6-28-2010

Theoretical and experimental studies of optically pumped molecular gas lasers

Ratanavis Amarin

Recommended Citation

Amarin, Ratanavis. "Theoretical and experimental studies of optically pumped molecular gas lasers." (2010). https://digitalrepository.unm.edu/ose_etds/2

Amarin Ratanavis

Candidate

Physics and Astronomy

Department

This dissertation is approved, and it is acceptable in quality and form for publication:

Approved by the Dissertation Committee:

, Chairperson

Paul R Schwoebel

THEORETICAL AND EXPERIMENTAL STUDIES OF OPTICALLY PUMPED MOLECULAR GAS LASERS

BY

AMARIN RATANAVIS

B.S.(hons.), Industrial Physics, King Mongkut's Institute of North Bangkok, 1999
M.S., Physics, King Mongkut's University of Thonburi, 2002
M.S., Physics, New Mexico State University, 2003
M.S., Optical Science and Engineering, University of New Mexico, 2007

DISSERTATION

Submitted in Partial Fulfillment of the
Requirements for the Degree of

Doctor of Philosophy
Optical Science and Engineering

The University of New Mexico
Albuquerque, New Mexico

May, 2010

Dedication

To my family

Acknowledgments

First and foremost I would like to thank my advisor Dr. Wolfgang Rudolph who enthusiastically taught and guided me for all these years. His incredible scientific view has always been inspired me. His advices were invaluable. I would like to thank Dr. Neil Campbell who guided me on many aspects of molecular gas lasers. I truly appreciate his guidance, discussions and supports. I had a great fortune to work with Dr. Vasudevan Nampoothiri who has exceptional experimental skills. I would like to thank him for his hard works helping me on experiments. I had the opportunity to have taken courses taught by great scientists during my graduate years- Dr. Mansoor Sheik-Bahae, Dr. Sanjay Krishna, Dr. Sudhakar Prasad and Dr. Wolfgang Rudolph. My sincere thank to all those great professors. I would like to thank Dr. Paul Schwoebel for the lessons on vacuum fitting that I have learnt which have helped me in setting up my experiments. I also would like to thank my colleagues and other research staff in our group who constantly supported and encouraged me- Dr. Luke Emmert, Dr. Mark Mero, Dr. Xuejun Liu, Duy Nguyen, Jim (Zhianling) Sun, Cristina Rodriguez, Reed Weber and Nathan Zameroski.

Last but not least I would like to thank the Royal Thai Government Scholarship for giving me the opportunity to earn this degree.

THEORETICAL AND EXPERIMENTAL STUDIES OF OPTICALLY PUMPED MOLECULAR GAS LASERS

BY

AMARIN RATANAVIS

ABSTRACT OF DISSERTATION

Submitted in Partial Fulfillment of the
Requirements for the Degree of

Doctor of Philosophy

Optical Science and Engineering

The University of New Mexico
Albuquerque, New Mexico

Theoretical and experimental studies of optically pumped molecular gas lasers

by

Amarin Ratanavis

B.S.(hons.), Industrial Physics, King Mongkut's Institute of North Bangkok,1999

M.S., Physics, King Mongkut's University of Thonburi, 2002

M.S., Physics, New Mexico State University, 2003

M.S., Optical Science and Engineering, University of New Mexico, 2007

Ph.D., Optical Science and Engineering, University of New Mexico, 2010

Abstract

Optically pumped molecular gas lasers based on vibrational-rotational transitions in the infrared spectral region were studied experimentally and theoretically. A model was developed to predict the performance of such lasers and explore their potentials for energy and power scaling. This rate equation model was applied to explore the performance of a second-overtone (pulsed) and a first-overtone (CW) pumped HBr laser. Experimental improvements concerning temperature spectral tuning and frequency stabilization of a Nd:YAG laser that pumped HBr were accomplished. Lasing at 4 microns was demonstrated from such a system. We identified acetylene and hydrogen cyanide as potential laser gases that can be pumped with lasers emitting in the attractive telecommunication C band region at about 1.5 microns. Estimations and fluorescence measurements suggest the possibility of lasing in the 3 micron region. Lasing was demonstrated for the first time with a 5 ns pump pulse from an optical parametric oscillator using traditional cavities. The first gas filled hollow fiber laser based on population inversion was demonstrated with C_2H_2 and emission in the 3 micron region was observed. An analytical model indicates the possibility of CW lasing with small Stokes shift in both C_2H_2 and HCN.

Contents

List of Figures

List of Tables

Chapter 1

Introduction

1.1 Background and Thesis Goals

Since the demonstration of the first laser in 1960 [1], lasers have become indispensable tools in areas ranging from fundamental research to industrial applications to medicine. Possible laser media comprise all states of matter - gases, liquids, solid materials and plasmas. Laser emissions were observed from the X-ray to the micrometer wave region [2]. The application determines the choice of laser and each type of laser has specific advantages and disadvantages. Semiconductor lasers exhibit very high efficiencies (up to 70%), are user-friendly but it is difficult to achieve average powers exceeding several kW. Solid-state (mostly active ions in a host material) lasers (SSLs) can produce larger output powers and pulse energies, however at reduced wall-plug efficiency. The reason is that unlike semiconductor lasers that can be pumped directly by electrical currents, SSLs are typically pumped optically and thus require one more (lossy) step of energy conversion.

Soon after the invention of the laser (solid-state, Ruby laser) the first gas laser was built (HeNe laser [3]). The most widely used pumping schema of gas lasers is an electrical discharge. Electron-atom, electron-molecule, or ion-atom collisions excite the active gas medium (example CO_2), or a gas particle which then transfers energy to the lasing gas (example HeNe). Continuous wave (CW) output powers of 150 kW have been achieved with CO_2 lasers. Unlike solid state materials a gas medium can be replenished relatively easily should it be necessary, which mitigates "damage" problems and heat dissipation. Wall-plug efficiencies of 10% have been reported for CO_2 lasers, which emit in the infrared spectral region ($\sim 10\,\mu$m). While this efficiency is relatively high, gas lasers that emit in the visible spectral region typically have efficiencies that are far less. Nevertheless, Ar-ion lasers (0.1% efficiency, typically P $\sim$ 10 W) and He-Ne lasers (0.1% efficiency, typically P $\sim$ 5 mW) were among the most widely used lasers until recently, when compact, more efficient solid-state and diode lasers started to replace them.

Optically pumped gas lasers (OPML) have been around for over 40 years. Compared to other types of lasers, gas lasers have a number of advantages. For example, gases have very high resistance to optical damage. Gases can be cooled by convection. Due to their broad spectra coverage from the ultra violet (UV) to the millimeter-wave region, gas lasers can be useful for specific wavelengths that are unavailable from other types of lasers [4]. The major drawback of OPML is the difficulty to find a suitable gas medium which can be pumped with available laser sources. In addition the line width of a molecular gas is on the order of hundreds of MHz; thus, a narrow band pump source is necessary to efficiently deposit the pump energy into the gas.

About ten years ago a renewed interest in optically pumped gas lasers emerged. The idea was to combine features of solid-state laser technology (high efficiency, compact design) with the advantages of gas media (heat dissipation, resistance to optical damage). In addition, gas media could allow access to wavelength regions, in particular in the near and mid infrared spectral (NIR and MIR) region, where the atmosphere is highly transmissive and where presently solid-state lasers are not available. These hybrid laser systems became possible when high-power lasers based on solid materials could be made narrow-band to pump the narrow absorption transitions of gases efficiently. Possible pump sources were solid-state, semiconductor and fiber lasers. Typically, these optically pumped gas lasers (OPGLs) if based on molecules (OPMLs) have large Stokes shifts. A by-product of these laser systems is a substantially improved output beam profile that is very forgiving of the pump beam profile.

Another area of intensive research is the coherent combination of the laser output of many individual fiber and or diode lasers. While the CW power of each individual source is limited by fundamental material (damage) parameters, the coherent superposition of many sources would allow output powers that are orders of magnitude higher. Despite various successes [5], the principal problems remain: the individual emitters to be combined have to be able to maintain a certain degree of coherence with respect to each other. This is difficult to achieve if high power must be maintained at the same time [5]. Suitably chosen gases where the laser wavelength is close to the pump wavelength (small Stokes shift) seem to offer the possibility to act as coherent beam combiners. While emitting within a spectrally narrow range depending on the gas medium, the individual pump sources do not have to maintain coherence. The laser action itself will combine the mutually incoherent sources into one coherent output beam with also dramatically improved spatial characteristics.

A crucial aspect of the hybrid laser is the combination of a viable pump source and gas. This is not trivial since gaseous media and available attractive (efficient, widely available) pump sources are limited. While in principle nonlinear optical devices such as optical parametric oscillators and amplifiers, can provide tunable pump radiation to match the absorption lines of gases, most such systems will only be of academic interest. Today a viable concept must allow the potential use of a SSL, semiconductor of fiber laser pump so that after demonstration of the proof of principle, a pathway to power and energy scaling can be devised. Only then will it be possible to move those concepts out of research labs into the commercial sector. Therefore a considerable part of the ongoing research is focused on identifying possible gas and pump sources. At the same time the gas should be "user-friendly".

In 2003, Krupke and coworkers demonstrated the first optically pumped alkali atom laser[6]. The rubidium (Rb) laser is a three-level laser with a quantum efficiency of 98% and thus exhibits an extraordinarily small Stokes shift. The active medium is enclosed in a heat pipe and the temperature (393 K) controls the alkali vapor pressure. Meanwhile laser action has also been demonstrated in other alkali vapors, eg. Cs [7]. Efficiencies exceeding 63% have been observed in Cs lasers [7]. The output of two different diode laser sources was combined and a total laser output power of 17 W was achieved [8]. Despite these successes many issues remain. The lasers are pumped in the 800 nm region and the output is shifted by only a few nm to longer wavelengths. This output is not in the eye-safe spectral region, which is important for many practical applications. The heated cell is inconvenient and there are issues with contamination of the cell windows, limiting the time when the 17 W output was observed to a few hours [8]. These problems could be mitigated by (molecular) gases that do not require heated cells and that do not react with cell windows if one can find appropriate pump sources.

Derived from this state-of-the-art of optically pumped gas lasers the following goals were defined for the thesis.

1. In 2004, our group demonstrated an HBr laser pumped by a Nd:YAG laser [9]. This combination is very attractive because it uses a highly developed pump source (Nd:YAG laser), which is energy scalable. At the same time the laser output is in the 4 micron region where the atmospheric transmission is high. It was necessary to improve certain experimental features of this laser and to explore its operational limits. These experimental concept demonstrations

were to be combined with simulations. The goal of the simulations was to make predictions concerning the energy scalability, achievable efficiency, the potential of CW operation and frequency tuning of this laser system.

2. It is very attractive to pump gases directly by diode and or fiber lasers. It was necessary to identify gas media with resonances where those pump sources emit. Also, these pump sources ought to be readily available to avoid extensive pump source development. We identified as possible gas candidates hydrogen cyanide (HCN) and acetylene (C_2H_2). Both have absorption bands in the 1.5 micron region (telecommunication C band) where diode and fiber lasers as well as optical components are highly developed and cost efficient. Although theses gases have been studied extensively key molecular parameters that are necessary to assess the potential of lasing were not known. A combination of measurements and estimations were envisioned to extract the necessary information. Simulations and analytical laser models were to be applied to evaluate optimal laser and pump conditions for pulsed and CW operation.

3. Using these results prototype HCN and C_2H_2 lasers were to be developed and demonstrated experimentally. Suitable cavity configurations needed to be explored experimentally and with simulations.

4. Hollow glass fibers (for example photonic bandgap fibers [10]) opened up attractive possibilities for optically pumped gas lasers. These fibers can be filled with an active gas and excited optically to emit laser radiation. Long interaction lengths of a spatially confined pump and the gain media can be realized. While these gas filled fibers have been used for nonlinear optical frequency conversion, lasing based on population inversion remained an open problem. The results for HCN and C_2H_2 were to be evaluated with respect to demonstrating the first hollow-fiber filled gas laser and, if possible, a proto-type hollow-fiber gas laser was to be demonstrated.

1.2 Outline of the Thesis

Chapter 2 summarizes molecular physics as it pertains to optically pumped lasers. Molecular energy levels are introduced and the selection rules that govern optically induced transitions between them are explained. The nature of vibration-rotation spectra in thermal equilibrium is discussed. The interactions of molecules with radiation and line broadening effects are described. Collision induced energy transfer processes are discussed.

Chapter 3 discusses the three molecular gas media that were of interest for this thesis in detail. We explain how molecular rate constants and parameters relevant for lasers were obtained. They are compiled and summarized in tables.

Chapter 4 presents a second overtone pumped HBr laser using a Nd:YAG pump laser operating at $1.34\,\mu$m. Improvements to the system concerning frequency shifting of the pump, line narrowing and stabilization of the Nd:YAG laser are described as well as the observed laser output.

Chapter 5 explores HCN and C_2H_2 as laser media. We first investigated fluorescence emission after excitation with a source emitting in the telecommunication C band. The results will be used to design a laser concept and demonstrate lasing with both gases.

Chapter 6 is devoted to the numerical modeling of OPMLs. The model was set up to serve generic OPGLs. As a case study, we applied it to describe and predict the performance of an optically pumped HBr laser. We study a second-overtone pumped pulsed and a first-overtone pumped CW laser. The model was also applied to predict certain aspects of the C_2H_2 and HCN laser.

In chapter 7 we analyze analytically the prospects of a CW laser with small Stokes shifts. This model requires certain simplifying assumptions. Their justification will be scrutinized with the numerical model.

In chapter 8 we will first apply a simple laser model using the laser parameters derived from previous chapters to assess the potential of a C_2H_2 filled hollow fiber laser. We will then report on the first gas-filled hollow laser based on population inversion.

Chapter 9 presents a summary of the thesis and a brief outlook of future work.

Chapter 2

Molecular physics

The knowledge of molecular physics is crucial for the understanding of OPMLs. In this chapter, a brief review of molecular physics related to OPMLs is presented. The scope of the discussion is limited to mid infrared (IR) OPMLs. The aim of this chapter is to develop an intuitive understanding of the molecular physics of mid IR OPMLs that will be important for later chapters of the dissertation. We will start with a description of molecular energy levels in section 2.1. The properties of the energy levels are what set molecules apart from other laser media such as solid state lasers. Light induced transitions are governed by selection rules, which will be discussed in section 2.2. Section 2.3 introduces the Boltzmann distribution which controls occupation numbers of energy levels at thermal equilibrium. This distribution is also responsible for the typical shapes of vibration-rotation spectra. In section 2.4, the molecular transition line widths are described. Section 2.5 discusses collision induced energy transfer between active molecules (self collisions) or through interactions (collisions) with atomic or molecular buffer gases. Such interactions can lead to molecular transitions without the emission or absorption of radiation (radiation-less transitions).

2.1 Energy states of molecules

In general, the electronic system and the translational, rotational, and vibrational degrees of freedom of the molecule determine four sets of discrete energy levels [11]. For mid-IR OPMLs, where typically optical transitions correspond to energies less than 1 eV, we can neglect the electronic energy and assume that the electronic state does not change. To illustrate the remaining three degrees of freedom let us consider a diatomic molecule as an example, see Fig. 2.1.

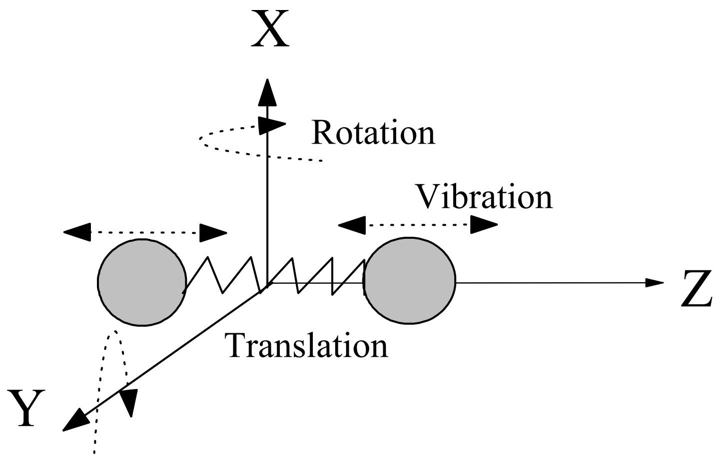

Figure 2.1: A diatomic molecule translates, rotates and vibrates simultaneously.

A molecule has a total of $3N$ degrees of freedom where N is the total number of atoms in the molecule, among them are three translational degrees of freedom [12]. Consequently a diatomic molecule has 6 degrees of freedom. From Fig. 2.1, it is obvious that such a molecule has two degrees of freedom of rotational motion and one degree of freedom of vibrational motion.

It should be mentioned that although the rotational and vibrational motions of molecules can be illustrated from the viewpoint of classical physics, they follow the rules of quantum mechanics [11]. The energy levels are quantized and therefore only certain rotational and vibrational energies are allowed.

2.1.1 Translational energy

The average translational kinetic energy of a single molecule corresponding to translation along each of the independent axes (x, y, and z) is equal to $\frac{1}{2}k_BT$, where k_B is the Boltzmann constant and T is the absolute temperature. Thus the total translational energy $E_{trans} = \frac{3}{2}k_BT$ [13]. From the total translational energy, the average speed of the molecule can be calculated [13]

$$v_{rms} = \sqrt{\frac{2E_{trans}}{m}} = \sqrt{\frac{3k_BT}{m}} = \sqrt{\frac{3RT}{M_m}} \ , \tag{2.1}$$

where m is the mass of a molecule, M_m is molar mass of molecules (kg/mol) and R is the universal gas constant(J/K/mol). The molar mass is related to the mass of the molecule by $M_m = N_Am$ where N_A is the Avogadro constant, and the universal gas constant $R = N_Ak_B$.

However the speed of molecule is generally referred to the mean speed which can be derived from the Maxwell-Boltzman distribution. The mean speed is given by [13],

$$\overline{v} = \sqrt{\frac{8k_BT}{\pi m}} = 0.92\ v_{rms} \ . \tag{2.2}$$

The average displacement path of a molecule between collisions is called mean free path. As shown in Fig. 2.2, if gas molecules A have diameter D_A and gas molecules B have diameter D_B, then the effective cross-section for collision can be given by [14],

$$\sigma_{AB} = \pi\left(\frac{D_A + D_B}{2}\right)^2 = \pi\frac{D_{AB}^2}{4} \ . \tag{2.3}$$

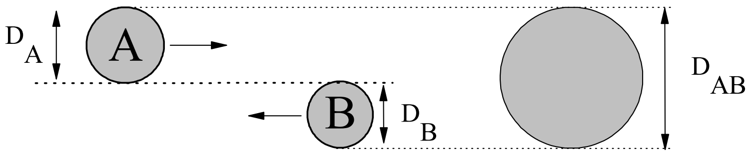

Figure 2.2: The collision between gas A molecule and gas B molecule.

In general, the collision rate per unit volume between molecules is given by [14]

$$Z_{AB} = \sqrt{2}\ \sigma_{AB} N_A N_B \overline{v}_{AB}\ , \tag{2.4}$$

where N_A and N_B are the number density of gas molecules A and B respectively. The mean speed of molecule A and B ($\overline{v}_{AB}$) is,

$$\overline{v}_{AB} = \sqrt{\frac{4k_BT}{\pi m_{AB}}}\ , \tag{2.5}$$

where m_{AB} is the reduced mass [14],

$$m_{AB} = \frac{m_A m_B}{m_A + m_B}\ , \tag{2.6}$$

where m_A and m_B are the mass of gas A and B respectively. The collision rate of gas molecule A is then $Z_{AA} + Z_{AB}$. Therefore the collision rate per one gas molecule A is written by,

$$z_A = \frac{Z_{AA}}{N_A} + \frac{Z_{AB}}{N_A}\ . \tag{2.7}$$

There the mean free path of gas A in the mixture of gases A and B can be obtained by the mean speed of gas A divided by z_A. The mean free path is then,

$$l_f = \frac{1}{\sqrt{2}N_A\sigma_A + \sqrt{2}N_B\sigma_{AB}\sqrt{\frac{m_A+m_B}{2m_B}}}\ , \tag{2.8}$$

For the self collision ($N_A = N_B$, $m_A = m_B$ and $N_A + N_B = N_t$), the expression reduces to [13]

$$l_f = \frac{1}{\sqrt{2} N_t \sigma_A} \ . \tag{2.9}$$

From the mean speed of gas A and its mean free path, the mean time between collision of gas A can be obtained [13]

$$\tau = \frac{l_f}{\bar{v}_A} \ . \tag{2.10}$$

2.1.2 Rotational energy

It is convenient to represent molecular rotation as a superposition of rotations about three orthogonal axes. A molecule rotates about its center of mass with the moments of inertia I_j defined as [15]

$$I_j = \sum_i m_i r_i^2 \ . \tag{2.11}$$

Here m_i is the mass of the atom i and r_i is the orthogonal distance from the atom to the axis of rotation The rotational axis corresponding to the largest moment of inertia is defined as c-axis and its moment of inertia is labeled I_c. The axis that has the smallest moment of inertia is perpendicular to the c-axis: this axis is called a-axis and its moment of inertia is defined as I_a. The third axis, perpendicular to both the c and a axis is labeled as b-axis and its moment of inertia is defined as I_b [15].

Depending on the relationships between the three different moments of inertia, five molecular rotational symmetries can be distinguished. They are spherical top, prolate top, oblate top, asymmetrical top and linear molecules as shown in Fig. 2.3 [16]. For the spherical top, all of the three moments of inertia are equal, i.e,

$I_a = I_b = I_c$. Examples of such molecules are CF_4 and SF_6. For the prolate top, the moments of inertia are such that $I_a < I_b = I_c$; CH_3Cl is an example molecule. A molecule that has the moments of inertia, $I_a = I_b < I_c$ is classified as oblate top; an example is benzene. Molecules for which none of the moments of inertia are equal are called asymmetrical top. H_2O is an example. Linear molecules like for example HF, HCN, CO, and CO_2 are characterized by $I_a = 0, I_b = I_c$. The molecules of interest in this thesis are of the latter type and we will restrict our discussion to them.

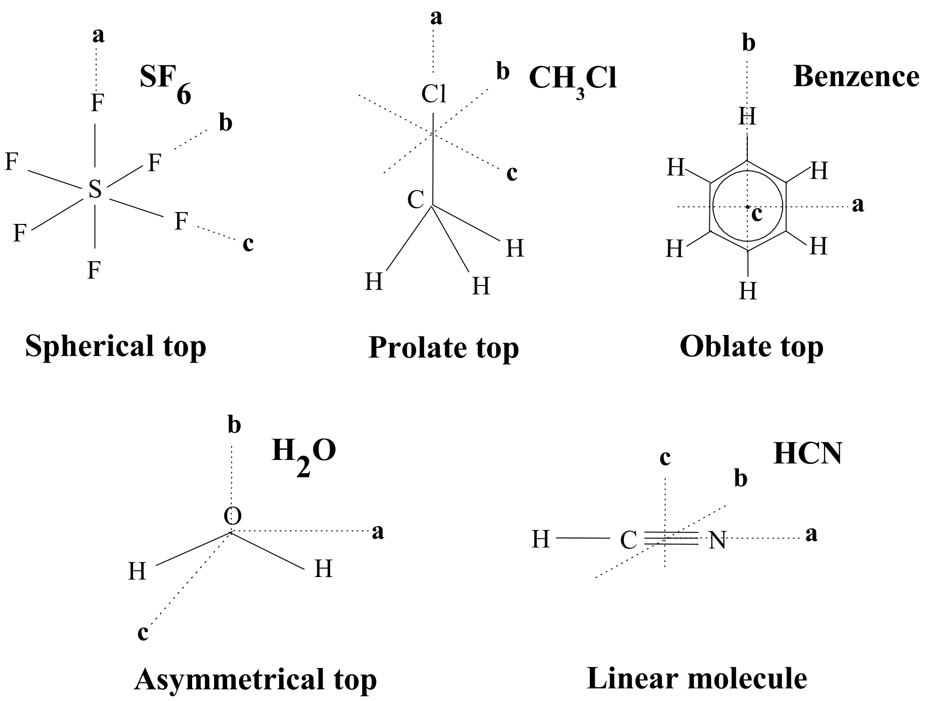

Figure 2.3: Examples of the molecular rotational symmetries.

The rotational energy of a linear rigid rotor is given by [15],

$$E(J) = BJ(J+1) \ , \tag{2.12}$$

where J is the rotational quantum number and B is the rotational constant. For linear molecules $B = \hbar^2/2I_b$ (joules) [16] with $I_b = I_c$. However, by the nature of molecules, they are not rigid bodies. As they rotate, they experience the centrifugal force in balance with a restoring force. This leads to higher order correction terms in the rotational energy [16],

$$E(J) = BJ(J+1) - D\left[J(J+1)\right]^2 \ , \tag{2.13}$$

where D is the centrifugal distortion constant.

The rotational constant (B) and the centrifugal distortion constant (D) are weakly dependent on the vibrational state:

$$E_V(J) = B_V J(J+1) - D_V\left[J(J+1)\right]^2 \ , \tag{2.14}$$

where

$$B_V = \frac{\hbar^2}{2I_V} \ , \tag{2.15}$$

where I_V is the moment of inertia for a molecule in a particular vibrational state, V is the vibrational quantum number and D_V is the centrifugal distortion constant.

In usual spectroscopic notation, the energy and the rotational constants are given in cm^{-1}. In this thesis, the energy and rotational constants that are presented in the units of cm^{-1} will be denoted as "$\tilde{}$" eg., $\tilde{B}_V$ and $\tilde{E}_V$. These quantities can be converted to corresponding SI units (joules) by multiplying with $100hc$. For eg.,

$$B_V = 100\,hc\,\tilde{B}_V \ . \tag{2.16}$$

2.1.3 Vibrational energy

As shown in Fig 2.1, the vibration of a diatomic molecule is fairly simple since it has only one type of the vibration. However for a polyatomic molecule, the situation is more complex. The concept of vibrational normal mode is used to identify the types of the vibrational motion. A normal mode is a summation of the molecular motions in which the center of the molecular mass remains fixed, all atoms in the molecule move along with the same phase and the vibration is harmonic [15]. There are $3N-6$ and $3N-5$ normal modes of vibration for a nonlinear and linear molecule, respectively, where N (as defined in section 2.1) is number of atoms in the molecule.

A diatomic molecule has 2 atoms and subsequently only one vibrational normal mode is expected. With anharmonicity, the vibrational energy of a diatomic molecule can be written as [16]

$$E(V) = h\nu_e\left(V+\frac{1}{2}\right) - h\nu_e\chi_e\left(V+\frac{1}{2}\right)^2 , \tag{2.17}$$

where ν_e is the vibrational frequency, χ_e is the dimensionless anharmonicity constant and V is vibrational quantum number.

Polyatomic molecules have several vibrational normal modes. For example, triatomic molecules as shown in Fig 2.4 have 3 atoms and 4 vibrational normal modes. However their bending modes assigned as V_2 have the same vibrational frequency [12]. In this situation, the bending modes are called doubly degenerate. In general to describe the vibrational state of a linear polyatomic molecule with vibrational normal modes (M), we can use a set of vibrational quantum numbers $(V_1, V_2, \ldots, V_M)$.

The vibrational energy of such a polyatomic molecule is then [16]

$$E(V_1, V_2, \ldots, V_M) = h\nu_1\left(V_1+\frac{1}{2}\right) + h\nu_2\left(V_2+\frac{1}{2}\right) + \ldots + h\nu_M\left(V_M+\frac{1}{2}\right) , \tag{2.18}$$

where ν_M is the vibrational frequency of normal mode M, V_M is its vibrational quantum number.

For triatomic molecules having degenerate vibrational normal modes such as the

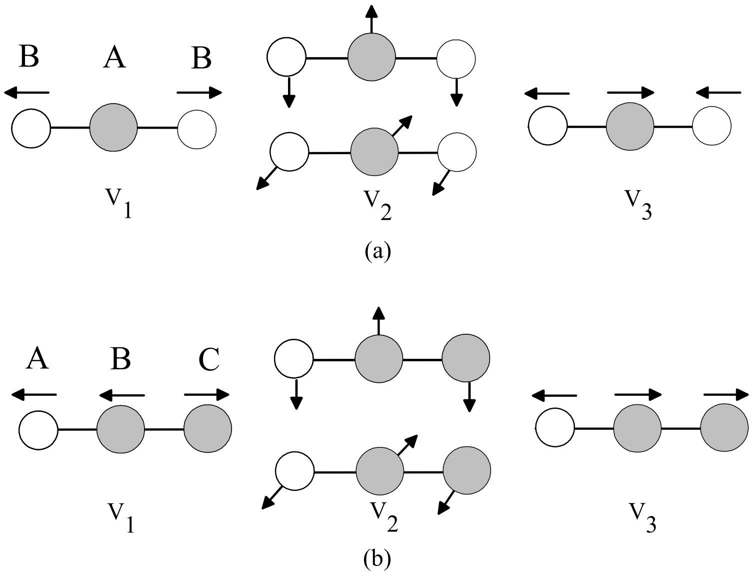

Figure 2.4: Examples of the vibration normal mode of linear triatomic molecules (a) AB_2 (b)ABC.

molecules in Fig 2.4, the vibrational energy is,

$$E(V_1, V_2, V_3) = h\nu_1 \left(V_1 + \frac{1}{2} \right) + h\nu_2 \left(V_2 + \frac{d_V}{2} \right) + h\nu_3 \left(V_3 + \frac{1}{2} \right) \ , \tag{2.19}$$

where d_V is the degree of degeneracy (in this case of the triatomic molecules, $d_V = 2$).

A molecule vibrates and rotates at the same time. From the Born-Oppenheimer approximation it follows that typical rotational energies are much smaller than vibrational energies. The vibrational-rotational energy of a molecule is simply the sum of the two energies [15],

$$E(V, J) = E(V) + E_V(J) \ . \tag{2.20}$$

Using Eqs. (2.14), (2.17) the vibrational-rotational energy is given by

$$E(V,J) = h\nu_e \left(V + \frac{1}{2}\right) + B_V J\left(J+1\right) - D_V \left(J\left(J+1\right)\right)^2 \ , \tag{2.21}$$

for a diatomic molecule. Using Eqs.(2.14) and (2.18)

$$\begin{aligned} E(V_1, V_2, \ldots, V_M, J) \ &= \ h\nu_1 \left(V_1 + \frac{1}{2}\right) + h\nu_2 \left(V_2 + \frac{d_V}{2}\right) + \ldots + h\nu_M \left(V_M + \frac{1}{2}\right) \\ &\quad + B_V J\left(J+1\right) - D_V \left(J\left(J+1\right)\right)^2 \ . \end{aligned} \tag{2.22}$$

for a polyatomic molecule where we assumed that normal mode 2 is doubly degenerate.

2.2 Selection rules

For gases to be used in (mid) IR OPMLs, we only need to consider translational, rotational and vibrational degrees of freedom. We assume that all transition occur within the electronic ground state. Energy transfer between these degrees of freedom is possible through molecular collisions. The three types of resonant interactions between radiation and matter important in OPMLs are stimulated absorption, stimulated emission and spontaneous emission. All these processes can produce population changes of molecular states.

Population inversion producing optical gain is required for laser action. Let us consider an upper laser level u and a lower laser level l. The small signal gain is given by

$$g = \sigma(\nu) \left(n_u - \frac{g_u}{g_l} n_l\right) = -\alpha \ , \tag{2.23}$$

where n_u and n_l are the number densities of molecules in the upper and lower laser state, respectively. g_u and g_l are degeneracy factors,

$$g_{u(l)} = 2J_{u(l)} + 1 \ , \tag{2.24}$$

where $J_u(l)$ denotes the upper(lower) rotational state, and

$$\sigma(\nu) = \frac{A_E \, \lambda^2 \, S(\nu)}{8\pi} \ , \tag{2.25}$$

is the stimulated emission cross section where λ is the photon wavelength, $S(\nu)$ is line shape profile[1] of a transition and A_E is the Einstein coefficient for spontaneous emission given by [15]

$$A_E = \frac{64\pi^4\nu^3}{12\pi\epsilon_o hc^3}|R_{o\to f}|^2 \ . \tag{2.26}$$

Here ν is the photon frequency, ϵ_o is the permittivity of free space and $R_{o\to f}$ is the transition moment.

In order to have laser gain $g > 0$, and the population in the upper state must be larger than the population in the lower state. In the opposite case, $g < 0$, radiation is absorbed. Transitions can only occur if the transition moment $R_{o\to f}$ is non-zero. Selection rules exist that predict allowed transitions for which the transition moment is nonzero.

An optically excited transition between two energy levels separated by $\Delta E(V, J)$ can occur by absorbing or emitting a photon of energy $[h\nu = \Delta E(V, J)]$. While this is a necessary requirement it does not predict whether the transition is allowed.

Molecular transitions are classified as either IR active or Raman active. Since this dissertation deals with optical pumping and stimulated emission of radiation, the following discussion is restricted to IR active selection rules.

---

[1] The line shape profile will be discussed in section 2.4

Molecules vibrate and rotate simultaneously. Therefore a change of the vibrational state can be accompanied by a change in the rotational state leading to vibration-rotation spectra. Consequently the selection rules combine transition rules within vibrational and rotational states.

The vibrational selection rules are based on the harmonic oscillator approximation and state that (i) the change in vibrational quantum number must be such that $\Delta V = \pm 1$ and (ii) that the vibrational motion must change the dipole moment (oscillating dipole) [16]. In the latter case the molecule is said to be IR active. The vibrational selection rule is less strict, that is $\Delta V = \pm 1, \pm 2, ...$ is allowed, if anharmonicity is taken into account. The transition probabilities of these overtone transitions, however, become smaller with increasing $|\Delta V|$.

The rotational selection rule is related to the type of rotation. For diatomic molecules, the vibrational selection rule is $\Delta V = \pm 1$ and the rotational selection rule is $\Delta J = \pm 1$. Since a diatomic molecule has only one normal mode of vibration, it has to have a permanent dipole moment to be IR active. Thus the diatomic molecule must be heteronuclear.

Rotational transitions with $\Delta J = +1$ ($\Delta J = -1$) are referred to as R branch (P branch) transitions. R branch and the P branch transitions are usually labeled as $R(J)$ and $P(J)$ where J is the rotational quantum number of the lower state.

The vibrational selection rule $\Delta V = \pm 1$ and the possibility of higher overtone transitions are also valid for polyatomic molecules. Polyatomic molecules do not need to have a permanent dipole moment to be IR active. To verify that a transition of a polyatomic molecule is allowed, molecular group theory can conveniently be used. This approach, however, does not provide the strength of an allowed transition. To use molecular group theory the concept of molecular symmetries has to be described which is beyond the scope of this thesis- however there are sufficient literatures available on this topic for [16, 15]. However if the concerned vibrational transition is allowed, the rotational section rules of linear polyatomic molecules are the followings [15],

1. $\Delta J = \pm 1$, i.e., P and R branches for the vibrational transitions between ground state and the stretching vibrational normal mode(s) or between the stretching vibration normal modes.

2. $\Delta J = 0, \pm 1$, i.e., P, Q and R branches for vibrational transitions stated otherwise from the first rule.

Note that Q branch transition occurs when ($\Delta J = 0$).

2.3 Boltzmann's distribution

In the previous section we have seen that a potential vibrational-rotational transition can be predicted by the selection rules and group theory. After it has been concluded that a certain transition is allowed, the question about the transition strength arises. Let us discuss as an example molecular absorption lines. According to Eqs. (2.23), (2.25) and (2.26), we can assume that $R^2_{o \to f}$ is about the same independent of the actual rotational state involved. Obviously the absorption coefficient depends on the number density of molecules in the rotational state of the vibrational ground state.

In thermal equilibrium, the population of molecular energy levels can be described by a Boltzmann distribution [17],

$$n\left(V, J\right) = N_{\mathrm{tot}} \frac{\left(2J+1\right) e^{-E(V,J)/k_B T}}{\sum\limits_{V,J} \left(2J+1\right) e^{-E(V,J)/k_B T}} \ , \tag{2.27}$$

where N_{tot} is the total number density of molecules and $(2J + 1)$ is the degeneracy factor of a rotational state with quantum number J.

It is obvious that $k_B T$ controls the fraction of molecules occupying a particular rotational-vibrational state. Higher temperatures mean that the maximum population shifts to states with larger J. A larger rotational constant B_V narrows the $n(V)$ distribution and moves the maximum to states to smaller J values. This is exemplified in Fig. 2.5 for HBr and HCN. For one of the gases of interest, C_2H_2, the nuclear spin also affects the population in thermal equilibrium. The Boltzmann distribution of a nuclear spin molecule is given by [17],

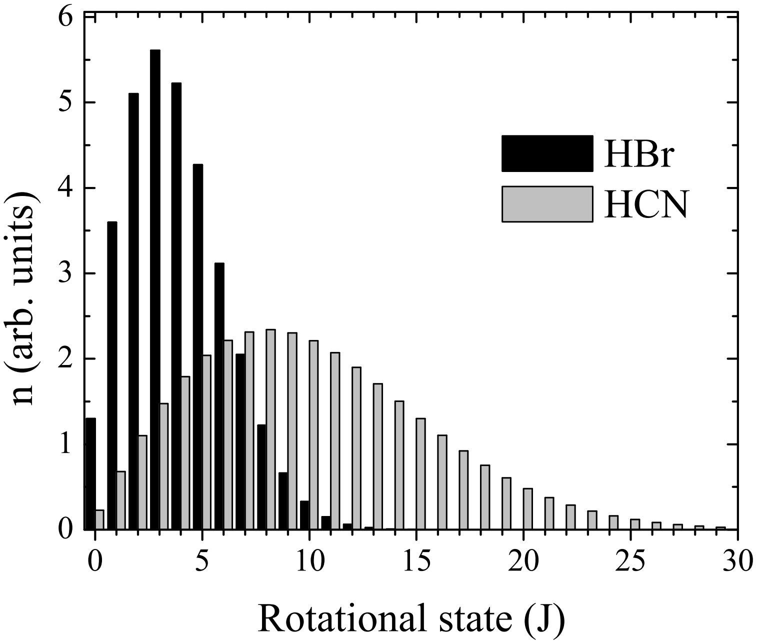

Figure 2.5: The rotational state occupation of HBr and HCN molecules in the vibrational ground state at room temperature.

$$n\left(V,J,K_i\right) \quad = \quad N_{\text{t}} \frac{\left(2K_i+1\right)\left(2J+1\right)e^{-E(V,J)/k_BT}}{\sum\limits_{V,J}\left(2K_i+1\right)\left(2J+1\right)e^{-E(V,J)/k_BT}}\ , \tag{2.28}$$

where $2K_i + 1$ is the nuclear spin degeneracy factor and K_i is the total nuclear spin quantum number. Here $K = 2I, 2I-1, \ldots, 0$ The nuclear spin (I) is half-integer for protons and integer for deuterium.

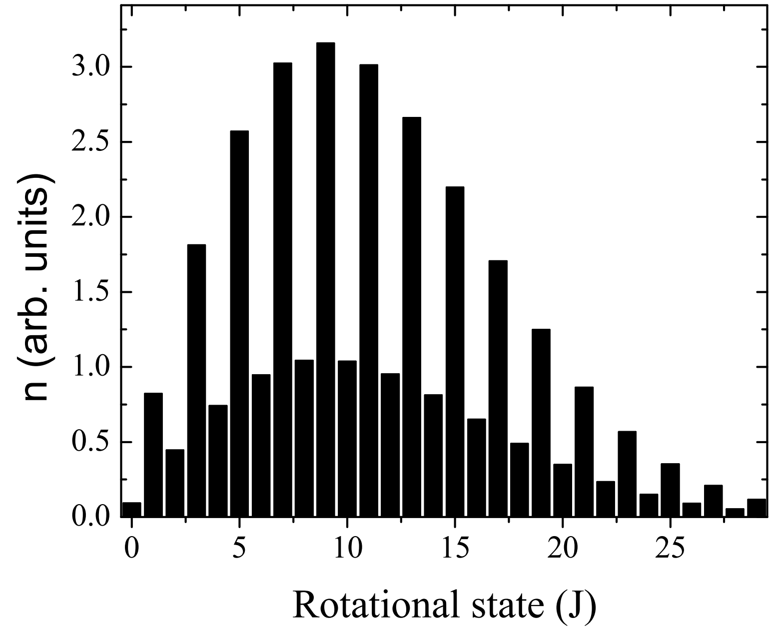

Figure 2.6: The rotational state occupation of C_2H_2 molecules in the vibrational ground state at room temperature.

For C_2H_2, each hydrogen atom has a nuclear spin (I) of 1/2, therefore, the possible K values in Eq. 2.28 are 1 and 0. Thus the nuclear spin degeneracy factor of C_2H_2 is 1 and 3. The assignment of the nuclear spin degeneracy factors is 1 for even J and 3 for odd J for C_2H_2.

$$\begin{aligned} n\left(V, J_{\mathrm{even}}, K=0\right) &= N_{\mathrm{t}} \frac{(2J+1)\, e^{-E(V,J)/k_B T}}{\sum\limits_{V,J_{\mathrm{even}}} (2J+1)\, e^{-E(V,J)/k_B T} + \sum\limits_{V,J_{\mathrm{odd}}} 3\,(2J+1)\, e^{-E(V,J)/k_B T}} \\ n\left(V, J_{\mathrm{odd}}, K=1\right) &= N_{\mathrm{t}} \frac{3\,(2J+1)\, e^{-E(V,J)/k_B T}}{\sum\limits_{V,J_{\mathrm{even}}} (2J+1)\, e^{-E(V,J)/k_B T} + \sum\limits_{V,J_{\mathrm{odd}}} 3\,(2J+1)\, e^{-E(V,J)/k_B T}} \,. \end{aligned} \tag{2.29}$$

This assignment can be explained by the Pauli principle. According to the Pauli principle, the symmetry of the total wave function of molecules with equivalent nuclei must be in agreement with symmetry requirements dictated by the interchange of nuclei [18]. The interchange of nuclei of half-integer spin must result in an antisymmetric wavefunction while for nuclei of integer spin the result is the opposite [18]. The total wave function can be written as,

$$\psi_t = \psi_{el}\psi_{vib}\psi_{rot}\psi_{nuc} \; . \tag{2.30}$$

For the ground state of C_2H_2, the product of $\psi_{el}\psi_{vib}$ is symmetric with respect to nuclear interchange [18]. Therefore the product of ψ_{rot} and ψ_{nuc} must be antisymmetric. However, ψ_{rot} is symmetric for even J and antisymmetric for odd J [18]. Furthermore the product of ψ_{nuc} spin functions for two protons of the hydrogen atoms in C_2H_2 results in three symmetric spin functions and one antisymmetric spin function [16]. Therefore the nuclear spin degeneracy factor is one for even J and three for odd J.

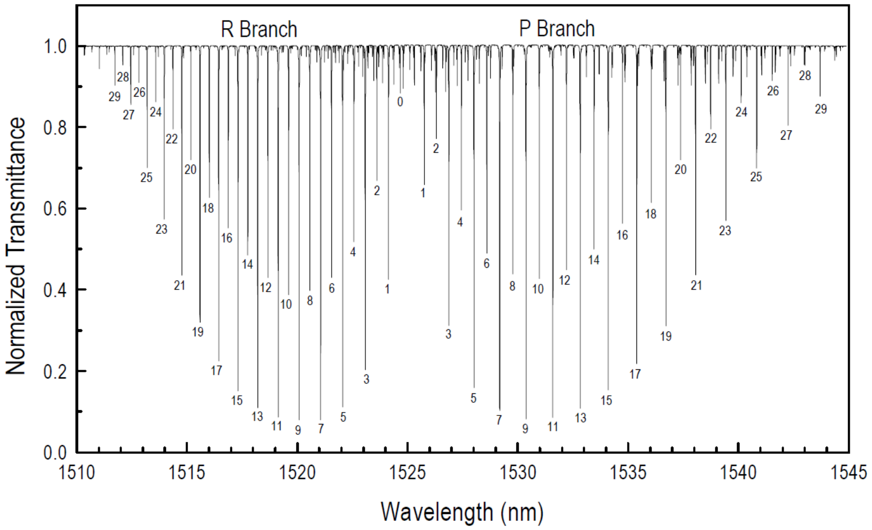

Figure 2.7: The absorption spectrum of C_2H_2 molecules in the 1.5 μm region at room temperature. Modified from [19].

The distribution of the population in rotational states for even J and odd J is shown in Fig 2.6. These population distributions result in the absorption spectrum of C_2H_2 as shown in Fig. 2.7

2.4 Line widths

The spectrum of a molecule as seen for C_2H_2 in Fig. 2.7 contains many absorption lines. Each line has a finite width and characteristic shape defined by the line shape function $S(\nu)$ in Eq. 2.25. The integral of the line shape function is normalized to unity,

$$\int_0^\infty S(\nu)d\nu = 1 \ . \tag{2.31}$$

The line width of the molecular transition is determined by three line broadening processes - natural line broadening, collisional broadening and Doppler broadening. While the first two mechanisms give rise to homogeneous broadening, the Doppler effect gives rise to inhomogeneous line broadening.

First, let us discuss the three broadening mechanisms separately. The lifetime of a molecular state is finite even for an isolated single molecule. In the absence of energy transfer between normal modes, this natural lifetime is determined by spontaneous emission. The natural lifetime is given by [16],

$$\tau_e = \frac{1}{A_E} \ . \tag{2.32}$$

According to the Heisenberg uncertainty principle, the lifetime of the state (τ_e) and the uncertainty of its energy (ΔE) are related [16],

$$\tau_e \Delta E \geq \hbar \ . \tag{2.33}$$

The uncertainty of the energy results in the natural linewidth (Full width at Half Maximum, FWHM,) of the line shape function which can be expressed as [16], (the natural line shape function is Lorentzian [20])

$$\Delta\nu_e = \frac{1}{2\pi\tau_e} \ . \tag{2.34}$$

In most practical situations the line broadening of a molecule in a gas is dominated by the other two broadening mechanisms.

Pressure broadening is described by a Lorenztian (line-shape) function [20]

$$S_c(\nu) = \frac{\Delta\nu_c/\pi}{(\nu_o - \nu)^2 + \Delta\nu_c^2} \ , \tag{2.35}$$

where ν_0 is the resonance frequency and $\Delta\nu_c$ is the line width (Half Width at Half Maximum, HWHM),

$$\Delta\nu_c = \frac{1}{2\pi\tau} \ , \tag{2.36}$$

where τ is the collision time of a molecule as defined in Eq. (2.10). The pressure broadening coefficients are specific for the resonant molecule and the collision partner as derived in section 2.1.1. At resonance $\nu = \nu_o$ the line shape factor is,

$$S_c(\nu_o) = \frac{1}{\pi\Delta\nu_c} \ . \tag{2.37}$$

Doppler broadening arises from the translational motion of molecules. Consider for example a molecule having a resonance frequency ν_o and moving in z direction with velocity ($v_z \ll c$) away from a light source of frequency ν. To the molecule the light frequency appears to be shifted

$$\nu' = \nu\left(1 - \frac{v_z}{c}\right) \ . \tag{2.38}$$

The molecule can absorb the Doppler shifted radiation if $\nu' = \nu_o$. This means that

$$\nu = \frac{\nu_o}{1 - \frac{v_z}{c}} \ , \tag{2.39}$$

becomes the frequency of the light source that can be absorbed by moving molecules ($\nu = \nu_o'$). Since ($v_z \ll c$), the equation above can be approximated by,

$$\nu_o' = \nu_o \left(1 + \frac{v_z}{c}\right) \ . \tag{2.40}$$

For gases in thermal equilibrium, the fraction of molecules moving along the z axis with velocity between v_z and $v_z + dv_z$ is given by the Maxwell-Boltzmann distribution [20],

$$p(v_z)dv_z = \left(\frac{m}{2\pi k_B T}\right)^{1/2} e^{-mv_z^2/2k_BT} dv_z \ . \tag{2.41}$$

From Eq. (2.39) it follows that

$$v_z = \frac{c}{\nu_o}\left(\nu - \nu_o\right) \ . \tag{2.42}$$

Using Eq.(2.29) with Eq.(2.30) and $dv_z = (c/\nu_o)d\nu$, the Doppler line shape function becomes [20],

$$S_d(\nu) = \frac{1}{\Delta\nu_d}\left(\frac{4ln2}{\pi}\right)^{1/2} e^{-4(\nu-\nu_o)^2 \ln 2/\Delta\nu_d^2} \ , \tag{2.43}$$

where

$$\Delta\nu_d = \frac{2}{\lambda}\left(\frac{2k_BT}{m}\ln 2\right)^{1/2} \ , \tag{2.44}$$

is the Doppler line width (FWHM).

At resonance ($\nu = \nu_o$) the Doppler line shape factor

$$S_d(\nu_o) = \frac{1}{\Delta\nu_d}\left(\frac{4ln2}{\pi}\right)^{1/2} . \tag{2.45}$$

The total line shape function is a convolution of the these line shape functions introduced above. The result is a Voigt profile, which is the superposition of the Doppler line shape and the collision (Lorentzian) line shape.

The collision line shape function with the shifted frequency according to the Doppler effect can be written as [20]

$$S_c(\nu, v_z) = \frac{\Delta\nu_c/\pi}{(\nu_o + \nu_o v_z/c - \nu)^2 + \Delta\nu_c^2} . \tag{2.46}$$

The Voigt profile is then the integral of the product between $S_c(\nu, v_z)$ and the Maxwell-Boltzmann velocity distribution

$$\begin{aligned} S_v(\nu) &= \left(\frac{m}{2\pi k_B T}\right)^{1/2} \frac{\Delta v_c}{\pi} \int_{-\infty}^{\infty} \frac{dv_z e^{-mv_z^2/2k_BT}}{(\nu_o + \nu_o v_z/c - \nu)^2 + \Delta\nu_c^2} \\ &= \frac{1}{\pi^{3/2}} \frac{\xi^2}{\Delta\nu_o} \int_{-\infty}^{\infty} \frac{da\ e^{-a^2}}{(a+b)^2 + \xi^2} , \end{aligned} \tag{2.47}$$

where,

$$\begin{aligned} a &= \left(\frac{m}{2\pi k_B T}\right)^{1/2} v_z \\ b &= (4\ln 2)^{1/2}\ \frac{\nu_o - \nu}{\Delta v_d} \\ \xi &= (4\ln 2)^{1/2}\ \frac{\Delta v_c}{\Delta v_d} . \end{aligned} \tag{2.48}$$

At resonance ($\nu = \nu_o$) $b = 0$ and

$$S_v(\nu_o) = \frac{\xi^2}{\pi^{3/2}\Delta\nu_c} \int_{-\infty}^{\infty} \frac{da\ e^{-a^2}}{a^2 + \xi^2} , \tag{2.49}$$

and

$$\int_{-\infty}^{\infty} \frac{da\ e^{-a^2}}{a^2+\xi^2} = \frac{\pi}{\xi}\mathrm{erfcx}(\xi)\ . \tag{2.50}$$

Here erfcx(ξ) is the scaled complementary error function. With this notation the Voigt profile at resonance frequency takes on the form [20],

$$S_v(\nu_o) = \left(\frac{4ln2}{\pi}\right)^{1/2} \frac{1}{\Delta\nu_d}\mathrm{erfcx}(\xi)\ . \tag{2.51}$$

For high pressures, ($\xi \gg 1$) resulting in erfcx(ξ) $= \frac{1}{\sqrt{\pi}\xi}$, the Voigt profile approaches the collisional line broadening function and at resonance [20],

$$S_v(\nu_o) \approx S_c(\nu_o) = \frac{1}{\pi\Delta\nu_c}\ . \tag{2.52}$$

At low pressure ($\xi \ll 1$) leading to erfcx(ξ) $= 1$, the Doppler limit is represented [20],

$$S_v(\nu_o) \approx S_d(\nu_o) = \frac{1}{\Delta\nu_d}\left(\frac{4\ln 2}{\pi}\right)^{1/2}\ . \tag{2.53}$$

The width of the Voigt profile can be approximated by [21]

$$\Delta\nu_v \approx 1.0692\Delta\nu_c + \sqrt{(0.8664\Delta\nu_c^2) + \Delta\nu_d^2}\ . \tag{2.54}$$

With this approximation, the product of the Voigt profile (at resonance) and the width of the Voigt profile is,

$$S_v(\nu_o)\Delta\nu_v \approx 0.64\ , \tag{2.55}$$

for the collision limit where $\Delta\nu_v = 2\Delta\nu_c$ (FWHM), and

$$S_v(\nu_o)\Delta\nu_v \approx 0.94\ , \tag{2.56}$$

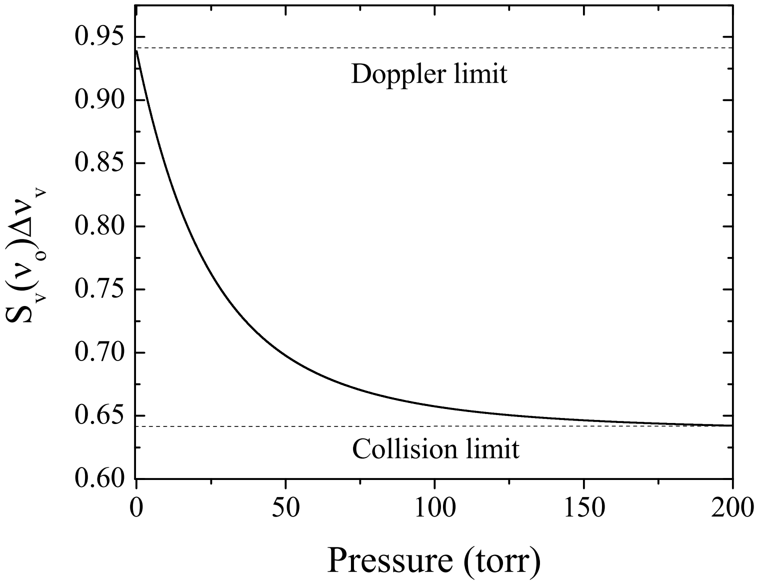

Figure 2.8: The product of $S_v(\nu_o) \times \Delta\nu_v$ as a function of pressure at room temperature for HBr gas. The second overtone transition at 1.34 μm was considered.

for the Doppler limit.

Figures 2.8 and 2.9 show line broadening parameters and the small signal absorption (see Eqs. 2.23 and 2.25) as a function of pressure. We considered second overtone transition at 1.34 μm of the HBr isotope 79 as an example.

At high pressures, the absorption coefficient is no longer increasing with pressure. In this limit of collisional broadening the absorption coefficient, cf. Eq. (2.23) with $n_l \gg n_u$ and from Eqs. (2.9), (2.10), (2.27), (2.25) and (2.52) becomes

$$\alpha = 1.42 \frac{g_u}{g_l} \frac{A_E \lambda^2}{8\pi\sigma_A} \sqrt{\frac{\pi m}{8 k_B T}} \frac{(2J+1)\, e^{-E(V,J)/k_B T}}{\sum\limits_{V,J} (2J+1)\, e^{-E(V,J)/k_B T}} \ , \tag{2.57}$$

and thus does not depend on pressure.

From the preceding discussion, to obtain the highest possible absorption, OPMLs should be operated at sufficiently high pressure. However at high pressures, collision

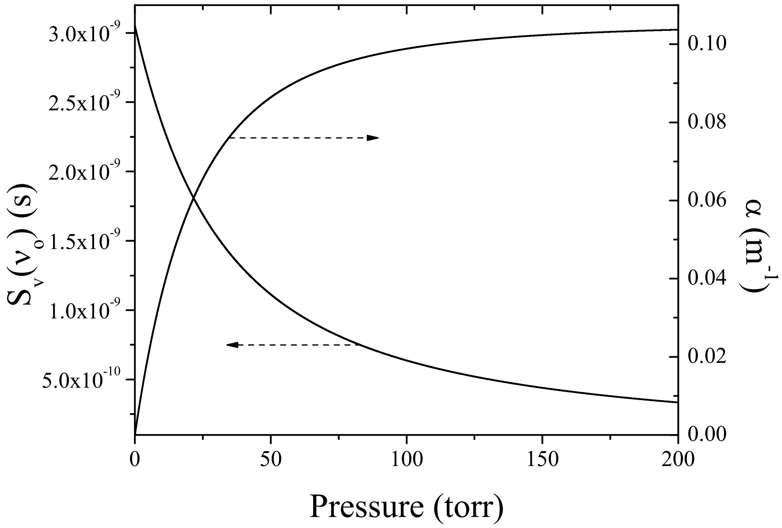

Figure 2.9: The Voigt profile at resonance $S_v(\nu_o)$ and the small-signal absorption coefficient(α) of the second overtone transition at 1.34 μm of HBr as the function of HBr pressure. The molecular parameter can be found in section 3.5.

induced energy transfer processes can lead to significant system losses and an overall optimization also including additional processes must be performed. In the next section we will discuss collision induced energy transfer.

2.5 Collision induced energy transfers

Collision induced transfer of energy can change the population numbers of molecular states. Such collisions are termed inelastic collisions as opposed to elastic collisions, which would only affect the line broadening. Inelastic collisions can provide a competing channel for depopulation of the upper pump level (population quenching) of a laser molecule (atom) and thus can directly affect the laser efficiency.

Let us consider an inelastic collision between two collision partners A and M

$$A_i + M_i \leftrightarrows A_f + M_f + \Delta E \ .$$

where the index i (f) stands for initial (final) state and

$$\Delta E = E_{A_f} + E_{M_f} - E_{A_i} - E_{M_i} \ , \tag{2.58}$$

is the energy defect. The forward rate k_f and the backward transfer rate k_r are related by

$$k_f = k_r \ e^{-\Delta E/k_B T} \ . \tag{2.59}$$

Due the anharmonic nature of the vibrational ladder of a molecule and the discreteness of the energy levels, there is typically a nonzero energy defect. This energy is absorbed or provided in most cases by the translational degrees of freedom.

The rotational inelastic collision process is often called rotational relaxation which describes the net population transfer in and out of the rotational state J within the same vibrational state V due to collisions. The rotational relaxation rate strongly depends on the change of the rotational quantum number ΔJ and the energy defect ΔE of the collisions. The rotational relaxation rate decreases as ΔJ and ΔE increase. This relationship can be described by the exponential energy gap law model (EG) [22],

$$k_{J\to J'} = a \ e^{-b\Delta E_{J\to J'}/k_B T} \ . \tag{2.60}$$

where J and J' are the initial rotational state and the final rotational state respectively. a and b are adjustable fitting parameters.

Another collision induced energy transfer is called vibrational relaxation. The vibrational relaxation is the process in which molecules exchange their vibrational energies by collisions. In general, the vibrational relaxation can be distinguished by the range of the energy defect If $\Delta E < k_B T$, the process called vibrational-vibrational (V-V) relaxation. However if the energy defect is much higher than $k_B T$, the process is called vibrational-translational relaxation (V-T). For collisions between polyatomic molecules, the vibrational energy exchange can occur between the same normal mode of vibration or between different normal modes of vibration.

For the collision between diatomic molecules, the energy defect usually determines how fast the relaxation process is and how efficiently energy is transferred. Consequently, the R-R process is the fastest followed by the V-V process and the V-T process. The order can be different for polyatomic molecules because vibrational energies of different normal modes can be very close.

Since diatomic molecules have only one normal mode of vibration, it is not difficult to predict relaxation pathways governed by V-V or V-T processes. In contrast, vibrational relaxation of polyatomic molecules is much more complicated. As a rule of thumb, those vibrational relaxation processes are favored for which the energy defect(Δ E) is small and for which the change of the vibrational quantum number (ΔV) is small [23].

2.6 Summary

For the gases to be used in mid-IR OPMLs, the translational, rotational and vibrational degrees of freedom are only need to be considered. The optical transitions occurs between vibrational-rotational states governed by selection rules. Boltzmann distribution controls the distribution of occupation numbers of energy levels at thermal equilibrium. The linewidth of molecular transition depends on various physical processes: natural line broadening, collisional broadening and Doppler broadening. Collision induced transfer of energy is a competing process for depopulation of the upper pump level of a molecule.

Chapter 3

HBr, HCN and C_2H_2 molecules

3.1 Introduction

HBr is an attractive OPML medium since its overtone transitions can be potentially pumped by well developed solid state lasers, for example Nd:YAG lasers, Tm:YAG lasers and Nd:glass lasers. Furthermore its emission lies in the 4 μm region which can be useful for applications such as remote sensing and imaging through the atmosphere. C_2H_2 and HCN are of interest for OPML systems because they can be pumped by readily available lasers emitting in the telecommunication C-band (~ 1.5 μm).

In this chapter we will discuss the molecular properties of the above three gases, in the context of relevance to OPML applications. Some of the data were extracted from literatures, some parameters were obtained from estimations and extrapolations. In addition to the above three gases, we will also provide spectroscopic data for HI as another potential OPML medium which can be pumped by C-band lasers that could be of importance for future studies.

3.2 HBr molecule

HBr naturally occurs in two isotopes ($H^{79}Br$ and $H^{81}Br$) with almost equal abundance [24]. HBr is a diatomic molecule and consequently has only one vibrational normal mode (see Fig. 3.1). A schematic diagram of the vibrational and rotational energy levels of HBr shown in Fig. 3.2. As discussed in section 2.2, the vibrational selection rule for a dipole allowed transition of a diatomic molecule is $\Delta V = \pm 1$. Therefore the lasing transitions shown in Fig. 3.2 are justified by the selection rules. However due to the anharmonicity of the vibrational levels of HBr higher overtone transitions of HBr are possible. The wavelength regions are 4 μm, 2 μm and 1.3 μm for fundamental transitions $V = 0 \rightarrow V = 1$, first overtone transitions $V = 0 \rightarrow V = 1$ and second overtone transition $V = 0 \rightarrow V = 2$ respectively. For experimental reasons[1], we consider a pump transition (from $V = 0$ ($J = 4$) to $V = 3$ ($J = 5$)) for second overtone pumping. In our simulations, we are also interested in the R(4) transition for first overtone pumping (from V=0 to V=2).

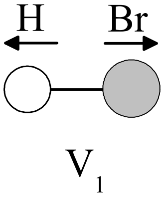

Figure 3.1: The vibrational normal mode of HBr.

The Einstein A coefficients for the pump transitions (A_{pump}) are $5\,s^{-1}$ for the fundamental, $0.1459\,s^{-1}$ for the first overtone transition [25] and $0.0083\,s^{-1}$ [24, 26] for the second overtone transition. The Einstein coefficients $A_{P,R}$ for the laser transitions are $5\,s^{-1}$ for R branches and $7\,s^{-1}$ for P branches of the fundamental (V to V-1) transitions [24, 26]. The pressure broadening coefficient of HBr is 4.7 MHz/torr

---

[1] this will be discussed in chapter 4

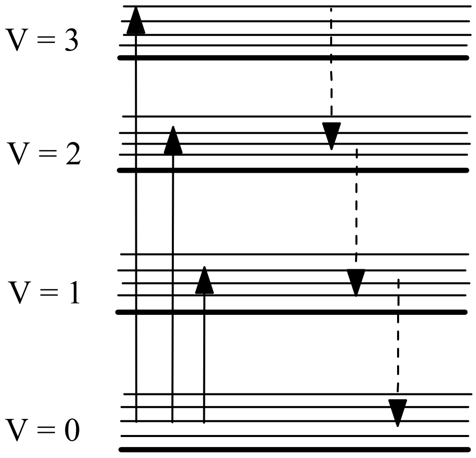

Figure 3.2: Energy level diagram of the HBr molecule. The solid arrows indicate the fundamental, first overtone and second overtone pump transtions. The dashed arrows stand for the multitude of possible R and P branch lasing transitions between adjacent vibrational states.

(HWHM) [27]. Table 3.1 exemplifies the cross section of HBr obtained from Eqs. (2.25) and (2.51) at room temperature and pressure of 20 torr.

Table 3.1: Transition wavelengths and cross sections for fundamental and overtone transitions of HBr at room temperature and a pressure of 20 torr.

Pump	wavelength(μm)	$\sigma(\nu_o)$m^2
fundamental	3.794	8.2×10^{-21}
first overtone	1.962	5.1×10^{-23}
second overtone	1.339	1.1×10^{-24}

Transition wavelengths of HBr shown in Table 3.1 can be calculated by using the spectroscopic constants in Table 3.2 and 3.3. The transition wavelengths (m) are calculated by,

$$\frac{1}{\lambda} = 100 \Big[\tilde{E}(V) - \tilde{E}(V') + \tilde{B}_V J(J+1) - \tilde{B}'_V J'(J'+1) \\ -\tilde{D}_V \left(J(J+1)\right)^2 + \tilde{D}'_V \left(J'(J'+1)\right)^2\Big] \tag{3.1}$$

Table 3.2: Spectroscopic constants of $H^{79}Br$ [28, 29]

Constant (cm^{-1})	V = 0	V = 1	V = 2	V = 3
$\tilde{E}(V) - \tilde{E}(0)$	-	2558.913382	5027.33757	7405.2623
$\tilde{B}_V$	8.351030806	8.1190713	7.8876846	7.656200
$\tilde{D}_V \times 10^4$	3.442872	3.41316	3.38745	3.3683

Table 3.3: Spectroscopic constants of $H^{81}Br$ [28, 29]

Constant (cm^{-1})	V = 0	V = 1	V = 2	V = 3
$\tilde{E}(V) - \tilde{E}(0)$	-	2558.529082	5026.59650	7404.1938
$\tilde{B}_V$	8.348448996	8.116589	7.8853273	7.653943
$\tilde{D}_V \times 10^4$	3.440715	3.41043	3.38578	3.36666

Rotational relaxation processes of HBr are induced by collisions

$$HBr(V,J) + M \leftrightarrow HBr(V,J') + M \tag{3.2}$$

where M could be an HBr or a buffer gas molecule. The R-R rate constants $k_m(V, J' \leftarrow J)$ for $J,\ J' < 8$ were determined using ab-initio calculations for HBr and He as the collision partners [30].

Using the modified energy gap (MEG) fitting law [31] we extrapolated these calculated rate constants to $J,\ J' < 29$. The example of the state to state rotational relaxation rates for self collision of HBr are shown in Table 3.4.

For the collision between HBr and He, the example of the state to state rotational relaxation rates for the collision between HBr and He are shown in Table 3.5.

The vibrational relaxation processes can formally be divided into

$$HBr(V,J) + HBr(V,J) \leftrightarrow HBr(V+1,J) + HBr(V-1,J)\ , \tag{3.3}$$

Table 3.4: The state to state rotational relaxation rates ($\mathrm{m^3\,molecules^{-1}\,s^{-1}}$) for self collision of HBr.

J' J	0	1	2	3	4	5
0	-	3.5	2.34	1.27	0.56	0.20
1	1.26	-	2.87	1.56	0.69	0.25
2	0.59	2.00	-	2.34	1.04	0.38
3	0.28	0.97	2.09	-	1.91	0.69
4	0.13	0.45	0.97	2.00	-	1.56
5	0.06	0.19	0.41	0.86	1.85	-

Table 3.5: The state to state rotational relaxation rates ($\mathrm{m^3\,molecules^{-1}\,s^{-1}}$) for the collision between HBr and He.

J' J	0	1	2	3	4	5
0	-	0.78	0.57	0.36	0.19	0.09
1	0.28	-	0.67	0.42	0.22	0.10
2	0.14	0.46	-	0.57	0.31	0.14
3	0.08	0.26	0.51	-	0.49	0.22
4	0.04	0.14	0.28	0.51	-	0.42
5	0.02	0.08	0.15	0.28	0.49	-

for V-V processes,

$$HBr(V,J) + M \leftrightarrow HBr(V-1,J) + M \ , \tag{3.4}$$

for V-T processes where M could be an HBr or a buffer gas molecule, and

$$H^{79}Br(V,J) + H^{81}Br(V',J) \leftrightarrow H^{79}Br(V-1,J) + H^{81}Br(V+1,J) \ , \tag{3.5}$$

for isotopic V-V process. We assumed here that possible buffer gases do not have resonances near the vibrational energies of HBr.

These vibrational relaxation processes have been studied by infrared florescence excitation [32, 33, 34, 35]. The summarized forward rate constants of HBr are shown in Table 3.6.

Table 3.6: Forward vibrational relaxation rate constants of HBr ($\mathrm{m}^3\,\mathrm{molecule}^{-1}\,\mathrm{s}^{-1}$) at room temperature.

Relaxation process	Collision partner	Rate constant
V-V	HBr	3×10^{-18} [33]
V-T	HBr	1.8×10^{-20} [33]
	He	2.8×10^{-22} [34]
	H_2	6.4×10^{-21} [32]
isotopic V-V	HBr	1.5×10^{-17} [35]

Since HBr is a polar molecule, dipole-dipole interactions determine the R-R, V-V, V-T and isotopic V-V rates that are due to self-collisions. The kinetics and their temperature dependence are very complex and their exact modeling is beyond the scope of this thesis. However some assumptions and approximations were made to be able to study HBr laser performances particularly by our laser models[2]. To the best of our knowledge, there are no experimental data for the temperature dependence of R-R rate constants of HBr molecules with and without the presence of a buffer gas. We assume that the rates follow a $\sqrt{T}$ dependence known from hard sphere collisions [23].

The temperature dependence of the V-T rate constant for HBr self-collision processes has been measured [36]. The V-T rate takes on a minimum at 350 K and does not change much from 273 K to 500 K. We approximated the variation in this range also by a $\sqrt{T}$ law. There is no experimental data concerning the temperature dependence of V-T processes in the presence of a buffer gas as well as for isotopic V-V process. We approximated both rates with a $\sqrt{T}$ law. The variation of V-V

---

[2] Laser model will be discussed in chapter 6.

rate constants for HBr with temperature has been measured [37] and a scaling law of $T^{-3/4}$ was fitted to the data.

3.3 HCN molecule

HCN is a polyatomic molecule which consists of 3 vibrational normal modes as shown in Fig. 3.3. It should be noted that the second vibrational normal mode is doubly degenerate. The notation of HCN ($V_1V_2V_3$) refers to the energy levels of the normal CN stretch (V_1), bend (V_2), and CH stretch (V_3) modes, respectively.

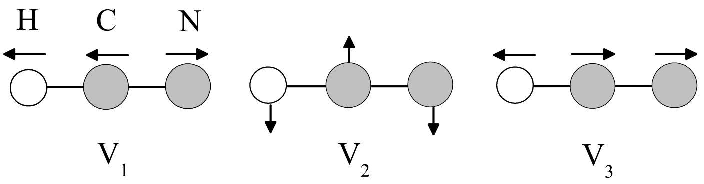

Figure 3.3: The vibration normal modes of HCN

For HCN, our interest is to excite the gas with laser sources emitting in the 1.5 μm region. In polyatomic molecules, it is possible to excite more than one vibrational normal mode simultaneously and such transitions are called combination bands. Excitation at 1.5 μm excitation is overlap to the combination band (002) of HCN as shown in Fig. 3.4.

Since HCN has three vibrational normal modes, there are several possible laser transitions that can originate from the upper pump level (002). Table. 3.7 shows the dipole allowed transitions from (002). We identified these transitions by applying spectroscopic group theory [16] to the HCN molecule.

More accurate transition wavelengths for the pump transition at 1.5 μm and the potential lasing transition at 3 μm of HCN can be obtained from Table. 3.8 and used

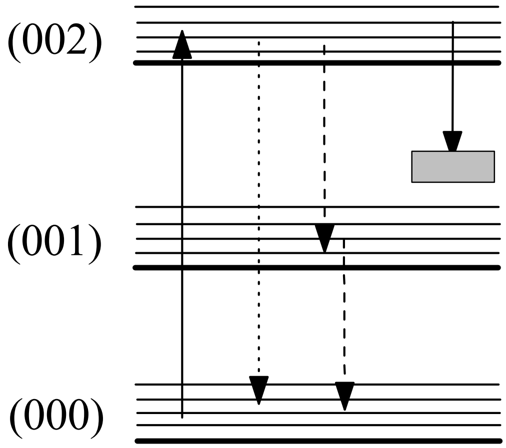

Figure 3.4: Energy level diagram of HCN molecule. The solid arrow denotes the pump transition at 1.5 μm. The dot and dashed arrows indicate the lasing transitions at 1.5 μm and 3 μm respectively as examples. The gray box stands for other potential lasing transitions of HCN.

Eq. (3.1). It should note that for HCN, $\tilde{D_V}$ is very small and can be neglected.

The HCN absorption cross section at 1.5 μm region has been estimated from HCN absorption spectra [19]. An absorption loss of about 0.2 dB/cm and a line broadening coefficient of about 45 MHz/torr (HWHM) for the peak absorption at 1535 nm were reported [19]. From this the absorption cross section is estimated to be between 4.8×10^{-22} m^2 to 1.8×10^{-22} m^2 for pressures from 1 torr to 10 torr.

The HCN cross section for stimulated emission from the transition (002) to (001) can be estimated from the absorption cross section of the transition (000) to (001) since these transitions have the same vibrational normal mode exchange i.e. (001). From the HITRAN database [40], the Einstein A coefficient of the transition (000) to (001) is about 37 s^{-1} for P and R branch transitions. By using this Einstein A coefficient and Eqs. (2.25) and (2.51), the absorption cross sections of the transition (000) to (001) are between 4.4×10^{-20} m^2 to 1×10^{-21} m^2 for pressures from 1 torr to 10 torr at room temperature.

Table 3.7: Examples of dipole allowed transitions that can originate from the terminal pumped state (002).

Dipole allowed transition	Approximate wavelength of transition(μm)
(002)→(000)	1.5
(002)→(010)	1.7
(002)→(100)	2.2
(002)→(110)	2.6
(002)→(001)	3
(002)→(120)	3.2
(002)→(011)	3.8
(002)→(200)	4.1
(002)→(130)	4.2
(002)→(021)	5.3
(002)→(140)	6
(002)→(031)	8.5
(002)→(150)	10.4
(002)→(111)	20
(002)→(041)	22

Table 3.8: Example of spectroscopic constants of $H^{13}CN$ [38, 39]

Constant (cm^{-1})	(000)	(001)	(002)
$\tilde{E}(V_1, V_2, V_3) - E(0,0,0)$	-	3293.513232	6483.27812
$\tilde{B}_{V_1,V_2,V_3}$	1.4399992	1.43037261	1.4204543

Typical state to state rotational relaxation rates of HCN are on the order of 15×10^{-16} (m^3molecules$^{-1}s^{-1}$) [41] which are about 5 times larger than that of HBr for $\Delta J = \pm 1$. The state to state rotational relaxation rates of HCN were estimated by multiplying by a factor of 5 to the state to state rotational relaxation rates of HBr shown in Table 3.4.

The pathways for vibrational energy relaxation in polyatomic molecules are difficult to predict. It is conceivable that those relaxation steps where the energy difference between the initial and final state is minimal are most probable [23]. In addition the difference in vibrational quantum numbers should also be small.

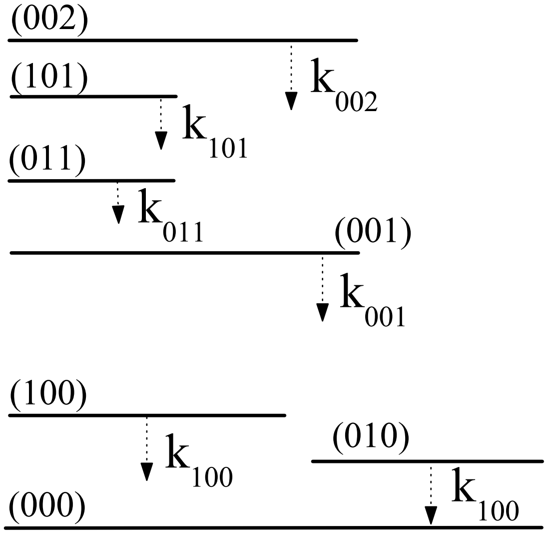

Figure 3.5: Simplified energy level diagram shows measured vibrational relaxation rates of HCN standing from the upper pump level (002)

Selected vibrational relaxation rate constants of HCN have been determined for various collision partners from laser-induced fluorescence decay experiments, which yield the total removal rates from the excited vibrational states (see Fig. 3.5).

Table 3.9 lists data for self-collision controlled removal rates (m^3molecules^{-1}s^{-1}) for various vibrational states of HCN at room temperature.

Details of the depopulation pathway of the (002) state have not yet been identified, however the dominant channel is likely [42],

$$(002) + (000) \rightarrow 2(001) \ . \tag{3.6}$$

The relaxation pathway of the (001) state is not fully understood [43, 44, 45]. It is likely initiated by the collision process [43],

$$(001) + (000) \rightarrow (100) + (010) \ , \tag{3.7}$$

Table 3.9: Self-collision controlled vibrational (removal) rate constants of HCN at room temperature.

$HCN(V_1V_2V_3)$	rate	vibrational rate constant
(002)	k_{002}	6.8×10^{-18} [42]
(001)	k_{001}	1.7×10^{-18} [43] 2.4×10^{-18} [44] 1.4×10^{-18} [45] 1.9×10^{-18} [45]
(100)	k_{100}	assumed $\simeq k_{001}$
(010)	k_{010}	$\gtrsim 2 \times 10^{-18}$ [45]
(101)	k_{101}	12.9×10^{-18} [46]
(011)	k_{011}	41×10^{-18} [47]

which could be followed by

$$(100) + (000) \rightarrow (000) + (000) \ , \tag{3.8}$$

and

$$(010) + (000) \rightarrow (000) + (000) \ . \tag{3.9}$$

These vibrational relaxation processes involve non-radiation pathways of molecules from the terminal pumped state (002) to the ground state (000). It should be mentioned that the vibrational relaxation process of the (100) state is assumed to have the same rate as the vibrational relaxation process in (100) due to their similar nature of the stretching mode.

In addition the vibrational relaxation processes,

$$(011) + (000) \rightarrow (001) + (010) \ , \tag{3.10}$$

and

$$(101) + (000) \rightarrow (100) + (001) \ , \tag{3.11}$$

were measured [46, 47].

It should be noted that the vibrational relaxations of HCN induced by buffer gases such as He and Ar have been studied [48, 42] using laser-induced fluorescence decay experiments. The processes are

$$(001) + M \rightarrow (120) + M \ , \tag{3.12}$$

and

$$(002) + M \rightarrow (121) + M \ , \tag{3.13}$$

where M is the buffer gas.

Table 3.10: Buffer gas-collision controlled vibrational (removal) rate constants (m^3molecules^{-1}s^{-1}) of HCN at room temperature.

HCN($V_1V_2V_3$)	M	vibrational rate constant
(001)	He	6.4×10^{-21} [48]
	Ar	6.5×10^{-21} [48]
(002)	He	5.6×10^{-21} [42]
	Ar	3×10^{-21} [42]

For the rotational relaxation of HCN controlled by buffer gas, no literature data are available.

3.4 C_2H_2 molecule

C_2H_2 has 5 vibrational normal modes as shown in Fig. 3.6. The fourth and the fifth vibrational normal modes are doubly degenerate. The notation of C_2H_2 ($V_1V_2V_3V_4V_5$) stands for the energy levels of the vibrational normal modes.

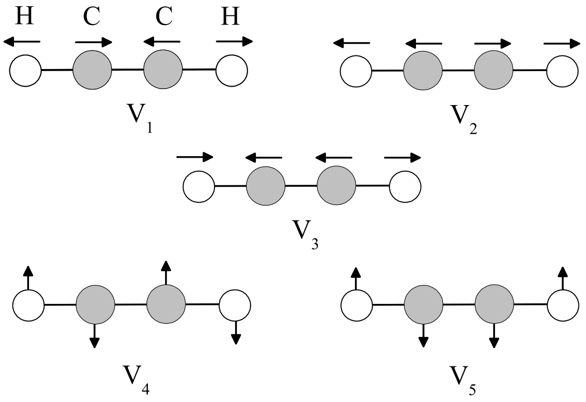

Figure 3.6: The vibration normal modes of C_2H_2.

The pump transition at 1.5 μm corresponds to the (00000) → (10100) transition. There are several potential lasing transitions as listed in Table 3.11.

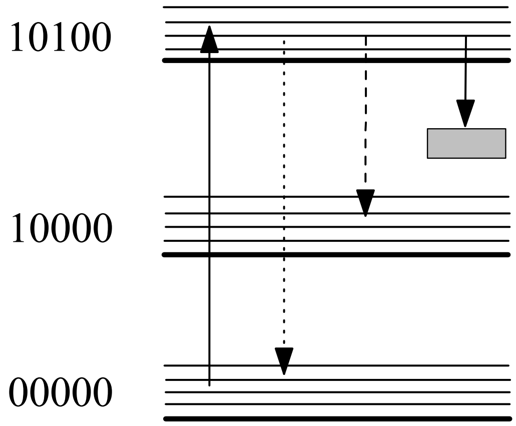

Figure 3.7: Energy level diagram of C_2H_2 molecule. The solid arrow denotes the pump transition at at 1.5 μm. The dot and dashed arrows indicate the lasing transitions at 1.5 μm and 3 μm respectively as examples. The gray box stands for other potential lasing transitions of C_2H_2.

More accurate transition wavelengths for the pump transition at 1.5 μm and the potential lasing transition at 3 μm of C_2H_2 can be obtained from Table 3.12 and used Eq.(3.1). It should note that for C_2H_2, $\tilde{D_V}$ is very small and can be neglected.

Table 3.11: Example on possible of dipole allowed transitions originating from the terminal pumped state(10100).

Dipole allowed transition	Approximate wavelength of transition(μm)
(10100)→(00000)	1.5
(10100)→(00010)	1.6
(10100)→(01000)	2.1
(10100)→(00100)	3
(10100)→(10010)	3.7
(10100)→(11000)	7
(10100)→(11010)	14

Table 3.12: Spectroscopic constants of C_2H_2 [49]

Constant(cm^{-1})	(00000)	(10000)	(10100)
$\tilde{E}(V_1,V_2,V_3,V_4,V_5)-\tilde{E}(0,0,0,0,0)$	-	3372.4	6555.9
$\tilde{B}_{V_1,V_2,V_3,V_4,V_5}$	1.177	1.170	1.164

A line broadening coefficient of about 6 MHz/torr (HWHM) for C_2H_2 was reported [50]. From the HITRAN database [40], the Einstein A coefficient of the transition (00000) to (10100) is about 4 s^{-1} for P and R branch transitions. By using this Einstein A coefficient and Eqs. (2.25) and (2.51), the absorption cross section is calculated to be between 8.8×10^{-22} m^2 to 7.2×10^{-22} m^2 for pressures from 1 torr to 10 torr.

The C_2H_2 cross section at 3 μm region from the transition (10100) to (10000) can be estimated from the absorption cross section of the transition (00000) to (00100) because these transitions have the same vibrational normal mode exchange i.e. (00100). From the HITRAN database [40], the Einstein A coefficient of the transition (00000) to (00100) is about 13 s^{-1} for P and R branch transitions. By using this Einstein A coefficient and Eqs. (2.25) and (2.51), the absorption cross sections of the transition (00000) to (00100) are between 2×10^{-20} m^2 to 1.4×10^{-20} m^2 for pressures from 1 torr to 10 torr at room temperature.

The state to state self collision of C_2H_2 has been measured [51] which is about 4 times smaller than the state to state rate the energy exchange of $\Delta \pm J = 1$ of HBr (see Table 3.4). We have multiplied the HBr rate constants in Table 3.4 by a factor of 0.25 in order to get the rotational relaxation rate constants for C_2H_2. The state to state rotational relaxation rate of C_2H_2 by a buffer gas (Ar) is about 1×10^{-16} ($\mathrm{m^3 molecules^{-1} s^{-1}}$) [52].

A summary of vibrational relaxation rates that have been reported are listed in Table 3.13. The vibrational relaxation process of the state (10100) has not been measured. However the expected value of k_{10100} should be in between the rate k_{00300} and k_{00100}.

Table 3.13: Self-collision controlled vibrational (removal) rate constants ($\mathrm{m^3 molecules^{-1} s^{-1}}$) of C_2H_2 at room temperature.

$C_2H_2(V_1V_2V_3V_4V_5)$	rate	vibrational rate constant
(10100)	k_{10100}	$4 - 7 \times 10^{-17}$
(00300)	k_{00300}	4×10^{-17} [52]
(00100)	k_{00100}	7×10^{-17} [53]
(00001)	k_{00001}	4×10^{-18} [54]

The depopulation pathway of the (00300) state has been studied by the infrared-ultraviolet double-resonance technique (IRUVDR). The vibrational relaxation process is according to [52]

$$(00300) + (00000) \rightarrow (11120) + (00000)\ . \tag{3.14}$$

The vibrational relaxation process of the (00100) state has also been investigated by the IRUVDR technique. The vibrational pathway is [53],

$$(00100) + (00000) \rightarrow (01010) + (00001)\ . \tag{3.15}$$

From the similar nature of the vibrational states involving the stretching vibrational normal mode(s) of states (00300), (10100) and (00100), we assume the vibrational relaxation of the (10100) having a value that is of the same order of magnitude as the V-V rates of the state (00300) and (00100).

In addition, the V-V rate of the process,

$$(00010) + (00000) \rightarrow (00000) + (00000)\ , \tag{3.16}$$

has been calculated [54].

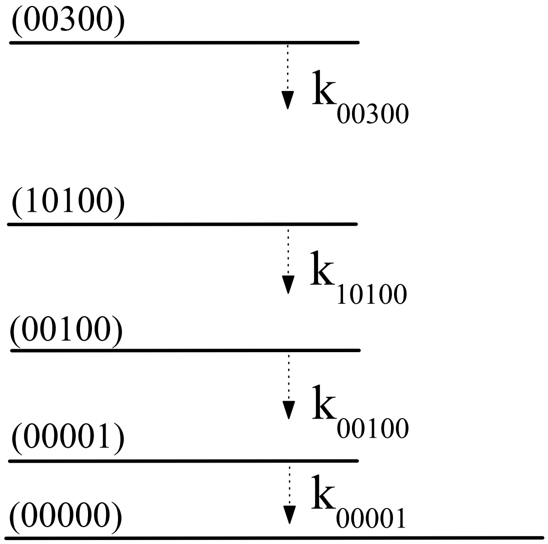

Figure 3.8: Simplified energy level diagram shows vibrational relaxation rates of C_2H_2

It should be mentioned that vibrational relaxation of C_2H_2 due to collisions with buffer gases has been reported for the (00100) state [55]. However the energy pathway of the collision has not been identified. The rates are 1.57×10^{-19} m^{3}molecules^{-1}s^{-1} for Ar and 1.37×10^{-19} m^{3}molecules^{-1}s^{-1} for Kr [55].

3.5 HI molecule

HI is a diatomic molecule and thus has only one vibrational normal mode as shown in Fig. 3.9. The second overtone absorption line of HI falls into the 1.5 μm region and therefore the molecule can be potentially pumped by C-band lasers. According to the HITRAN database [40], the Einstein A coefficients for the pump transitions (A_{pump}) is about 0.06 s^{-1} for the second overtone transition. The Einstein coefficients $A_{P,R}$ for the laser transitions are 0.12 s^{-1} for P and R branches of the fundamental (V to V-1) transitions. The pressure broadening coefficient of HI is 3.6 MHz/torr (HWHM) [56]. Table 3.14 exemplifies the cross section of HI obtained from Eqs. (2.25) and (2.51) at room temperature and pressure of 20 torr for overtone R(4) transitions.

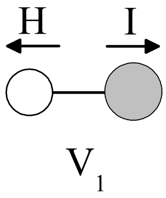

Figure 3.9: The vibration normal mode of HI.

Table 3.14: Transition wavelengths and cross section for fundamental and second overtone of HI at room temperature and a pressure of 20 torr.

Pump	wavelength(μm)	$\sigma(\nu_o)$m^2
fundamental	4.3691	3.42×10^{-22}
second overtone	1.5392	1.44×10^{-23}

The transition wavelengths of HI can be calculated by using the spectroscopic constants in Table. 3.15 and used Eq. (3.1). For HI, $\tilde{D_V}$ is small and can be neglected.

Table 3.15: Spectroscopic constants of HI [57]

Constant (cm^{-1})	V = 0	V = 1	V = 2	V = 3
$\tilde{E}(V) - \tilde{E}(0)$	-	2229.5817	4379.2261	6448.0348
$\tilde{B}_V$	6.426322	6.255213	6.082917	5.098767

The vibrational relaxation processes,

$$HI(V,J) + HI(V,J) \leftrightarrow HI(V+1,J) + HI(V-1,J) \ , \tag{3.17}$$

have rate constants for the V-V process of 2.2 $\times 10^{-19}$ $\text{m}^3\text{molecules}^{-1}\text{s}^{-1}$ [58]. For the V-T process

$$HI(V,J) + HI \leftrightarrow HI(V-1,J) + HI \ , \tag{3.18}$$

the rate of 1.2 $\times 10^{-20}$ $\text{m}^3\text{molecules}^{-1}\text{s}^{-1}$ [59]. Rotational relaxation process have not yet been reported.

3.6 Heat capacity, thermal conductivity and gas properties

Heat capacities and thermal conductivities of gases involved in this thesis are listed in Table.3.16. If the gas consists of a mixture of an active gas (index a) and buffer gas (index b) with partial pressure p_a and p_b, heat conductivity κ and the heat capacity C can be written as [62],

$$\kappa = \frac{p_a \kappa_a + p_b \kappa_b}{p_a + p_b} \ , \tag{3.19}$$

and

$$C = \frac{p_a \ C_a + p_b \ C_b}{p_a + p_b} \ . \tag{3.20}$$

Table 3.16: Heat capacity and thermal conductivity [60, 61].

gas	Heat capacity ($\mathrm{J/mol \cdot K}$)	Thermal conductivity$\times 10^{-3}$ ($\mathrm{W/m \cdot K}$)
HBr	20.82	8.9
HCN	28.6	11.87
C_2H_2	33	18.51
HI	20.79	5.694
He	12.5	142.64
Ar	12	16.36
Kr	12	8.834

The brief descriptions and boiling temperature of gases are also listed in Table 3.17.

Table 3.17: Gas properties [61].

gas	Description	Boiling temperature (K) at 1 atm
HBr	colorless, toxic and corrosive	206.45
HCN	colorless, toxic and flammable	298.85
C_2H_2	colorless and highly flammable	189.15
HI	colorless, toxic and corrosive	237.55
He	colorless, odorless and tasteless	4.22
Ar	colorless, odorless and tasteless	87.28
Kr	colorless, odorless and tasteless	119.8

3.7 Summary

The three molecular gases that are of interest to this thesis have been discussed in detail. The spectroscopic data such as transition wavelengths, cross sections, kinetic rate constants are essential for estimations and interpretations in the context of relevance to OPML applications. Their spectroscopic constants (for example rotational constants) were obtained from the available literature. Possible lasing transitions were identified by dipole selection rules. Data for various relaxation rate constants and the effect of buffer gas on the rate constants are obtained or extrapolated from literature values. In addition, the molecular constants and spectroscopic data for another potential molecular gas laser medium HI are also provided for future studies.

Chapter 4

Optically pumped HBr laser

4.1 Introduction

As outlined in the preceding chapter, HBr is a potential molecule that can be pumped by solid state lasers and emits in the attractive 4 μm wavelength region. Several optically pumped overtone HBr lasers have been demonstrated. Lasing at $\sim$ 4 μm has been observed when optically pumped with a nanosecond pulsed optical parametric oscillator (OPO) on the first overtone of HBr [25] at $\sim$ 2 μm. It has been proposed by Jones [4] that Tm:YAG lasers emitting in the range of 1.9–2.2 μm can be used to excite the first overtone transition of HBr. The third overtone excitation of HBr by Nd:Glass laser emitting at 1.05 μm has been reported [63]. The second overtone of HBr pumped by a 1.34 μm Nd:YAG laser was demonstrated by our laboratory [9].

In this chapter, we focus on the improvements on the HBr laser pumped on its second overtone by a 1.34 μm Nd:YAG laser [64]. Section 4.2 presents our approach for frequency shifting, line narrowing and stabilization of a pulsed Nd:YAG laser that was used for the second overtone excitation. Section 4.3 describes the characterization of the HBr molecular gas laser. The goal of this was to improve our understanding of second overtone pumped HBr lasers and together with simulations explore fundamental performance limits and energy scaling.

4.2 Q-switched Nd:YAG laser for optical pumping of HBr

The Nd:YAG laser used to excite the second overtone of HBr is a modified flashlamp pumped SEO Schwartz 1-2-3 laser with a linear cavity. The cavity mirrors have high reflectivity in the 1.3 μm region and low reflectivity in the 1 μm region in order to prevent lasing at the much stronger 1.06 μm line.

The pump laser was modified by Kletecka et al [9] to emit a narrow band Q-switched pulse at 1.34 μm to pump the V=0, J = 4 to V=3, J = 5 transition of the 79 isotope of HBr. In this section we describe improvements made to the pump laser during this thesis. These improvements concern:

1. the temperature tuning of the emission of the Nd:YAG active medium,
2. the frequency tuning and single-mode selection using a birefringent filter,
3. the stabilization of the Nd:YAG cavity length to the frequency of the seed laser.

Before we discuss the details, let us look at the final layout of the pump laser, see Fig.4.1. The Nd:YAG is Q-switched using an acousto-optic modulator. The quater-wave plates prevent standing waves in the laser crystal. A diode seed laser is stabilized to a reference HBr cell. The seed light is coupled through the first diffraction order into the YAG cavity. This incoupling is switched-off when the Q-switch is fired. Provided the YAG cavity has the correct length, the seed photons initiate lasing at the correct wavelength. The detection of the Nd:YAG fluorescence

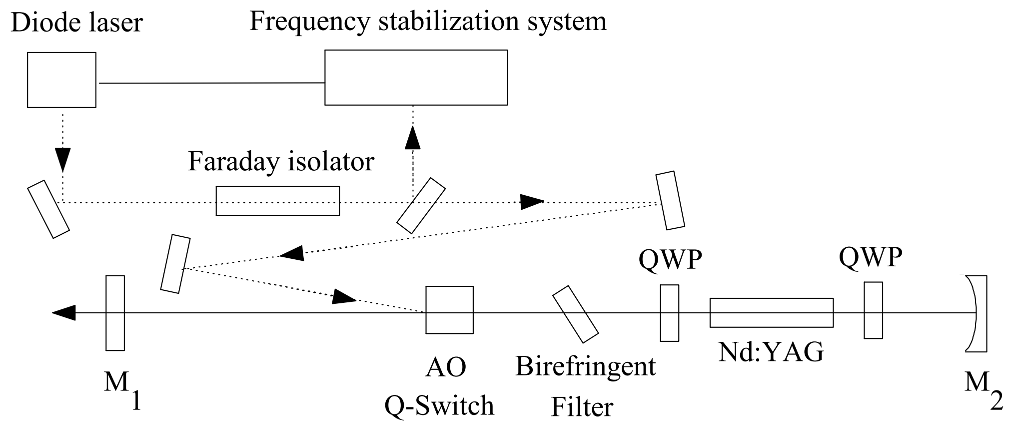

Figure 4.1: Schematic diagram of the Q-switched, injected seed Nd:YAG laser. M_1 is the outcoupling mirror having a reflectivity of 0.70 and M_2 is the rear mirror with high reflectivity at 1.34 μm. QWP stands for quarter wave plate.

was performed to determine the potential lasing line of the Nd:YAG laser in the 1.3 μm region to excite the HBr molecule. The cavity mirrors of the Nd:YAG laser were removed. The fluorescence from the Nd:YAG crystal was collected via lenses and sent into a Czerny-Turner spectrometer. The signal out of the spectrometer was detected by a InGaAS photodiode and averaged using a lockin amplifier. The detected Nd:YAG fluorescence is shown in Fig. 4.2 along with the second overtone transitions (P and R branches) of HBr. There are a number of the promising Nd:YAG lines to excite the second overtone of HBr. However, we chose the 1.339 μm line because it is the strongest transition in the 1.3 μm region that overlaps with the second overtone absorption lines of HBr. The measurements also show the difficulty to match the HBr absorption and Nd:YAG laser because the Nd:YAG fluorescence does not lie perfectly at the HBr absorption. In addition the absorption linewidth of HBr is on the order of a few hundred Megahertz. In order to match the emission of the Nd:YAG to the correct HBr absorption, we used temperature tuning of the Nd:YAG emission wavelength. The spectrum of Nd:YAG moves to longer wavelengths when the Nd:YAG crystal is heated. To tune the peak of the Nd:YAG fluorescence to a HBr

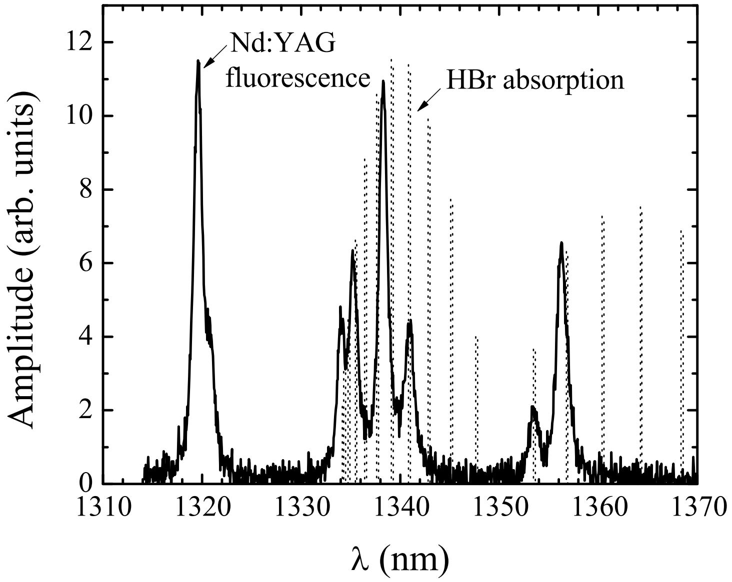

Figure 4.2: Nd:YAG fluorescence in the 1.34 μm region overlapped with with R and P branch absorption lines (second overtone transitions) of HBr

absorption line, a 4 MHz linewidth Newport diode laser was used as the reference. The diode laser was divided into two beams. The first beam was triple-passed through a 50 cm long HBr absorption reference cell at a pressure of 30 torr. This path of the diode laser was monitored and locked by the standard PID (proportional-integration-differentiation) system control to ensure that the diode laser is on the absorption dip of HBr. The second beam was sent to the spectrometer overlapping spatially with the fluorescence beam of the Nd:YAG. A circulating bath with a mixture of ethylene glycol and water was used to adjust the temperature of the Nd:YAG rod. The fluorescence was recorded as a function of the bath temperature with a spectral resolution of about 0.4 nm. Fig. 4.3 shows the temperature tuning results. It is concluded that a temperature of 105 C° is needed to reach the HBr transition. From the slope of $\lambda(T)$ a temperature tuning coefficient of 0.0073 nm/K was determined for the wavelength of 1.339 μm Nd:YAG emission. In the free-running condition, the Nd:YAG laser does not oscillate in the necessary single longitudinal mode regime.

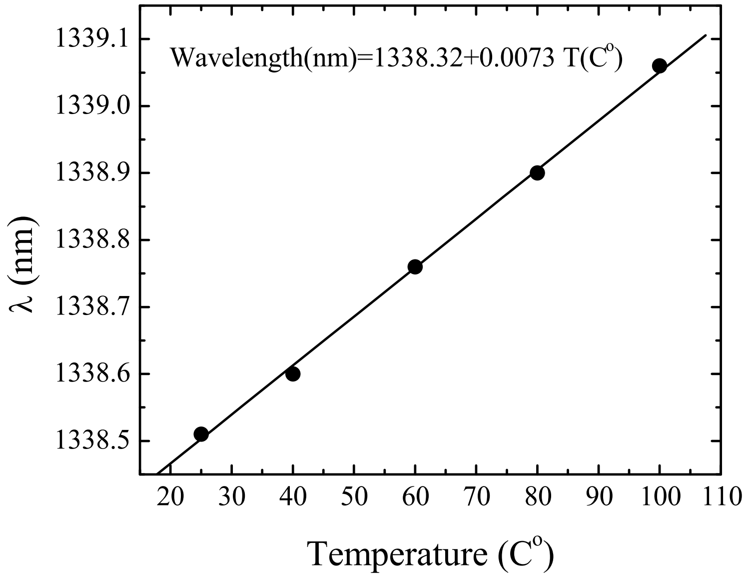

Figure 4.3: Temperature tuning of the Nd:YAG fluorescence in the 1.34 μm region. The target wavelength, R(4) HBr absorption is at 1.33909 μm which corresponds to the temperature of the chiller at 105 C°.

One reason is spatial hole-burning which can be avoided by placing the Nd:YAG rod between quarter-wave plates. Furthermore a birefringent filter was implemented to select the correct oscillation frequency and tune the Nd:YAG to the spectral range of interest (see Fig. 4.4). This filter was designed to prevent the laser from lasing at other wavelengths especially at the 1319 nm line (see Fig. 4.4). To efficiently pump the molecular gas, the pump source must have a narrow linewidth. For this reason, the Nd:YAG laser was injection seeded with a diode laser locked to the desired HBr transition in order to further reduce the laser bandwidth to a few hundred MHz. A schematic of the injection seeded and Q-switched Nd:YAG laser with the birefringent filter is shown in Fig. 4.1.

A stable resonator configuration was chosen to produce a high-quality TEM_{00} output beam. A 100% reflecting rear mirror of 5 m radius of curvature and a 70% reflecting 4 m radius of curvature output coupler spaced about 1.5 m apart formed

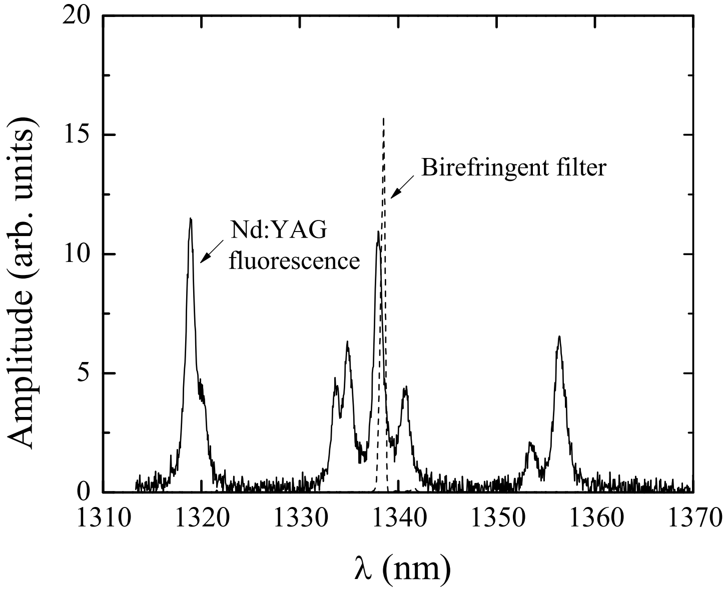

Figure 4.4: Nd:YAG fluorescence with birefringent filter (dashed line). The Nd:YAG fluorescence is also plotted (solid line) without the birefringent filter.

the laser cavity. The free spectral range was 100 MHz. As stated before, to suppress the much stronger laser transitions in the 1.06 μm region, the cavity mirror coatings were chosen to have a very low reflectivity in the 1 μm region.

The seed diode is the same diode laser used in the fluorescence measurement. As has been done before in the fluorescence measurement, a part of the diode laser was triple-passed through a 50 cm reference cell filled with 30 Torr HBr and the absorption of the R(4) second overtone transition of HBr was monitored continuously using a photodiode which provided a feedback signal through the PID control system to ensure that the diode frequency was always locked to the desired absorption line of HBr. The rest of the diode laser was continuously injected and aligned to be co-linear with the Nd:YAG along the first diffraction order of the Q-switch as long as the Q-switch is on and the Nd:YAG is prevented from lasing. The seed makes multiple roundtrips in the Nd:YAG cavity.

Typical seed injection power was 1.5 mW in the first order. The leakage of the seed beam through the rear mirror of the Nd:YAG cavity was monitored by an InGaAs photodiode, which served as a probe for active monitoring of the cavity resonances at the seed frequency. This probe also served to monitor the fluctuations (thermal, mechanical) of the cavity in the absence of lasing. Suitable mode matching optics were introduced in the seed beam to enable proper mode matching of the diode laser and the Nd:YAG laser inside the Nd:YAG cavity.

When the flash lamp is fired and the Q-switch is off, the seed beam is no longer injected into the Nd:YAG cavity. Under optimum conditions the remaining seed photons in the cavity are efficient to control the frequency of the Nd:YAG output and ensure that the frequency difference is less than the absorption line width of HBr.

In order to optimize the injection seeding, the Nd:YAG cavity needs to be in resonance with the mode of the seed laser. To obtain the optimum, cavity length adjustment is required. Thus the output coupler (M_1) was mounted on a piezo electric translation stage. At the correct cavity length, the pulse build-up time of the Nd:YAG laser is the shortest and the emission is in a single mode. However if the seed diode frequency does not match with any longitudinal mode frequency of the Nd:YAG cavity, the Nd:YAG laser starts from noise (spontaneous emission of the Nd:YAG) resulting in a longer build up time and multi-mode lasing.

Figure 4.5 shows the measured pulse build-up time and the Nd:YAG cavity resonance as a function of cavity mirror position as the Nd:YAG cavity was ramped through the free spectral range. The slew rate of the ramp in terms of the free spectral range was 200 MHz/s. As is evident, at low seed power, the shortest pulse build-up times occur near the peak of the cavity resonance. From these graphs the time can be determined at which the Nd:YAG laser should be triggered for optimum performance.

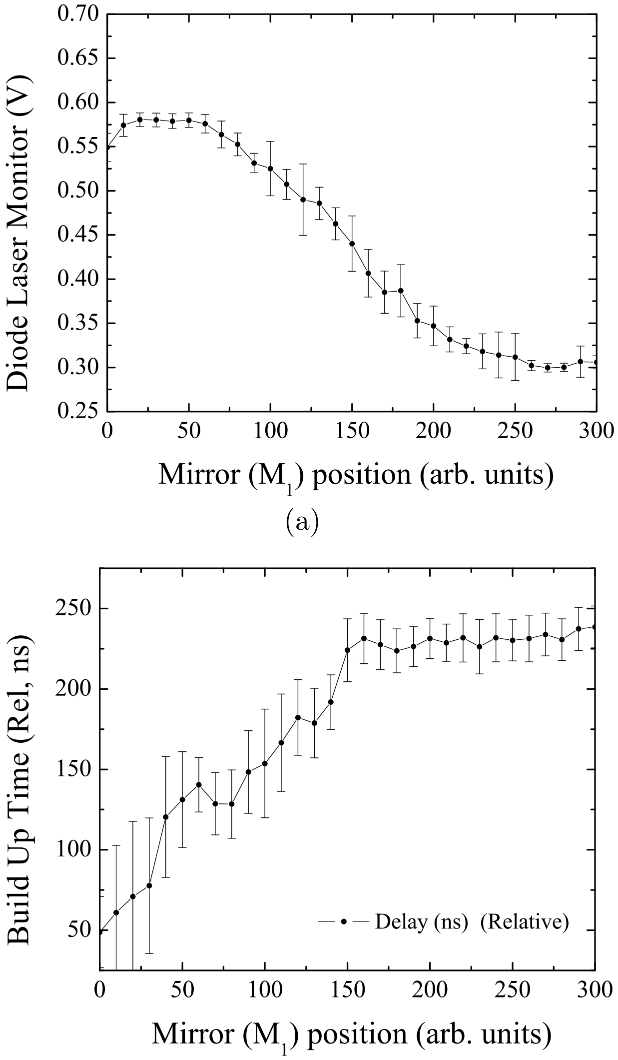

(a)

(b)

Figure 4.5: (a) Transmission diode signal from the Nd:YAG cavity as a function of the position of the M_1 mirror translated with a piezo-transducer. (b) Pulse build-up time as a function of the position of the M_1 mirror.

Shortest build-up times also meant single mode emission as shown in Fig.4.6. For the practical operation of the Nd:YAG laser a saw-tooth ramp was applied to the piezo stage and the transmitted diode signal was monitored. The Q-switch was fired when the diode signal reached a certain value. This method was preferred over a

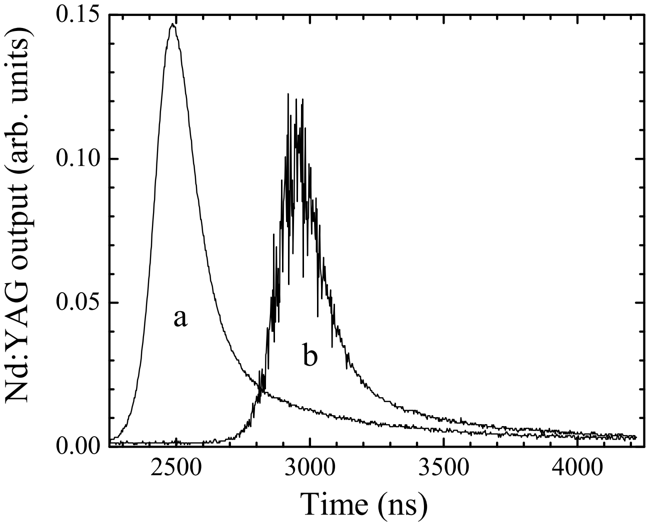

Figure 4.6: The single mode emission (a) versus multi-mode emission (b) of the Nd:YAG laser.

more traditional cavity stabilization scheme because it reduced the impact of thermal fluctuations and noise. The downside was that an exact repetition rate could not be set. This, however, is of little importance for most OPMLs. Output energies between 20 mJ and 50 mJ were obtained in a single mode at the correct frequency. These energies were limited by the small-size Nd:YAG system available to us.

4.3 Characteristics of the HBr laser output

Suitable mode matching optics were used to couple the Nd:YAG output to the HBr cavity efficiently. The Nd:YAG laser makes a double-pass in a 1-m long tube filled with 25 Torr of HBr. The HBr cavity is sketched in Fig.4.7. The pump and HBr beams were separated using a pair of CaF_2 dispersive prisms to facilitate multiple pump passes and for independent control of the pump. The HBr was pumped on its R(4) of the second overtone transition using 60 mJ, 200 ns pulses from the pump laser. The laser output was sent to a monochromator (ORIEL model 77700A). The

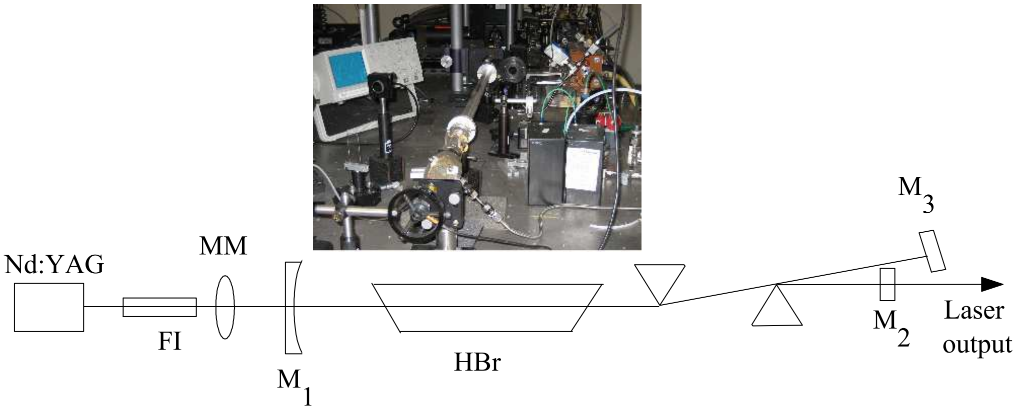

Figure 4.7: Layout of HBr cavity. FI-Faraday isolator, MM-mode-matching optics. M_1 and M_2 form the HBr cavity and M_3 is a flat mirror for retro-reflecting the pump.

output from the monochromator was detected by a cooled-InSb detector and was averaged using a lockin amplifier. We have observed lasing on 5 different transitions of the V(3→2) and V(2→1) manifold as shown in Fig.4.8. The spectral resolution was 12 nm although the specification of the monochromator was 4 nm. From our HBr laser simulation[1], we believe some of the transitions are being suppressed by CO_2 absorption particularly the line V(2→1)P(6→ 7) and V(2→1)P(5→ 6). To reduce CO_2 absorption, the amount of cavity exposed to the atmosphere must be reduced.

At this point we decided that we had enough experimental evidence to continue with modeling to draw conclusion concerning energy scalibility and frequency tunability of HBr lasers. A practical issue was that the seed diode laser broke and could not be repaired. Apparently the specific wavelength of 1300 nm was not in the standard production line of Newport and would have required lengthly and costly custom development with a somewhat uncertain outcome. From here on we concentrated on experimental effort on C_2H_2 and HCN OPMLs.

---

[1] will be discussed in chapter 6

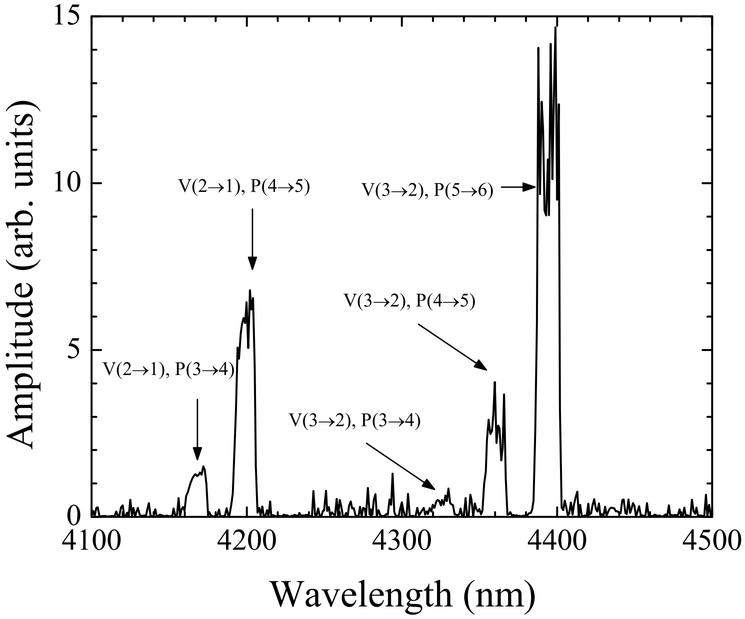

Figure 4.8: HBr spectral output in the 4 μm region

4.4 Summary

Single frequency emission of a Nd:YAG laser at the second overtone absorption of HBr has been demonstrated using a combination of temperature tuning, injection seeding and controlling the length of the cavity. The laser is used to optically pump an HBr laser. Five lasing transitions in the mid-infrared region have been observed from the HBr laser.

Chapter 5

Optically pumped C_2H_2 and HCN lasers

5.1 Introduction

Narrow band and high power telecommunication C-band (diode and fiber) lasers are attractive pump sources for OPMLs. As mentioned previously, gases such as C_2H_2 and HCN have strong absorption lines in this spectral range and have been used as frequency standards for stabilized diode and fiber lasers in the near IR regime. Thus they can be excited by well developed high-power diode lasers or fiber lasers at 1.5 μm. When pumped with C-band lasers, C_2H_2 and HCN emission wavelengths are between 1.5 μm and 20 μm owing to their multi-vibrational modes as discussed in chapter 3. These make C_2H_2 and HCN potential candidates for C-band beam combiners. A number of optically pumped C_2H_2 and HCN lasers have been reported. A CW CO-C_2H_2 laser at 8 μm has been demonstrated as means to transfer pump photons at 4 μm from vibrationally excited CO to C_2H_2 [65]. C_2H_2 super radiant pulse emissions of 13.6 μm and 15.6 μm excited by a narrow band optical parametric oscillator (OPO) at 3 μm were observed [66]. A CW optically (2.5 μm) pumped HF-HCN at 3.8 μm laser was demonstrated based on vibrational energy transfer from excited HF molecules to HCN molecules [67]. To the best of our knowledge, we were the first to explore and to demonstrate the optically pumped C_2H_2 and HCN lasers based on the excitation at 1.5 μm [68].

In this chapter, we describe the demonstrations of the optically pumped C_2H_2 and HCN lasers. Section 5.2 describes fluorescence measurements of C_2H_2 and HCN. The measurements served to evaluate the prospects of using both gases as laser media. The observation of CW fluorescence at about 3 μm for C_2H_2 and 3 μm and 4 μm for HCN suggested the possibility to demonstrate laser action. We first investigated amplified spontaneous emission (ASE) and then set up gas lasers with optical cavities (section 5.3).

5.2 CW fluorescence of C_2H_2 and HCN

The schematic diagram of the CW fluorescence detection of C_2H_2 and HCN is shown in Fig.5.1. The CW fiber laser used in this experiment is an IPG photonics laser, EAR-5k-C2-SF with a (collimated) output beam diameter of 1.6 mm and output power of 5 W. This fiber amplifier is seeded by a 1 mW New Focus diode laser (model Velocity 6300).

A fraction (0.5%) of the laser beam is used to probe the absorption of a reference cell containing either (C_2H_2 at 50 torr or HCN at 100 torr). The 4-cm long fluorescence cells were filled with C_2H_2 and HCN at 1 torr and 5 torr, respectively. The cell windows are made out of the fused silica. The fluorescence cells were supplied by Scientific Glass CO. Ltd. for C_2H_2 and Technical Glass, Inc. for HCN. The pump beam was focused by a lens (f_2 = 25.4 cm) to excite the gas media. The side fluorescence was collected and focused into a monochromator (ORIEL model

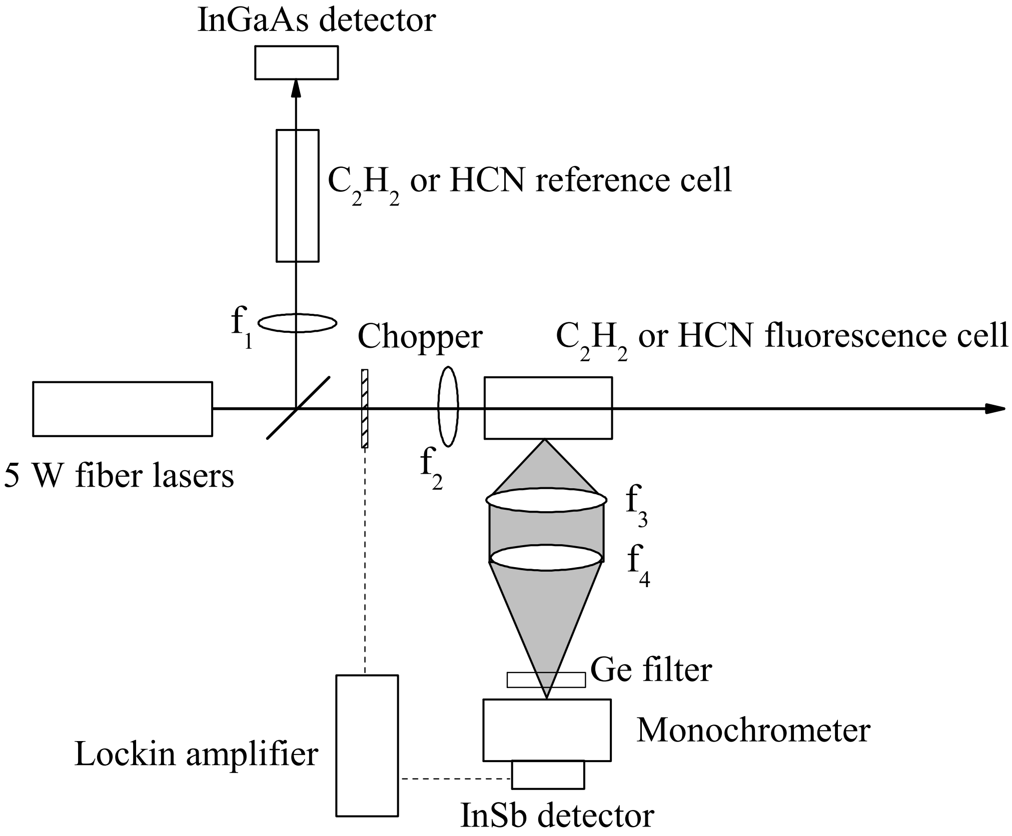

Figure 5.1: Experimental layout of CW fluorescence detections of C_2H_2 and HCN .

77700A). The collection optics ($f_3 = 2.54$ cm and $f_4 = 10.16$ cm) were designed to match the F-number of 3.9 of the monochromator.

A Ge window with transmission from 1.6 μm to 12 μm was used to block the pump radiation. The output from the monochromator was measured with a cooled-InSb detector and a lockin amplifier with a time constant of 1 second. It was verified that the fluorescence signals vanish when the fiber laser was tuned away from the gas absorption.

The measured fluorescence signals are plotted in Fig. 5.2. Since the signals were rather small and our focusing optics were not optimized, opening the slits of the monochromator was necessary which resulted in low spectral resolutions.

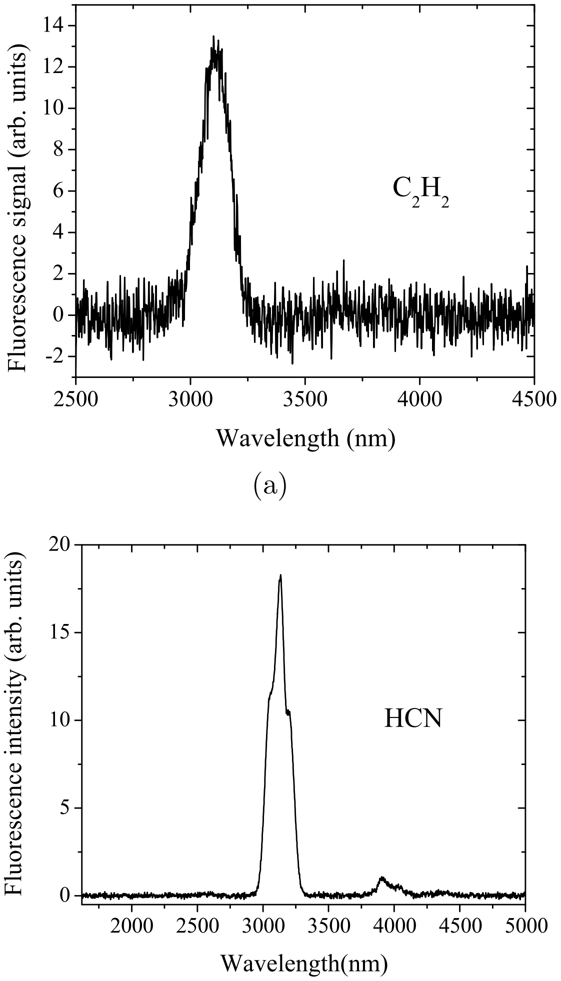

(a)

(b)

Figure 5.2: The detected fluorescence signals (a) C_2H_2 (b) HCN. The excitation source was a 5 W laser at about 1535 nm. C_2H_2 the transition P(19) was excited. HCN the transition R(7) was excited.

The monochromator was scanned form 1.5 μm to 5 μm The detector's spectral response was from 1 to 5 μm. We observed one spectral component for C_2H_2 at about 3.0 μm, and for HCN we found two spectral components at about 3 μm and 4 μm, respectively. The observed fluorescence from C_2H_2 is produced by a transition from (10100) to (10000). This transition is dipole allowed as discussed in section 3.3 and 3.4. The two fluorescence components from HCN correspond to the transition from (002) to (001) for 3 μm region and from (002) to (011) for the component at $\sim$ 4 μm region.

5.3 C_2H_2 and HCN lasers pumped by a ns pulse OPO

5.3.1 Experimental setup

The fluorescence measurements suggest that lasing at 3 μm is most likely. However to increase the possibility to obtain the gain required for 3 μm lasing, a ns OPO was used as the pump source. This OPO is a commercial system provided by Laser Vision. The pulse duration of the OPO is about 5 ns operating at 10 Hz repetition rate. The OPO bandwidth at 1.5 μm is about 3.5 GHz.

The schematic of the optically pumped C_2H_2 and HCN laser is shown in Fig. 5.3. For the C_2H_2 laser, an 80 cm gas cell filled with 2.2 torr of gas was used. The gas was optically pumped by the nanosecond OPO tuned to the R(7) absorption line at 1.521 μm. The absorbed pump energy was about 2.3 mJ. Lasing action could be observed for absorbed pumped energy exceeding 100 μJ. The OPO pump was sent and focused to the center of the cell by a 2 m focal length lens which produces a pump spot of diameter of about 4 mm. The 1.4 m long laser cavity consisted of two 5 m concave mirrors having a high transmission to the pump wavelength and a reflectivity of 0.9 in the 3 μm region. Since the substrate material of the available mirrors was BK7 which has a very low transmission at the laser wavelength, the laser output was detected from the reflection off a CaF_2 window inside the laser cavity.

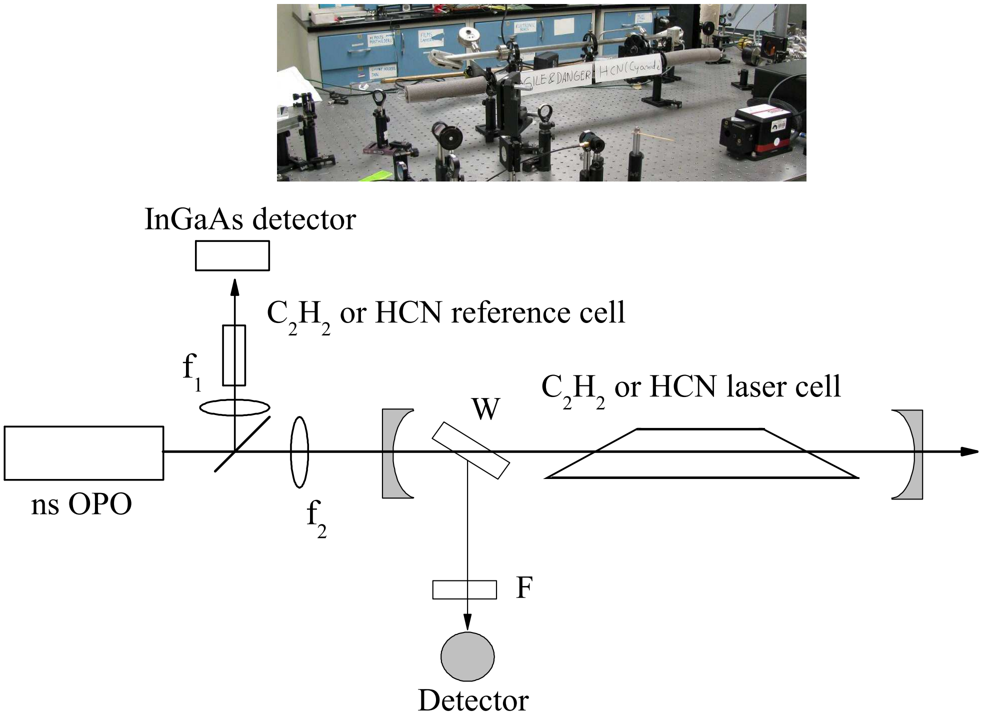

Figure 5.3: Experimental layout of optically pumped C_2H_2 and HCN lasers.

For the HCN laser, a 4 cm HCN cell filled with 5 torr was optically pumped by the OPO to excite the R(9) absorption line at 1.536 μm. The laser cavity length was 73 cm. The OPO pulse was focused to the center of the cell using a 1 m focal length lens producing a pump spot diameter about 2 mm. The 0.5 m concave front cavity and the rear end mirrors were transparent to the pump wavelength and had a reflectivity of 0.9. The absorbed pump energy was about 140 μJ. The laser threshold occurred at 40 μJ of absorbed pump pulse energy. In the case of HCN, the laser output was detected from the reflection off the HCN cell window.

It is worth mentioning that ASE emission (direct output) were observed for C_2H_2 and HCN (no external cavity mirrors). In these experiments, the OPO pump was focused to the center of the cells by a 1-m focal length lens resulting in a spot of diameter of about 2 mm. The length of the cells were 80 cm with C_2H_2 filled at 2 torr and 1 m HCN filled at 5 torr. The ASE emissions were observed for absorbed pump energies exceeding 200 μJ and 415 μJ, for C_2H_2 and HCN respectively.

The laser and the ASE spectra were recorded by the monochromator used in the CW fluorescence detection. The temporal profiles of the laser output and ASE emission were detected by a fast detector.

5.3.2 Results and discussion

The observed spectrum of the C_2H_2 laser is shown in Fig.5.4(a), an example temporal laser profile is depicted in Fig.5.4(b). The corresponding ASE traces are shown as insets. The laser emission shows two peaks separated by about 40 nm in the 3140 nm region. The two peaks correspond to the R(7) and P(9) transition. Both originate at the upper pump level with J = 8 of the (10100) vibrational state and terminate at J= 9 in the (10000) vibrational state as shown in Fig.5.5.

The two spectral laser components do not represent transitions from the allowed rotational states adjacent to the pumped level to the (10000) vibrational level. Their wavelength separation would be about 9 nm, which is estimated from the known value of the rotational constant for the (10100) state as provided in chapter 3. The rotational relaxation time of the pumped level is about 18 ns for a pressure of 2.2 torr, hence one would not expect any laser transitions to occur from the neighboring states during the pump pulse. It is instructive to note the absence of any emission signature from the lower laser state (10000) to the ground state (00000), which would be at about 3 μm. This transition is not dipole allowed.

The exact temporal profile of the laser output fluctuated somewhat from shot to shot and was slightly dependent on the cavity alignment. It reflects a superposition of longitudinal and transverse modes and showed the typical mode beating frequencies.

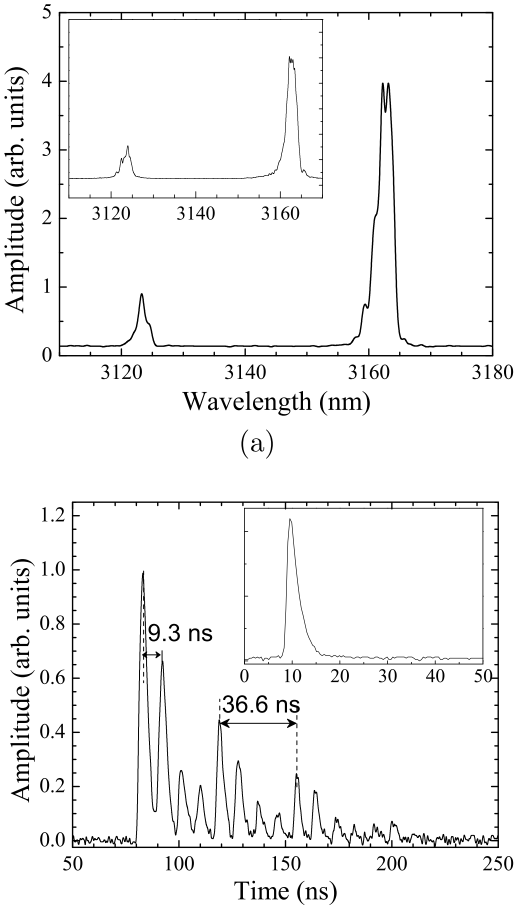

(a)

(b)

Figure 5.4: C_2H_2 laser pumped with 5-ns pulses at R(7)(a) spectrum (b)temporal profile. The insets show the ASE spectrum and temporal profile.

The longitudinal mode spacing is given by [69],

$$\Delta\nu_L = \frac{c}{2L} \ , \tag{5.1}$$

where L is the laser cavity length.

The transverse mode spacing is given by [69],

$$\Delta\nu_T = \Delta\nu_L \frac{1}{\pi} \cos^{-1}\left(\sqrt{g_1 g_2}\right) \ , \tag{5.2}$$

where the parameter g_i is defined as

$$g_{1,2} = \left(1 - \frac{L}{R_{1,2}}\right) \,, \tag{5.3}$$

where $R_{1,2}$ is the radius of curvature of the cavity mirror.

From our cavity geometry of C_2H_2 laser, $\Delta\nu_L \sim 107$ MHz(~ 9 ns) and $\Delta\nu_T \sim 26$ MHz (~ 38 ns) by using Eqs. (5.1) and (5.2). Therefore the observed periods of 9.3 ns and 36.6 ns are in agreement with what one expects from the cavity and mirror geometry.

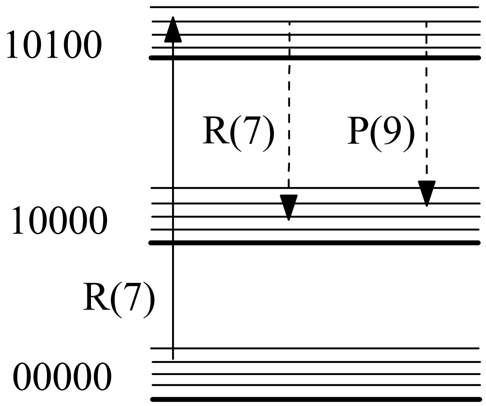

Figure 5.5: The observed laser transitions of optically pumped C_2H_2

Figure 5.6 shows the spectral and temporal profile of the HCN laser and ASE. The spectrum in Fig. 5.6(a) shows a main peak at $\sim$ 3165 nm. The peak corresponds to the P(11) transition originating from the initially populated level J = 10 of the (002) vibrational state. The observed structure in the short-wavelength tail of the peak is likely from P line emission originating at adjacent rotational states (J = 8 and J = 9) because of the short ($\sim$ 5ns) rotational relaxation time.

The modulation of the temporal profile is attributed to transverse mode beating.

The temporal spacing between transverse modes in the HCN cavity was estimated to be 79 MHz (by using Eq.(5.2)) which corresponds to 12.6 ns mode beating.

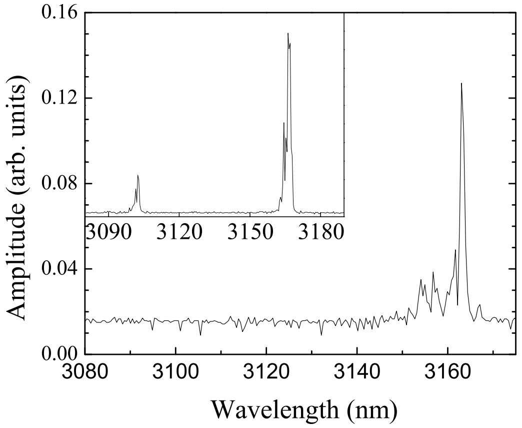

(a)

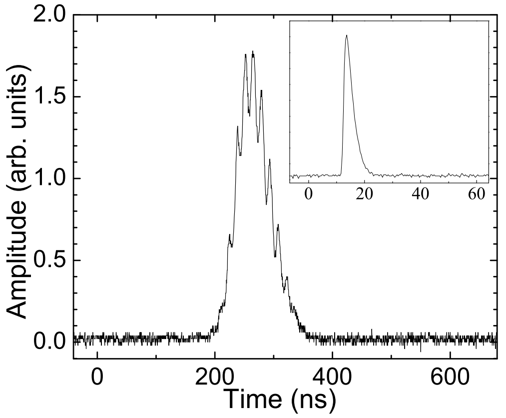

(b)

Figure 5.6: HCN laser pumped with 5-ns pulses at R(9) (a) spectrum (b)temporal profile. The inset shows the corresponding ASE spectrum and temporal profile.

The exact relaxation pathway from the lower laser level to the ground state and relevant time constants are not completely known. There is a possibility for another laser transition between vibrational levels (001) and (010) producing radiation at about 4 μm. There is also another potential laser transition from level (001) to the ground state (000), which would emit at about 3 μm. None of these lasing lines were observed. Likely reasons are insufficient pump energy and inadequate bandwidth of the cavity mirrors.

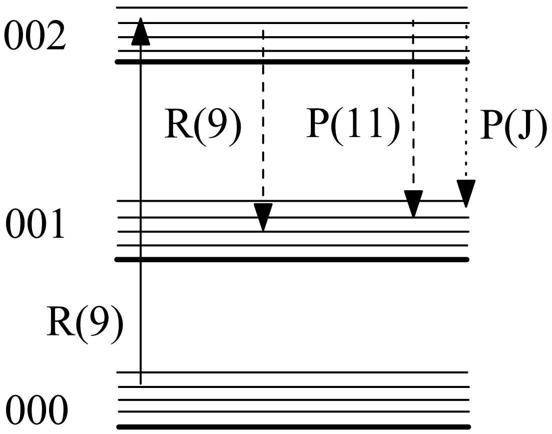

Figure 5.7: The assigned laser transitions of optically pumped HCN where P(J) is the neighboring transition observed from laser output. The R(9) transition was observed from the ASE experiment.

The ASE spectrum shows an additional (weaker) spectral component at about 3.1 μm, which most likely represents the R(9) transition. In the laser, due to gain competition, the weaker line is suppressed. The spectral components in the short-wavelength tail of the laser line can originate from P(9) and P(8) transitions. Similar emission was not observed for C_2H_2. The reason is that the rotational relaxation constant in HCN is about 10 times larger.

5.4 Summary

We demonstrated the first C_2H_2 and HCN lasers that were optically pumped at the communication band. A tunable nanosecond pulsed optical parametric oscillator (OPO) is used to optically pump C_2H_2 and HCN on their absorption lines at 1.5 μm to the combination band states of C_2H_2 and HCN. We have observed laser lines in the 3 μm region that originate from the terminal pump states to combination states of C_2H_2 and HCN. We also have observed mirrorless directed emission from these molecular gases. The results demonstrate the potential of C_2H_2 and HCN as promising gas media for beam combiner systems for communication band.

Chapter 6

Laser model

6.1 Introduction

In this chapter we will introduce a general model of OPMLs that is based on vibration-rotation transitions. Several laser models have been developed based on the assumption of instantaneous rotational thermalization [70, 71]. Comprehensive laser models have been introduced that are able to handle realistic rotational energy transfer [72, 9]. Our laser model is a further development Ref. [9] and enables rotational energy exchange up to Δ J = ± 4, keeps track through 8 vibrational and 30 rotational levels and allows a temperature dependence of molecular constants and takes into account heat dissipation.

In section 3.2, the numerical laser model is explained for a diatomic molecule. Occupation numbers of molecular states are described by rate equations taking into account the interaction with radiation fields and collisions. The temperature change and its effect on relaxation rates and equilibrium level occupations are included. This model can be applied to any polyatomic molecule.

In section 3.3 we will first apply the model to HBr and compare the results to our experimental data. We also adapt this model to C_2H_2 and HCN and compare the simulation results to our experimental observations.

In section 3.4, the performance and spectral tuning of optically pumped HBr lasers are evaluated by the laser model as an example. In this section, the second overtone pulse excitation and the first overtone CW excitation of HBr are studied, which lead us to many conclusions that are of general nature concerning OPMLs.

6.2 Numerical model

Because of the complexity and variety of polyatomic molecules several simplifying assumptions have to be made to maintain a certain degree of generality. A schematic energy diagram is shown in Fig. 6.1.

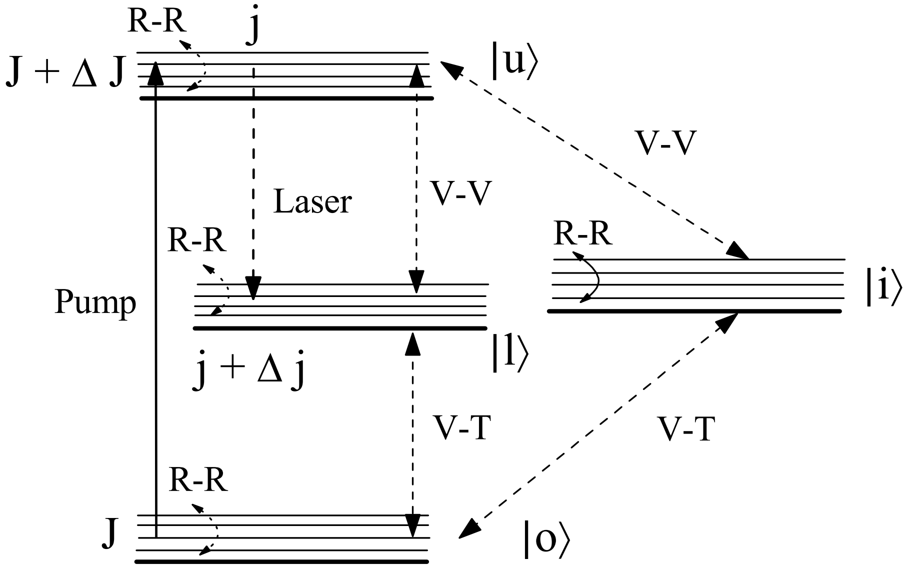

Figure 6.1: A simplified molecular energy level diagram. $|o\rangle$ $|u\rangle$ $|l\rangle$ and $|i\rangle$ denote vibrational states with rotational manifolds.

Molecules are optically pumped from a rotational level (rotational quantum number J) of the vibrational ground state $|o\rangle$ to a rotational level with quantum number $J' = J + \Delta J$ of an excited vibrational level $|u\rangle$. $\Delta J = \pm 1, 0$ for an R, P and Q transition, respectively.

The laser transition occurs between a rotational level (rotational quantum number j) of the vibrational excited state $|u\rangle$ and a rotational level with quantum number $j' = j + \Delta j$ of a vibrational level $|l\rangle$. For the laser transitions, $\Delta j = \pm 1, 0$ for a P, R, Q transition, respectively. The state $|i\rangle$ can represent a single or an ensemble of vibrational states that do not couple to the pump and laser radiation. The molecules can relax back to the vibrational ground state via $|i\rangle$ and from the lower laser state $|l\rangle$ by $(V-V)$ and $(V-T)$ relaxation processes. For diatomic molecules for example, the intermediate state $|i\rangle$ can represent vibrational states of higher energy populated by collisions (vibrational ladder climbing). For each vibrational state, the thermal equilibrium population within the rotational manifolds is produced by rotational relaxation $(R-R)$.

The excited state population that does not contribute to stimulated emission (lasing) can transfer energy to other rotational levels or vibrational levels mediated by collisions. Thus the laser gain will depend not only on the strength of the pump and lasing transitions but also on competing relaxation processes. Therefore the performance of OPMLs is controlled by the interplay between the pump transition, the laser transition and the collision induced population transfer processes.

For diatomic molecules, such as HBr, an intermediate level $|i\rangle$ is not necessary, since the system is simple enough to treat the various relaxation process in detail.

The schematic energy level diagram that will be used for modeling a diatomic molecular laser is shown in Fig. 6.1. Eight vibrational states with quantum numbers $V = 0, 1, 2, \ldots, 7$ are considered to allow for vibrational energy exchange between the terminal pump state, which in our case is at $V = 2$, 3, and vibrational states with higher energy (ladder climbing). For each vibrational state, 30 rotational states are taken into account with quantum numbers $J = 0, 1, \ldots, 29$.

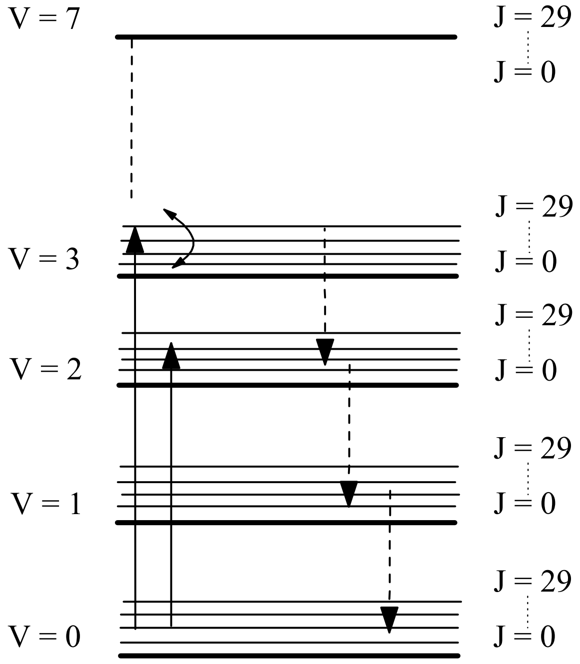

Figure 6.2: Energy level diagram of a diatomic molecule. V = 0, 1, . . . , 7 are the quantum numbers of the vibrational levels and J = 0, . . . , 29 are the rotational quantum numbers. The solid arrows indicate the optical pump transitions exciting a first or a second overtone. The dashed arrows stand for a multitude of possible R or P branch lasing transitions between adjacent vibrational levels.

A schematic diagram of the laser layout that is used in the model is shown in Fig. 6.3. The pump laser is coupled into the cavity through mirror M_1 and retroreflected by mirror M_2 (double pass). Mirror M_1 is the end mirror and mirror M_2 acts as the outcoupler. A uniform (flat top) pump profile in the transverse direction is assumed. In addition, all population numbers are understood as values averaged over the gas cell. The laser output in general is a superposition of laser lines resulting from different R and P branch rotation-vibration transitions.

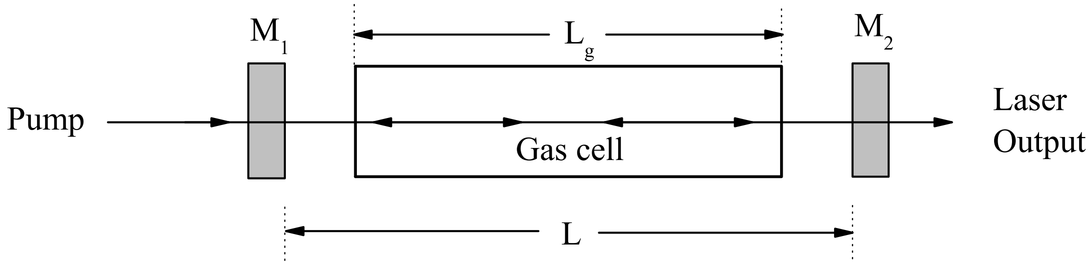

Figure 6.3: Schematic diagram of the optically pumped gas laser on which the model is based.

The rate equations governing the intracavity photon densities (photons/m^3) of these laser lines, $\Phi_P(V,J)$, and $\Phi_R(V,J)$, can be written as

$$\frac{d\Phi_{P,R}(V,J)}{dt} = c\frac{L_g}{L}\,g_{P,R}\,(V,J) - \frac{\Phi_{P,R}(V,J)}{\tau_c} + \Omega\;A_{P,R}\,n(V,J)\frac{L_g}{L}\;, \tag{6.1}$$

where the subscripts $_{P,R}$ denote the P and R branch transitions of a molecule, and the quantum numbers in parenthesis (V,J) denote the upper lasing state. $n(V,J)$ is the population density (molecules/m^3) in the state (V, J). The quantity Ω is a geometrical factor describing the survival rate per round-trip of spontaneously emitted radiation. The passive cavity photon life-time $\tau_c = 2L/c/\left[-\ln(1-R_L) - \ln(R_M)\right]$ is determined by the reflectance R_M of the outcoupler and the combined other linear losses per round-trip, R_L. $A_{P,R}$ is the Einstein coefficient for spontaneous emission. The gain coefficient for a transition starting at molecular state (V, J) is

$$g_{P,R}\,(V,J) = \sigma_{P,R}\,(V,J)\left[n\,(V,J) - \frac{(2J+1)\;n\,(V-1,J\pm1)}{2\,(J\pm1)+1}\right], \tag{6.2}$$

where

$$\sigma_{P,R}(V,J) = \frac{A_{P,R}\,\lambda_{P,R}^2\,S_{P,R}(V,J)}{8\pi}\;, \tag{6.3}$$

is the gain cross section, $\lambda_{P,R}$ is the laser wavelength, and "$-$" ("$+$") stands for the

R (P) transition. $S_{P,R}(V,J)$ is the line shape function (Voigt profile), which was introduced in Eq. (2.51).

At thermal equilibrium at temperature T, the population densities follow a Boltzmann distribution. From Eq. (2.27)

$$n\left(V,J\right)=N_{\mathrm{t}}\frac{\left(2J+1\right)e^{-E(V,J)/k_BT}}{\sum\limits_{V,J}\left(2J+1\right)e^{-E(V,J)/k_BT}}\ , \tag{6.4}$$

where N_{t} is the total number density of molecules, k_B is the Boltzmann constant and $E(V,J)$ is the energy of state (V,J) introduced in Eq. (2.21). In most case only the level with $V=0$ will be occupied at room temperature at thermal equilibrium without the presence of a pump laser. If a pump pulse excites a certain level with $V\neq 0$ a Boltzmann distribution can be established within the rotational manifold of this vibrational state provided that the vibrational depopulation occurs on a slow enough time scale.

The evolution of the population densities is governed by the interaction with the pump and laser fields, and by collisions. The corresponding rate equations can be written as

$$\begin{aligned}\frac{dn\left(V,J\right)}{dt} \quad = \quad & c\,\Phi_R\left(V,J\right)\left[g_R\left(V+1,J+1\right)-g_R\left(V,J\right)\right]\\ & -c\,\Phi_P\left(V,J\right)\left[g_P\left(V,J\right)-g_P\left(V+1,J-1\right)\right]\\ & +R_{\mathrm{pump}}\left(V,J\right)\delta\left(V-V_u,J-J_u\right)\\ & -R_{\mathrm{pump}}\left(V,J\right)\delta\left(V-0,J-J_u-1\right)\\ & +A\left(V,J\right)+B\left(V,J\right)+C\left(V,J\right)+D\left(V,J\right)\ ,\end{aligned} \tag{6.5}$$

where $R_{\mathrm{pump}}(V,J)$ is the pump rate (molecules/s/m^3) averaged over the gas cell and δ is the Kronecker delta function. The terms A,B,C and D describe rates due to various collisionally induced transitions.

The spatially averaged pump rate is approximated by

$$R_{\text{pump}} = \phi_{\text{pump}}\left(V_u\right)\left[1 - e^{-\alpha_{\text{pump}}L_G}\right]\sum_{q=0}^{Q} e^{-q\alpha_{\text{pump}}L_G}\ ,, \tag{6.6}$$

where $\phi_{\text{pump}}(V_u)$ is the incident pump-photon flux density (photons/s/m^3), and Q is the number of cavity roundtrips by the pump. Note that $Q = 1$ refers a double pass through the gain medium. This approach does not take into account that the pump varies longitudinally inside the gain medium, which is consistent with the rate equation approach that uses quantities averaged over one cavity round trip.

The absorption coefficient for the pump radiation is

$$\alpha_{\text{pump}} = \sigma_{\text{pump}}(V_u)\left[\frac{2J_u + 1}{2(J_u \pm 1) + 1}\, n\left(0, J_u \pm 1\right) - n\left(V_u, J_u\right)\right], \tag{6.7}$$

where V_u and J_u are the vibrational and rotational quantum numbers of the upper pump level, respectively.

The pump cross section in Eq. (6.7) is

$$\sigma_{\text{pump}}(V, J) = \frac{A_{\text{pump}}\,\lambda^2_{\text{pump}}\,S_{\text{pump}}(V, J)}{8\pi}\ . \tag{6.8}$$

Here A_{pump} is the Einstein coefficient for spontaneous emission. $S_{\text{pump}}(V, J)$ is the line shape factor and λ_{pump} is the pump laser wavelength. The factor of $(2J_u + 1)/(2(J_u \pm 1) + 1)$ is obtained from the degeneracies of the upper $(J_u\ )$ and lower $(J_u \pm 1\ )$ rotational state of the pump transition. It should be noted that "$-$" ("+") stands for the R (P) transition. We also assume that the spectral width of the pump laser is much smaller than the width of the transition profile.

The terms $A(V, J)$, $B(V, J)$, $C(V, J)$, and $D(V, J)$ represent population changes associated with R-R, V-V, V-T, and isotopic V-V process. The latter process takes into account population transfer between isotopes that may be present. Typically the pump can only excite one isotope because of the narrow pump spectrum. However, the molecular energy states of isotopes can be very close so that resonant energy transfer can have large cross sections. For example for the two isotopes of HBr ($\sim 50\%$ abundance) the difference between alike rotational states is on the order of 0.4 $\mathrm{k_B T}$ at room temperature [35].

The collision induced energy transfer processes depend on the molecule and its collision partner (same molecule or buffer gas). The isotopic V-V process is not present in isotopically pure samples. To briefly discuss processes A through D, a hypothetical diatomic molecule AB is used.

The term $A(V, J)$ in Eq. (6.5) describes the R-R relaxation process. For one particular collision,

$$AB(V,J) + M \leftrightarrow AB(V,J') + M + \Delta E_{R-R} \ . \tag{6.9}$$

In this case, M could be another AB molecule or a buffer gas molecule and $\Delta E_{R-R} = E(V,J) - E(V,J')$ is the energy mismatch of the participating rotational states assuming that the energy state of M does not change. The term $A(V,J)$ can be written as

$$A\left(V,J\right) = \sum_{M} \sum_{J' \neq J} \left[k'_M\left(V, J \leftarrow J'\right) - k_M\left(V, J' \leftarrow J\right) n\left(V,J\right)\right] n_M \ , \tag{6.10}$$

where $k_M(V, J' \leftarrow J)$ is the rate constant ($\mathrm{m^3 molecule^{-1} s^{-1}}$) for population transfer from level J' to J and n_M is the total number density of collision partner M.

The forward and backward rate constants $k'_M(V, J \leftarrow J')$ and $k_M(V, J' \leftarrow J)$ are related to each other by

$$k'_M(V, J \leftarrow J') = k_M\left(V, J' \leftarrow J\right) \frac{2J+1}{2J'+1} e^{-\Delta E_{R-R}/k_B T} \ , \tag{6.11}$$

where $J' > J$.

The term $B(V, J)$ in Eq. (6.5) describes the V-V relaxation process. Since the V-V energy transfer probability falls off rapidly for increasing energy mismatch [23] , we consider only the collisions of AB molecules that are initially in the same vibrational state

$$AB(V, J) + AB(V, J) \leftrightarrow AB(V + 1, J) + AB(V - 1, J) + \Delta E_{V-V} \ . \tag{6.12}$$

which is the process producing the smallest energy mismatch.

The energy defect is,

$$\Delta E_{V-V} \ = \ E(V, J) + E(V, J) - E(V + 1, J) - E(V - 1, J) \ . \tag{6.13}$$

The term $B(V, J)$ can be written as

$$B(V, J) = k'_V n(V + 1, J)n(V - 1, J) - k_V n(V, J)n(V, J) \ , \tag{6.14}$$

where k_V and k'_V are rate constants ($\mathrm{m}^3\,\mathrm{molecule}^{-1}\,\mathrm{s}^{-1}$) for the forward (exothermic) and backward direction, respectively, and $k'_V = k_V e^{-\Delta E_{V-V}/k_B T}$.

The terms $C(V, J)$ in Eq. (6.5) describe the V-T energy transfer process. Since the transition from V to $V - 1$ has by far the largest cross section, we have included only the following process in the model:

$$AB(V, J) + M \leftrightarrow AB(V - 1, J) + M + \Delta E_{V-T} \ , \tag{6.15}$$

where $\Delta E_{V-T} = E(V, J) - E(V - 1, J)$ is the energy supplied or absorbed by the translational degrees of freedom. The term $C(V, J)$ can be written as

$$C\,(V, J) = \sum_M \left[\kappa'_M n\,(V - 1, J) - \kappa_M n\,(V, J)\right] n_M \ , \tag{6.16}$$

where κ_M, κ'_M are the rate constants (m^3 molecule^{-1} s^{-1}) for the forward (exothermic) and backward direction, respectively, and

$$\kappa'_M = \kappa_M e^{-\Delta E_{V-T}/k_B T} \ . \tag{6.17}$$

For simplicity, the term $D(V, J)$ in Eq. (6.5) considers only vibrational energy exchange of two isotopic molecules A$^{\mathrm{a}}$B and A$^{\mathrm{b}}$B in collisions,

$$A^a B(V, J) + A^b B(V', J) \leftrightarrow A^a Br(V-1, J) + A^b B(V+1, J) + \Delta E_{\mathrm{iso}} \ . \tag{6.18}$$

The corresponding term $D(V, J)$ can be expressed as:

$$D(V, J) \ = \ \sum_{V'} k'_{iso}\, n^a(V-1, J) n^b(V'+1, J) \sum_{V'} -k_{iso}, n^a(V, J) n^b(V', J) \ , \tag{6.19}$$

where

$$\Delta E_{\mathrm{iso}} \ = \ E^a(V, J) + E^b(V', J) - E^a(V-1, J) - E^b(V'+1, J) \ . \tag{6.20}$$

The rate constants (m^3 molecule^{-1} s^{-1}), k_{iso} and k'_{iso} represent the forward (exothermic) and backward direction and

$$k'_{iso} = k_{iso} e^{-\Delta_{\mathrm{iso}}/k_B T} \ . \tag{6.21}$$

The gas temperature changes during the pump and laser process. Assuming a constant volume (gas cell) the pressure will also change. Both temperature and pressure thus modify linewidths and relaxation rates during the laser process. Through the temperature the equilibrium (rotational) population numbers are also expected to change. All these effects are taken into account phenomenologically in our model.

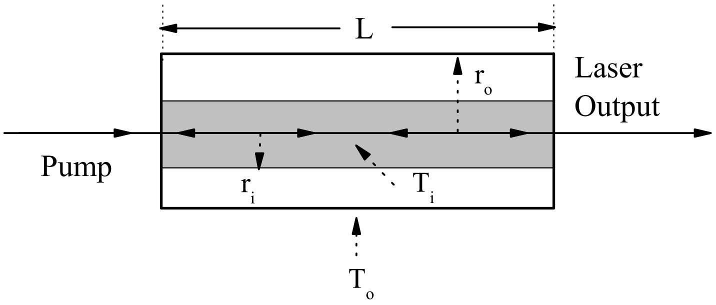

Figure 6.4: The layout of the pump cylinder that the temperature dependent model was based on.

We consider that the pump excites a cylinder of radius r_i uniformly as shown in Fig. 6.4.

To discuss the principal effect of temperature and heat conduction on the laser output in a semi-quantitative way we made some simplifying assumptions. In general the rate equation of the temperature change can be written by,

$$\begin{aligned} \frac{dT_i}{dt} &= \frac{1}{\rho C}\frac{dQ}{dt} \\ &= \frac{1}{\rho C}\left[\frac{P_{\text{abs}} - P_{\text{out}}}{V_p} - \frac{dE_{viro}}{dt} - \frac{dE_{con}}{dt}\right] , \end{aligned} \tag{6.22}$$

where V_p is the pump volume, C is the heat conduction, ρ is the gas density. The net heat energy deposition per unit time, dQ/dt, is calculated from the absorbed pump power P_{abs} minus the power emitted by the lasing process and by spontaneous emission, P_{out}. Thermal energy can be transported to the cylinder wall denoted as dE_{con}/dt. The rate of change of the vibration-rotation energy density in the pump volume dE_{viro}/dt is also taken into account [23] where

$$\frac{dE_{viro}}{dt} = \sum_{V,J} E(V,J)\frac{dn(V,J)}{dt} \ . \tag{6.23}$$

In steady state the pump and laser produce a gas cylinder of radius r_i that has a constant temperature T_i within the cylinder of radius r_0. The cylinder wall is kept at constant temperature T_0, which leads to a linear temperature gradient with respect to the radius coordinate from r_0 to r_i.

Under steady state conditions thus $dE_{viro}/dt = 0$ and we used the solution of the heat conduction equation through a cylindrical surface which is given by [73]

$$\frac{dE_{con}}{dt} = \frac{2\kappa(T_i - T_0)}{r_i^2 \ln(r_0/r_i)} \ , \tag{6.24}$$

where κ is the thermal conductivity.

The rate equation for the temperature T_i reads

$$\frac{dT_i}{dt} = \frac{1}{\rho C}\left[\frac{P_{\text{abs}} - P_{\text{out}}}{\pi r_i^2 L_{WG}} - \frac{2\kappa\,(T_i - T_0)}{r_i^2\,\ln(r_0/r_i)}\right] \ , \tag{6.25}$$

This equation is solved simultaneously with the rate equations introduced previously in each time step and the molecular rates are changed if necessary for the next time step.

6.3 Model predictions and comparison to experimental results

In this section, we will compare our numerical results of HBr, HCN and C_2H_2lasers and experimental results discussed in chapter 4 and chapter 5. The main purpose was to verify the observed lasing lines.

6.3.1 Second overtone pumped HBr laser

The characteristics of the HBr laser output was discussed in section 4.3. We have observed a total of 5 lasing lines, namely, P(6), P(5), P(4) for the transitions $V(3 \rightarrow 2)$ and P(4), P(5) for the transitions $V(2 \rightarrow 1)$.

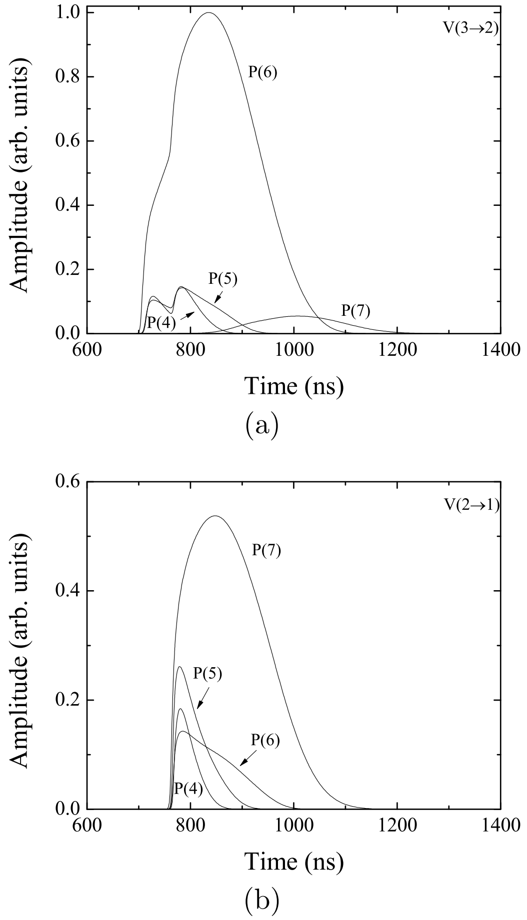

Figure 6.5: HBr laser pumped at R(4) (a) Lasing transitions from $V(3 \rightarrow 2)$ (b) Lasing transitions from $V(3 \rightarrow 2)$. The peak of the 200 ns pump pulse is at 800 ns

To simulate the HBr laser, we used the laser parameters from our experiment. The energy input was 60 mJ (pulse duration = 200 ns), double pass pump (that is Q=1 in Eq.(6.6)) with the spot size (radius) of 1.75 mm. The gas pressure of HBr was 25 torr yielding an absorbed energy of about 8.7 mJ. The laser cavity length was 1.4 m and the HBr cell was 1 m. The reflectivity of the outcoulping mirror was 0.75. Figure 6.5 shows the simulated temporal profiles of the lasing transitions using laser parameter close to the experiment. Figure 6.5 shows some additional lines compared to what we observed in our experiment. The line P(7) is the weakest line from the transition $V(3 \rightarrow 2)$ and this line could be at the noise level of the recorded spectrum in Fig.4.8. According to the parameters shown in Table. 3.2, the wavelength of this transition is 4428.22 nm. Since our model did not include the CO_2 absorption, the simulation produced P(6) and P(7) lines from the transition $V(3 \rightarrow 2)$. In the experiment the CO_2 absorption is strong enough to completely suppress these laser lines. To include the CO_2 absorption in our model, the exact CO_2 line positions with respect to the HBr lasing transitions are required.

Laser transitions from V=2 can occur only after transitions from V=3 have established large enough populations in rotational states n(V=2,J). Therefore the onset of these laser lines in delayed relative to transition $V(3 \rightarrow 2)$.

6.3.2 3 μm lasing of C_2H_2 and HCN lasers

The C_2H_2 and HCN laser outputs were shown in section 5.3. Based on the laser parameters given in section 5.3.1, we simulated the laser outputs of C_2H_2 and HCN. It should be noted that the pump diameters are about twice larger than the laser mode diameters both of C_2H_2 and HCN lasers. Therefore the absorbed pump energies in the laser mode volumes are about 1/4 of the total absorbed pumped energies. The simulation results are shown in Fig. 6.6 and Fig. 6.7. The peak of the pump pulses in both cases is at 20 ns.

The obtained C_2H_2 laser lines are identical to those observed in the experiment (cf.Fig.5.4 and Fig.5.5). The simulated temporal profile persisted over a longer time

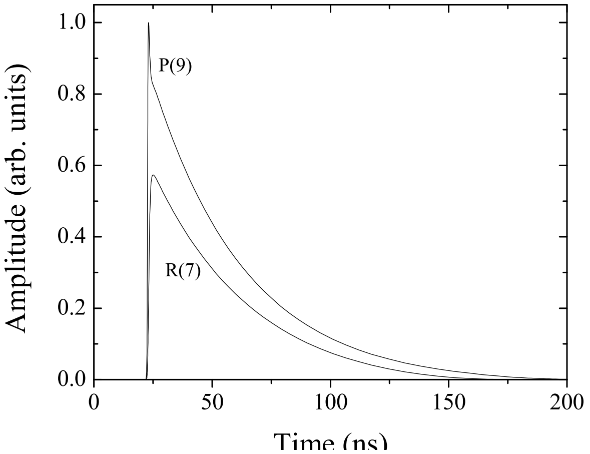

Figure 6.6: C_2H_2 laser pumped at R(7). The laser lines arise from the transition between (10100) and (10000).

period owing to a laser cavity with mirrors having a reflectivity of 0.9 which agrees what we observed in the experiment (see.Fig.5.4).

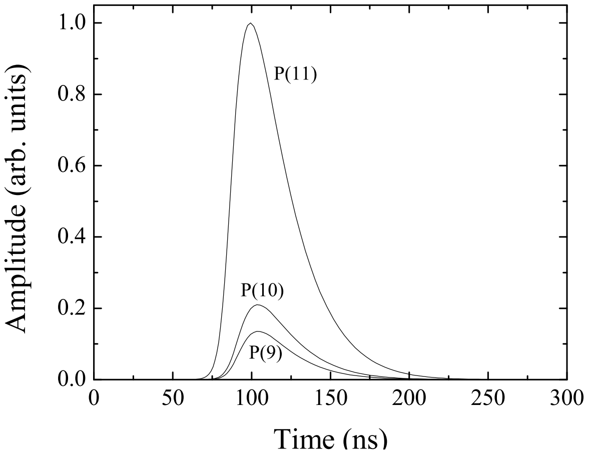

Figure 6.7: HCN laser pumped at R(9). The laser lines occur from the transition between (002) and (001).

The HCN laser lines from our simulation (Fig. 6.7)are in qualitative agreement with the observed laser output shown in Fig.5.6 and assigned in Fig. 5.7. The strongest laser line is P(11) and the structures in the short wavelength tail of the main peak correspond to P(10) and P(9). These structures are possible due to the fast rotational relaxation (about 5 ns), which is of the same time scale as the pump pulse duration (5 ns). The simulated temporal profile of the HCN laser output also agree with the observed temporal profile (see Fig.5.6). It should be noted that the rise time is slow compared to that of C_2H_2. This is due to the short length of the gas cell, which requires more cavity roundtrips for the pulse to reach the peak.

6.4 Performance and spectral tuning of optically pumped overtone HBr lasers

In this section, we will discuss the HBr laser performance and its spectral tuning ability when pumped with a pulse and CW. For the former we consider a second overtone pump as was realized in the experiments described in section 4.3. For the latter we will assume a CW pump in resonance with the $V = 2$ vibrational state (first overtone).

For the case of second overtone pumping a short pump pulse (100 ns) is considered. A quadruple pass of the pump is assumed (that is Q=3 in Eq.(6.6)). For the first overtone pumping a quasi CW source is assumed and a double pass through the gain medium ($Q = 1$). A shown in the experimental section, second overtone pumping is possible with a pulsed Nd:YAG laser tuned to 1.339 μm . The first overtone transition of HBr at 1.962 μm can be accessed with a CW Tm-doped fiber laser or a pulsed optical parametric amplifier. As mentioned previously, we assume that the pump linewidths are much smaller than the absorption linewidth of HBr; the latter is typically hundreds of MHz (cf. Table 3.1).

The laser efficiency η presented in the result is defined as the laser output energy divided by the absorbed pump energy. This efficiency relates better to the intrinsic efficiency of the system; it is not affected by the number of pump passes through the gain medium or the length of the gain medium.

For both laser scenarios, we will discuss the pressure and temperature dependence of the laser performance. As mentioned previously, the lasing transitions of HBr are in the 4 μm region and they can be used for atmospheric applications.

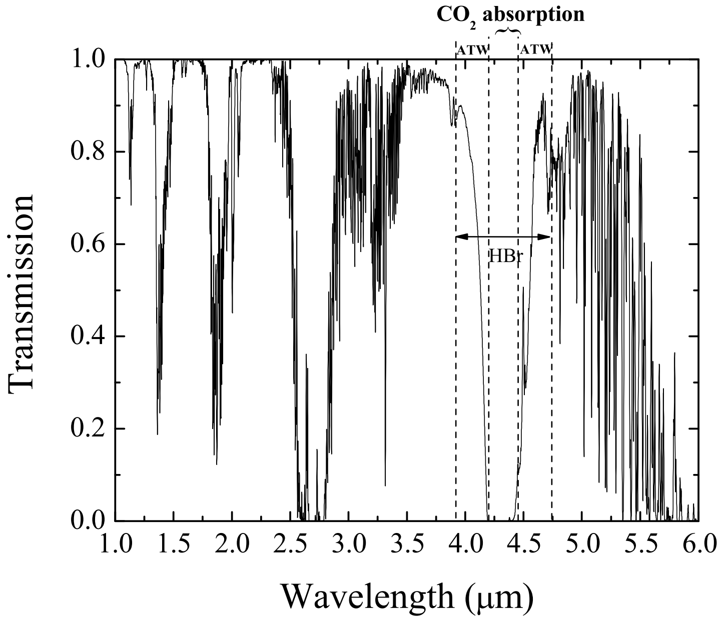

Figure 6.8: Atmospheric transmission in spectral range from 1 μm to 6 μm obtained from IRTRANS4[74]. The spectral region covered by a second overtone and a first overtone pumped HBr laser are shown as an example

As shown in Fig. 6.8, some of laser transitions of HBr fall into the high absorption region of CO_2. It is therefore desirable to be able avoid these laser transitions and shift the energy to transitions in the high transmission region. We will discuss the possibility of spectral tuning of the laser output by inserting suitable filters into the cavity. We will also consider a waveguide laser that can realize long interaction lengths. At the end of the section we will evaluate the ultimate limits of the achievable laser efficiency.

6.4.1 Second-overtone transition excited by a pulsed pump

The simulations with a short pump pulse (100 ns) refer to the laser cavity shown in Fig. 6.3. Reflectances of mirrors M_1 and M_2 for the laser radiation are 100% and 75%, respectively, unless mentioned otherwise. The pump beam has a uniform beam diameter of 3 mm, the length of the gas cell is $L_g = 1.0\,\mathrm{m}$ and the total cavity length $L = 1.3\,\mathrm{m}$.

The collision time of HBr at typical laser gas pressures about 20 torr is on the order of 1 ns and thus much shorter than the pump pulse duration of 100 ns. We therefore assume that the temperature increase of the pumped gas region is instantaneous. At room temperature, the thermal velocity of an HBr molecule is about 300 m/s. Neglecting collisions, it would take the molecule about 10 μs to traverse a distance corresponding to the pump beam diameter. Since this time scale is so much longer than the lasing event we can safely neglect heat dissipation (conduction) out of the active region for pulsed excitation.

For a general overview of the laser performance, we simulated the onset of the various laser transitions and the laser efficiency as a function of pump input energy and plotted the results in Fig. 6.9.

It is the evident that immediately after the laser threshold is reached transitions between V = 3 and V = 2 as well as between V = 2 and V = 1 occurred. In general, P-branch transitions have lower lasing thresholds than R-branch transitions owing to a more favorable degeneracy factors as seen in Eq. (6.2).

The last step of the lasing cascade (transitions V(1→0)) is achieved only at large pump energies (fluences exceeding 14 J/cm^2). A complete lasing cascade is desirable

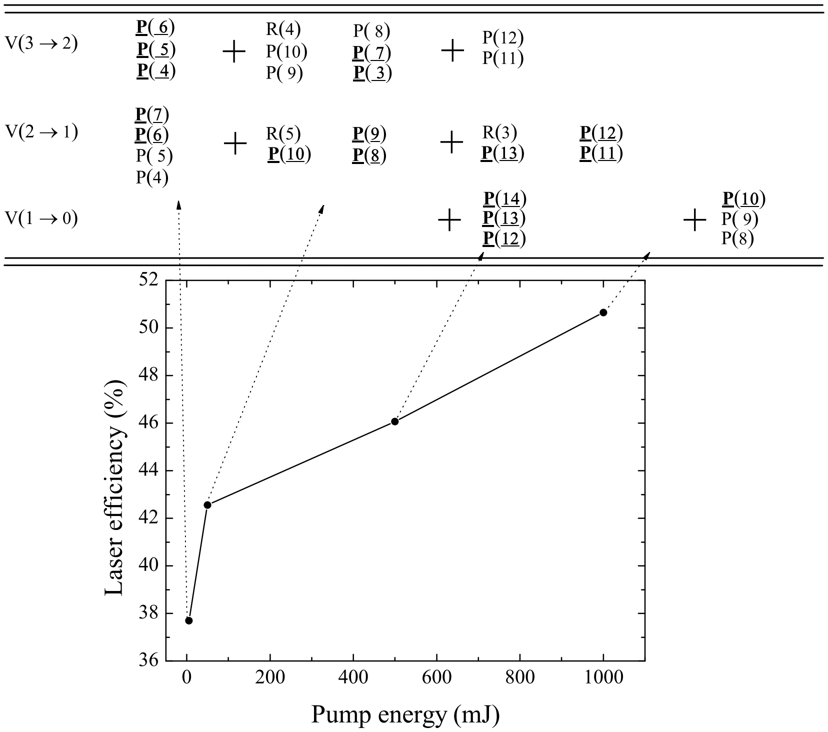

Figure 6.9: Laser efficiency and compilation of lasing transitions for four different pump energies. The underlined laser transitions indicate emission outside the atmospheric transmission window.

for large efficiencies. Achieving a population inversion between V = 1 and V = 0 requires a sufficient depletion of the ground state. This is easier to achieve for pump pulse durations that are longer than the R-R relaxation time, which allows for a larger number of molecules to be excited from a certain rotational level of the vibrational ground state.

After the transitions from V = 1 to V = 0 turn on, the laser efficiency increases rapidly. For high input energies (∼ 10 J) the laser efficiency is expected to be about 69%. This is where the pump transition begins to saturate. Beyond this point (not shown in Fig. 6.9), the laser efficiency increases slowly and the maximum achievable laser efficiency is expected to approach 80%.

6.4.1.1 Pressure and temperature dependence

Pressure and temperature of the gas can be controlled relatively easily in the experiment. Their effect on the laser performance will be discussed next to predict optimum operation conditions.

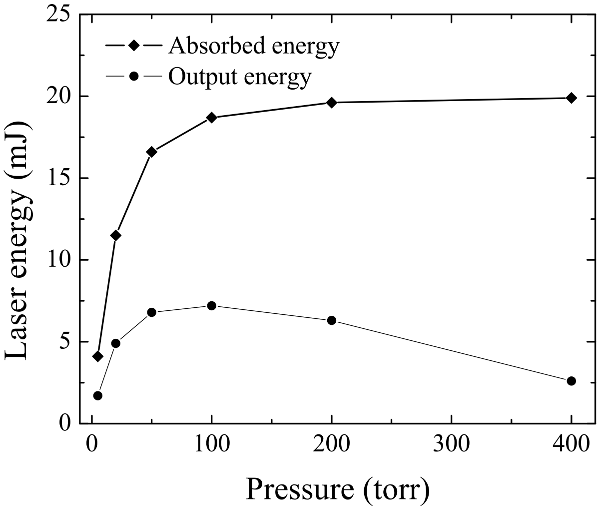

Figure 6.10: Absorbed energy and output energy as a function of pressure, $T = 298\,\mathrm{K}$ for the second overtone, pulse-pumped laser.

Figure 6.10 shows the laser energy as a function of HBr pressure p without the presence of buffer gas. Changing the pressure of the active gas impacts the laser performance through (i) the number density of absorbing molecules, (ii) the collisional line broadening factor and consequently the absorption and emission cross sections, and (iii) the collision rates that control rotation and vibrational relaxation times. At high pressures of HBr, the absorbed energy levels off due to pressure broadening (cf., section 2.4). The laser output energy decreases at higher pressure as more absorbed energy dissipates radiationless due to the increase of V-V and V-T energy transfer rates.

While experimentally somewhat more challenging to change, the temperature is

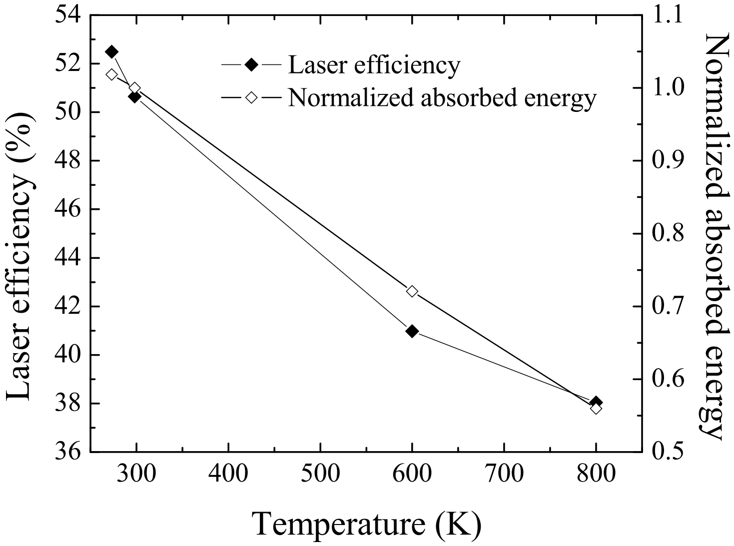

Figure 6.11: Laser efficiency and absorbed pump energy normalized to its value at $T = 298\,\mathrm{K}$ as a function of initial gas temperature. The pump energy was 1 J.

another parameter that will affect the laser performance. Figure 6.11 shows the expected efficiency of the laser for initial gas temperatures from 273 K to 800 K, assuming a constant ratio p/k_BT ($p = 20\,\mathrm{torr}$ at 298 K). This constant ratio ensured a constant molecular number density.

Due to more favorable Boltzmann population at low temperatures, pump absorption increases as the gas temperature decreases. This results in an increase of the laser efficiency with decreasing temperature. The relative population of the lower pump level to the total number density increases from 12% at 800 K to 16% at 273 K. Another factor which contributes to the enhanced efficiency at lower temperature is the smaller line width of the laser transitions at lower temperatures increasing the absorbed pump energy and stimulated emission cross section. The temperature dependence of the R-R rate had only a minor effect on the laser output (results not shown) in this pressure range. The corresponding R-R thermalization time at temperature of 800 K is only 1.7 times faster than at a temperature of 273 K.

6.4.1.2 Manipulating the laser spectrum with intracavity spectral filters

As indicated in Figs. 6.9 and Fig. 6.8 an optically pumped molecular laser can potentially oscillate on tens of vibration-rotation transitions, and in the case of HBr, covering a spectrum from 3.95 μm to 4.63 μm. Following the excitation of a particular rotational state is a fast rotational energy transfer out of this state to establish a Boltzmann distribution if lasing and vibrational relaxation are neglected. This fast energy transfer between rotational states provides attractive possibilities to tune the spectral output of the laser without substantially sacrificing the laser efficiency.

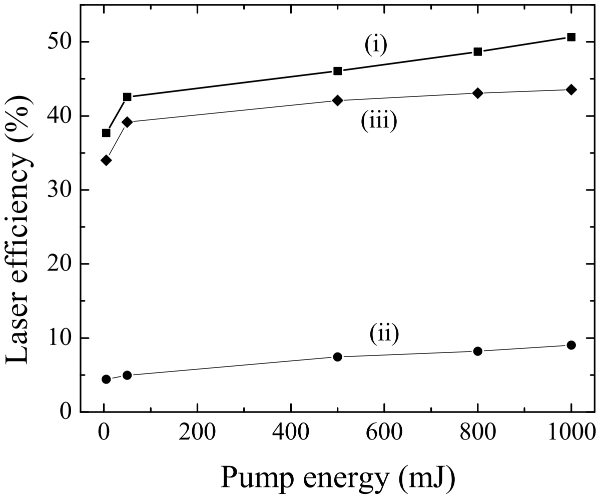

Figure 6.12: Laser efficiency as a function of the pump energy for (i) total output with no intracavity filter, (ii) the output in the atmospheric transmission window (ATW) with no intracavity filter, and (iii) the output in the ATW with an intracavity filter that blocks the laser lines outside the ATW.

A particular practical application to force the laser emission into the atmospheric transmission window (ATW) is proposed. Some of the possible laser transitions (underlined in Fig. 6.9) fall outside the atmospheric transmission. A suitable spectral filter that increases the cavity losses in the area of high atmospheric absorption (4.2 μm to 4.45 μm) was incorporated in the rate equation model and prevented lasing in this spectral region.

Figure 6.12 depicts the laser efficiency of emission into the transmission window with and without filter as a function of pump input energy. The results indicate the possibility to tailor the spectral output of the laser without substantially sacrificing the laser efficiency. This is possible because of the fast rotational relaxation during the pump event that replenishes the population of rotational levels from which lasing occurs from rotational states that cannot depopulate through lasing because of the filters.

6.4.2 First-overtone transition excited by a Quasi-CW pump

6.4.2.1 Temperature and heat dissipation effects

To achieve CW lasing under conditions when the cascade is not complete is difficult and will generally result in low efficiency. In such a case, to maintain lasing, the lowest vibrational level has to be depopulated by vibrational relaxation which is rather slow. Addition of a buffer gas to facilitate relaxation to the ground state can help to reduce this bottleneck. For simulating CW excitation, we used a step function pump profile and the simulations were carried out until steady state was reached. The steady-state laser parameters then represent CW laser output parameters.

In a high power CW laser heat generation and dissipation are issues. Unlike in solid state lasers thermal effects in gas lasers can be mitigated by circulating the gain media (gas flow). In addition, or as an alternative option, heat dissipation through the walls of the laser tube can be utilized. This requires sufficiently small transverse dimensions of the tube and possibly the addition of a buffer gas of significant thermal conductivity. Waveguide (WG) like structures[1] seem to be ideal candidates for

---

[1] The waveguide can be made of, for example, a silica tube (capillary) coated internally with Ag and AgI or coated with dielectric multi-layers using an Omniguide design for

realizing long interaction lengths between a laterally confined pump beam and the active gas while permitting efficient heat transfer to the walls of the tube.

For such a cavity we investigated the thermal effects on the performance of a CW pumped laser. In general, a temperature increase will affect the line broadening of the transitions, accelerate vibrational and rotational relaxation and shift the maximum of the thermal equilibrium (Boltzmann) distribution to higher energy states. Whether the process is constant volume (sealed tube) or constant pressure (open tube with gas flow) will further influence the behavior of some of these parameters. In what follows we will refer to the case of a sealed tube.

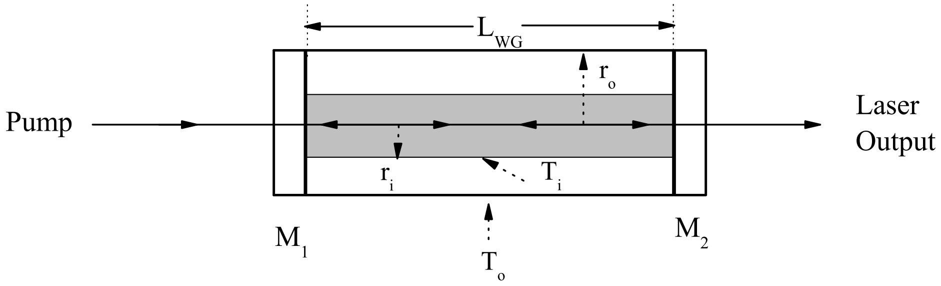

Figure 6.13: Schematic diagram of an optically pumped gas laser using a waveguide cavity. The reflectance of mirror M_1 for the laser is 100% with maximum transmission for the pump. The end face of the waveguide (M_2) acts as outcoupling mirror with a reflectance of 65% and has maximum reflectance (100 %) for the pump.

The simulations refer to the geometry shown in Fig. 6.13. The WG end faces can act as mirrors providing optical feedback for the pump and the laser radiation. We assume here a 1.5-m long WG with 13% round trip loss with a core diameter of 1 mm.

The heat conductivity κ and the heat capacity C of buffer gases and HBr gas are listed in table 3.16. If the gas consists of a mixture of an active gas (HBr, index a) and buffer gas (index b) with partial pressure p_a and p_b the resulting heat conductivity

---

extremely large bandwidth [75].

κ and the heat capacity C can be calculated by using Eqs. (3.19) and (3.20).

The laser performance (efficiency) and the temperature behavior were modeled as a function of the heat conductivity under conditions that resulted in a complete lasing cascade from V = 2 to V = 0. We assumed a pump power P = 230 W, $p_a = 2.5\,\mathrm{torr}$, $p_b = 37.5\,\mathrm{torr}$, $r_0 = 0.5\,\mathrm{mm}$ and $r_i = 0.225\,\mathrm{mm}$.

The temperature dependencies of R-R, V-V, V-T and isotopic V-V rates discussed in section 3.5 were incorporated in our simulations.

Figure 6.14 and Fig. 6.15 show the laser efficiency as a function of the heat conductivity. To discuss the role of radiationless depopulation of vibrational states we simulated in Fig. 6.14 the laser performance for a sequence of increasing V-T deactivation rates, starting from the actual rate for HBr, while the realistic rates for R-R, V-V and isotopic V-V processes were used. The initial gas temperature was 273 K in all cases. The operational steady-state temperature in the lasing volume, T_i, is shown for the smallest and largest value of the thermal conductivity on the corresponding graphs.

From Fig. 6.14 it is evident that for a given V-T relaxation rate only small thermal conductivities have a substantial impact on the laser efficiencies. Only for small thermal conductivities is the change in operational temperature large enough that temperature induced changes in the V-T relaxation rates reduce the laser efficiency. This trend becomes more pronounced for V-T relaxation rates that are larger than the actual rates. Note that the V-T relaxation scales with the temperature approximately as $\sqrt{T}$ [23]. The V-T relaxation provides nonradiative depopulation pathways that are in competition with the laser process. An increase in thermal conductivity, for example by adding buffer gas, reduces the temperature and the impact of nonradiative relaxation.

The efficiency presented refers to the laser power transmitted through the out-

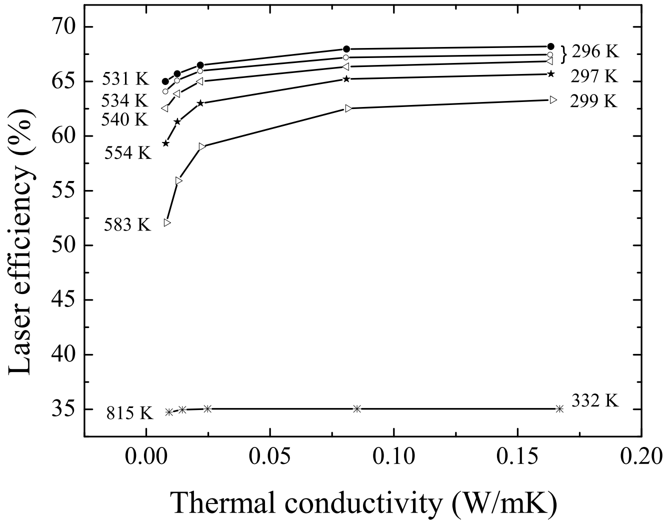

Figure 6.14: Laser efficiency as a function of the thermal conductivity of the gas in the waveguide for a first overtone CW pumped laser for various V-T relaxation rates for the transitions from V = 2 to V = 0 and from V = 1 to V = 0, $\bullet$ - actual V-T rates, $\circ$ - 2 × actual V-T rates, $\triangleleft$ - 4 × actual V-T rates, $\star$ - 8 × actual V-T rates, $\triangleright$ - 16 × actual V-T rates, and $*$ - $10^3\times$ actual V-T rates, see section 3.5 for V-T rate constants.

coupling mirror. If we lump the WG losses into the outcoupling mirror all quoted efficiencies must be multiplied by a factor of 1.37. This suggests that the theoretically achievable efficiency is as high as ∼92% using the actual HBr vibrational relaxation rates and the highest thermal conductivity. This maximum possible efficiency reduces to a value close to the quantum efficiency of ∼48% in the case where lasing occurs only on the V = 2 to V = 1 transitions. This is the case shown in the bottom curve of Fig. 6.14, where the V = 1 state is depopulated by fast (artificially increased) V-T relaxation.

Figure 6.15 shows the laser efficiency as a function of the thermal conductivity for different initial gas temperatures for constant pump power (230 W) and for constant absorbed pump power using the actual V-T rates. For the constant pump case increasing temperature is associated with diminishing absorbed power owing to ab-

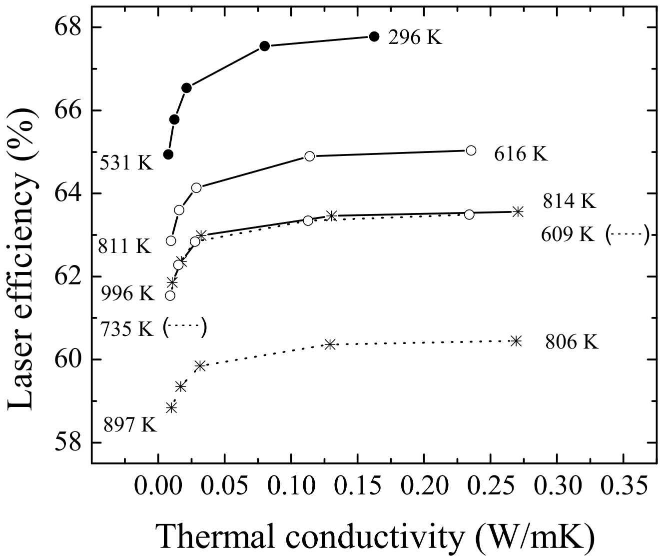

Figure 6.15: Laser efficiency as a function of the thermal conductivity for three different initial gas temperatures (●- 273 K, ○- 600 K, ∗- 800 K). The dotted lines represent the case of a constant incident pump power, the solid curves were obtained for a constant absorbed pump power equal to the pump power for an initial gas temperature of 273 K. The steady-state temperatures for the smallest and the largest heat conductivities are also shown. The pump power was 230 W.

sorption line broadening (Doppler and pressure broadening), which consequently decreases the absorption rate. Therefore, it is apparent that the efficiency for constant absorbed pump power exceeds the corresponding efficiencies for constant incident pump power. For constant absorbed pump power the efficiency also decreases with increasing temperature as a result of increasing V-T rates.

6.4.2.2 Spectral tuning

We also modeled the CW pumped laser with an intracavity spectral filter. To estimate the efficiency of R-R relaxation in channeling energy into desired rotational levels we restricted lasing to arbitrarily selected individual lines out of V = 2 while admitting all transitions from V = 1.

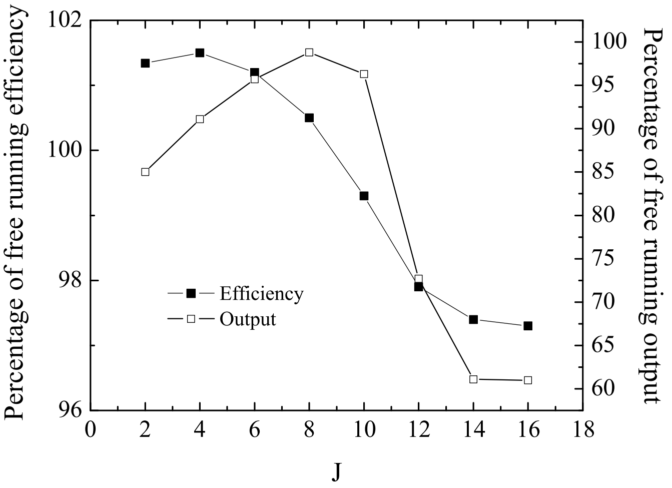

Figure 6.16: Laser efficiency obtained with an intracavity filter normalized to the free-running laser as a function of the single rotational state (J level) at V = 2 that was allowed to laser. All transitions from V = 1 to V = 0 were permitted.

The laser output was simulated as a function of the rotational quantum number J of the upper laser level (V = 2). The results are shown in Fig. 6.16.

It is apparent that the laser efficiency is generally similar to that of the entirely free running laser case. The small variation around 100% is due to the change in mean photon energy of emission relative to that of the laser without constraints. The output power can reach more than 98% of that of the free running laser for transitions starting at J = 8 in V = 2. This is remarkable considering that the pump populates the level J = 5. This demonstrates the efficiency of the R-R energy transfer mediated in part by the He buffer gas and aided by the vibrational level life-time of $\sim$500 μs of HBr for the specified gas mix.

Another approach is to limit the laser bandwidth around a desired center wavelength. This would mean only a certain group of transitions are allowed. Corresponding results are shown in Fig. 6.17. The filter bandwidth was adjusted between 2 nm and 15 nm so that exactly one transition from V = 2 and one transition from V = 1 occurs.

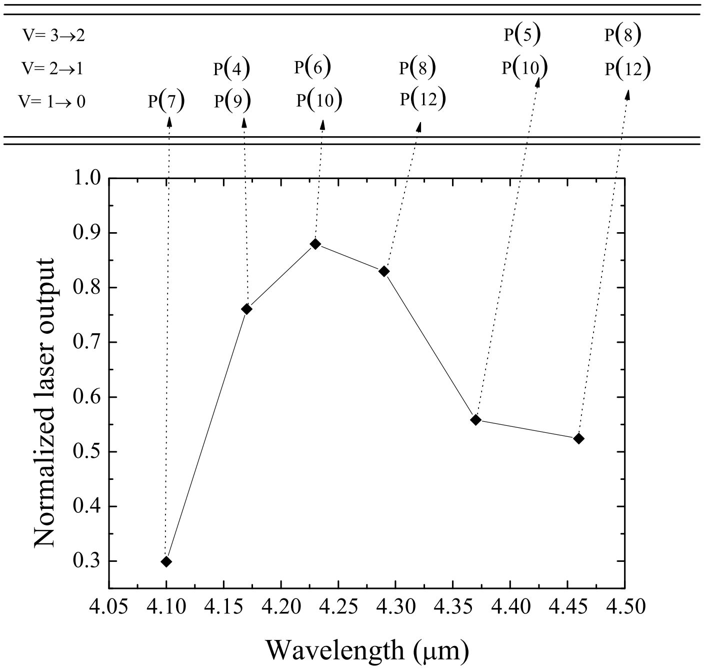

Figure 6.17: Laser output normalized to the free-runing case as a function of the filter pass wavelength. One lasing transition within the filter bandwidth was allowed from each vibrational level.

The efficiency and laser output is maximum where lasing out of V = 2 is allowed from the upper pump level (J = 5) producing the P(6) line. There are also cases where weak lasing out of V = 3 can be expected as a result of population transfer via V-V processes (ladder climbing).

6.5 Summary

A comprehensive laser model was been developed to predict the performance of optically pumped molecular lasers under pulsed and continuous wave excitation conditions. The model dynamically keeps track of the population of 8 vibrational states and 30 rotational states. Collision induced relaxation among rotational levels, vibrational levels, energy transfer to translational degrees of freedom, and interactions with buffer gas, and the temperature dependence of these processes are included. General features of CW and pulse pumped higher overtone molecular gas lasers are discussed using parameters of HBr gas as an example. For a second overtone pulse pumped HBr laser, a complete lasing cascade can be expected at a certain pump pulse fluence resulting in maximum achievable efficiencies approaching 80%. Frequency tuning and spectral narrowing of the laser output is possible with the insertion of intracavity filters without sacrificing laser output power owing to efficient energy redistribution between rotational levels mediated by appropriate buffer gases. CW lasing using waveguide (WG) like geometries is possible with efficiencies approaching 92% for first overtone pumped lasers. Heat conduction through the active gas enhanced by buffer gases and subsequent heat dissipation through the cooled WG walls are expected to handle the thermal load up to kW output power levels.

The laser model was used to compare the experimental results in HBr, HCN and C_2H_2 lasers. The simulation results show good agreement with the experiments. The general conclusions drawn from the model could be applied to other similar overtone optically pumped molecular gas lasers.

Chapter 7

Optically pumped molecular lasers with small quantum defect

7.1 Introduction

In the preceding chapter, a comprehensive laser model was introduced to predict the performance and spectral tuning ability of an OPML system. A first and second overtone pumped HBr laser was studied with this model. It should be mentioned that it is also possible to pump a fundamental transition and to obtain lasing on a transition back to the ground state from the excited rotational level or from a different rotational level resulting small energy defect between the lasing transition and the pump transition. Such a laser would be similar to atomic vapor lasers in terms of very high quantum efficiency and large slope efficiency as discussed in chapter 1.

For a small quantum-defect optically pumped laser (SDOPML),lasing has to occur between the pumped vibrational level and the vibrational ground state. Such molecular lasers would have a number of attractive features. They can be operated at room temperature, and a certain amount of frequency tunability exists owing to the multitude of possible vibration-rotation transitions.

The first SDOPML was demonstrated by Skribanowitz et al in 1972 by using hydrogen fluoride (HF) as the gas medium [76]. This concept was first analyzed by Golger and Letokhov in 1973 [70]. From 1970s to 1990s, several optically pumped ammonia (NH_3) lasers have been demonstrated. Up to date, the small defect optically pumped (NH_3) laser is still the most powerful optically pumped gas laser that has ever been reported [77].

In this chapter, we analyze theoretically the potential of a continuous wave (CW) molecular laser operating on vibration-rotation transitions with small quantum defect. In order to make this approach applicable to a broader class of molecules including polyatomic molecules we include an intermediate state, cf. Fig. 7.1.

The fact that pump and lasing transitions involve only two vibrational states allows us to approach the laser problem analytically if we make some simplifying assumptions. We will first develop the theoretical background for a general molecule (section 7.2) and then apply the results to HCN (section 7.4). We will also test the validity range of the analytical equations with our computer model (section 7.3).

7.2 Analytical laser model

A schematic energy level diagram of the molecules to be considered is shown in Fig. 7.1. The pump laser excites a transition between a rotational level (rotational quantum number J) of the vibrational ground state $|o\rangle$ and a rotational level with quantum number $J' = J + \Delta J$ of an excited vibrational level $|u\rangle$. $\Delta J = \pm 1$ for an R and P transition, respectively. The molecule can relax back to the vibrational ground state via an intermediate state $|i\rangle$. The time τ_u represents a characteristic time for collision induced vibrational relaxation back to the ground state if an intermediate state $|i\rangle$ is not occupied, that is $\tau_o = 0$. In general, other vibrational states can be involved in the relaxation paths shown in Fig. 7.1 with the two effective time constants being a simple representation of this situation. Such relaxation paths can include intermediate vibrational states that are located energetically between $|u\rangle$ and $|o\rangle$ and states with energies higher than $|u\rangle$ (vibrational ladder climbing). For an analytical approach let us first assume that rotational relaxation within one vibrational state is fast so that at all times a thermalized rotational population in $|o\rangle$ and $|u\rangle$ exists[1] The occupation numbers in a certain rotational state J at temperature T are thus given by

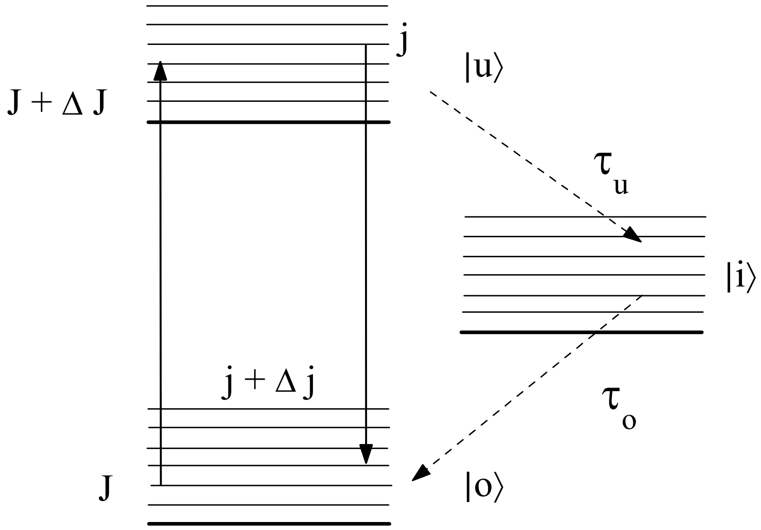

Figure 7.1: Simplified molecular energy level diagram. $|o\rangle$ and $|u\rangle$ denote vibrational states with rotational manifolds that in thermal equilibrium are populated according to a Boltzmann's distribution. $|i\rangle$ can represent an ensemble of states that participate in the relaxation of the excited vibrational state $|u\rangle$ to the ground state $|o\rangle$. τ_u and τ_o are effective relaxation times indicating how fast $|u\rangle$ is depopulated and $|o\rangle$ populated.

$$n_{o,u}(J) \;=\; (2J+1)\, e^{-\beta_{o,u}(J)}\, \frac{N_{o,u}}{S_{o,u}}\ , \tag{7.1}$$

---

[1] We will later scrutinize the ramifications of this assumption with the numerical model.

where $S_{o,\,u} \;=\; \sum_J (2J+1)\, e^{-\beta_{o,\,u}(J)}$ with $\beta_{o,\,u}(J) \;=\; E_{o,\,u}/\,(k_B T)$. For a simple diatomic or linear molecule the rotational energy relative to the rotational ground state of the respective vibrational level $E_{o,\,u} \;=\; \hbar^2 J\,(J+1)\,/\,(2I)$ where I is the moment of inertia, $N_{o,\,u}$ is the total population density in the vibrational states, and k_B is the Boltzmann constant.

The gain coefficient for a transition from $|u, j\rangle$ to $|o, j+\Delta j\rangle$ can be written as

$$g \;=\; \sigma_j \left[n_u(j) - \frac{2j+1}{2\,(j+\Delta j)+1} n_o\,(j+\Delta j) \right] \;, \tag{7.2}$$

where σ_j is the gain cross section. The occupation numbers needed to calculate g can be obtained from Eq. (7.1). The rate equations for the total occupation numbers in a certain vibrational level in steady state are:

$$\frac{dN_o}{dt} \;=\; -R_p \frac{2J+1}{S_o} e^{-\beta_o(J)} \left[N_o - \frac{S_o}{S_u} e^{\Delta\beta_{uJ}} N_u \right] + \frac{N_i}{\tau_o} = 0 \tag{7.3a}$$

$$\frac{dN_i}{dt} \;=\; \frac{N_u}{\tau_u} - \frac{N_o}{\tau_o} = 0 \tag{7.3b}$$

$$N_t \;=\; N_u + N_o + N_i \;, \tag{7.3c}$$

where $\Delta\beta_{uJ} = \beta_o\,(J) - \beta_u\,(J+\Delta J)$, and the pump rate (photons/s) $R_p = \phi_p\,\sigma_J$ is the product of the pump photon flux and the absorption cross section.

Assuming $S_o = S_u = S$, the gain coefficient becomes

$$g\,(J, \Delta J, j, \Delta j) = \\ \sigma_j \frac{2j+1}{S} e^{-\beta_u\,(J)}\, N_t \left[\frac{\tau_u R_p\, e^{-\beta_o(J)} \left(1 - e^{\Delta\beta_{uJ} + \Delta\beta_{uj}}\right) - e^{\Delta\beta_{uj}}}{\frac{S}{2J+1} + R_p e^{-\beta_o(J)}\, \left(\tau_u + \tau_o + \tau_u\, e^{\Delta\beta_{uJ}}\right)} \right] \;, \tag{7.4}$$

where $\Delta\beta_{uj} = \beta_u\,(j) - \beta_o\,(j+\Delta j)$. The assumption of equal S_i was made to simplify the analytical expressions.

From Eq. (7.4) it is obvious that positive gain can occur only if $\Omega = \Delta\beta_{uJ} + \Delta\beta_{uj} < 0$. This means that the laser photon energy must be smaller than the pump photon energy. The condition,

$$\Omega = -\frac{\hbar^2}{2I}\left(\Delta J^2 + 2J\Delta J + \Delta J + \Delta j^2 + 2j\Delta j + \Delta j\right)/k_BT < 0 \ , \tag{7.5}$$

determines which combinations of pump and lasing transitions are not possible for lasing to occur independently of the pump rate and relaxation parameters. For example, excitation of a P-line transition and lasing on a R-line transition would result in $\Omega > 0$, which according to Eq. (7.4) does not permit positive gain.

To include the lasing process from state $|u, j\rangle$ to state $|o, j + \Delta j\rangle$ we can add to Eq. (7.3a) a term

$$R_L \frac{2j+1}{S}\, e^{-\beta_o(j+\Delta j)}\, \left[e^{-\Delta\beta_{uj}} N_u - N_o\right] \ , \tag{7.6}$$

where $R_L = \sigma_j\, \phi_L$ is the product of the laser emission cross section σ_j and the laser photon flux ϕ_L. The rate equation for ϕ_L after steady state has been reached can be written as,

$$\frac{d\phi_L}{dt} \;=\; c\sigma_j\phi_L \frac{L_g}{L}\left\{\frac{2j+1}{S} e^{-\beta_o(j+\Delta j)}\, \left[e^{-\Delta\beta_{uj}} N_u - N_o\right]\right\} - \frac{\phi_L}{\tau_c} = 0 \ , \tag{7.7}$$

where τ_c is the photon cavity lifetime, L is the cavity length and L_g is the length of the gain medium. The cavity lifetime $\tau_c = 2L/c/\left[-\ln(1 - R_L) - \ln(R_M)\right]$ is determined by the reflectance R_M of the outcoupler and the combined other linear losses per roundtrip, R_L.

Note that to force this one-mode laser operation on the transition from j to $j + \Delta j$, if necessary, a suitable spectral filter can be placed in the cavity preventing all other lasing transitions. In steady state the gain coefficient equals the cavity loss coefficient:

$$g_L = \sigma_j \frac{L_g}{L} \left\{ \frac{2j+1}{S} e^{-\beta_o(j+\Delta j)} \left[e^{-\Delta\beta_{uj}} N_u - N_o \right] \right\} = \frac{1}{c\tau_c} \ . \tag{7.8}$$

Equations (7.8) and (7.3a) with the addition of the laser term Eq. (7.6) yield the steady-state laser output:

$$\begin{aligned} P_L &= h\nu_j A L_g Q \left\{ R_p \frac{2J+1}{S} e^{-\beta_o(J)} \left[N_t(1-e^{\Omega}) - \frac{S'}{\gamma\tau_c}(1+\gamma e^{\Delta\beta_{uJ}}) \right] \right. \\ &\quad \left. - \frac{1}{\tau_u} \left[\frac{S'}{\tau_c} + N_t e^{\Delta\beta_{uj}} \right] \right\} \ , \end{aligned} \tag{7.9}$$

where h is the Plank constant , ν_j is the laser frequency and A is the cross section of the laser beam which is assumed to be the same as the pump beam cross section,

$$\begin{aligned} \gamma &= \frac{\tau_u}{\tau_u + \tau_o} \ , \\ S' &= \frac{L}{L_g} \frac{S e^{\beta_u(j)}}{(2j+1)\, c\sigma_j} \ , \end{aligned}$$

and

$$Q = \gamma \frac{e^{\beta_o(j+\Delta j)}}{(1+\gamma e^{-\Delta\beta_{uj}})\, e^{\beta_u(j)}} \ .$$

As is obvious from Eq. (7.9) , to obtain lasing, a pump photon rate

$$\begin{aligned} R_p &> \frac{S e^{\beta_o(J)}}{(2J+1)\,\tau_u} \left[\frac{S' + \tau_c N_t e^{\Delta\beta_{uj}}}{\tau_c Nt\,(1-e^{\Omega}) - S'\,(\gamma^{-1} + e^{\Delta\beta_{uJ}})} \right] \\ &= R_{th} \ , \end{aligned} \tag{7.10}$$

is required, where R_{th} is the threshold pump photon rate. The, threshold pump power is then $P_{th} = R_{th}\, h\nu_p\, A\, / \sigma_J$, where ν_{p} is the pump laser frequency. From, Eq. (7.10) one sees that for a given molecular energy structure,

$$\gamma > \gamma_{min} = \left[\frac{\tau_c\, N_t(1-e^{\,\Omega})}{S'} - e^{\,\Delta\beta_{uJ}} \right]^{-1} \tag{7.11}$$

is necessary to enable positive gain. This imposes a condition on how fast the upper level can empty (τ_u) and how slowly the ground state can be repopulated (τ_o). It is also important to note that the energy spacing of the rotational states matters, which is contained in the term $(1 - e^{\Omega})$ in Eq. (7.10). Larger spacings relax the conditions on the pump fluence and lower the value of γ_{min}.

The laser output power Eq. (9) can be rewritten as

$$P_L = \eta\ (P_p - P_{th})\ , \tag{7.12}$$

where P_p is the pump power and

$$\eta = \frac{\nu_j}{\nu_p}\, Q\, \sigma_J\, L_g \frac{2J+1}{S}\, e^{-\beta_o(J)} \left[N_t \left(1 - e^{\Omega} \right) - \frac{S'}{\gamma \tau_c} (1 + \gamma e^{\,\Delta\beta_{uJ}}) \right] \tag{7.13}$$

is the laser slope efficiency.

It should be noted that an optically thin active medium for the pump is assumed in the analytical approach which is of course detrimental to a high overall laser efficiency even though the slope efficiency can be made very high. The assumption was however necessary for the analytical approach, which assumes spatial uniformity. This situation can be reached under high pump saturation conditions. Using a numerical approach, we will show below that in a real system large overall pump absorption and laser efficiency can be achieved simultaneously.

7.3 Numerical laser model

The analytical approach assumes an instantaneous thermalization among the rotational states of the vibrational levels and an intracavity filter that permits only one line to lase. To test if the main qualitative conclusions drawn above are still valid under finite thermalization rates we used a computer model described in section 6.2 that simulates relaxation processes between the rotational states in detail. In our model we consider only collisions where $|\Delta J| = |J' - J| \leq 4$. The rotational rate constants were extrapolated from the experimental data using the modified energy gap (MEG) fitting law. The numerical model was simplified identically to the analytic model in which consider 3 vibrational states. However for each vibrational state, the total 30 rotational states were included.

7.4 Model predictions and discussions

HCN was chosen as an example. We consider for the pump process a transition from HCN (000), $J = 8$ to HCN (002), $J + \Delta J = 9$ and lasing from HCN (002), $j = 9$ to HCN (000), $j + \Delta j = 10$. The spectroscopic data of HCN can be found in section 3.3.

The necessary long interaction lengths between the active gas and high pump intensities can in principle be realized using hollow fibers which have been used for example for saturated absorption spectroscopy with C_2H_2 [78] and for stimulated Raman scattering in H_2 [79]. Unless introduced otherwise, we assume the pump beam to have a uniform beam profile with a diameter of 10 μm and a 1.5 m long WG filled with 10 torr of HCN. The WG and outcoupling losses (assumed to be 5%) are lumped into the cavity round trip loss (linear loss).

Fig.7.2 shows the threshold pump power as a function of the cavity roundtrip loss. It is evident that small values of τ_o/τ_u are favorable. Smaller τ_o/τ_u ratios mean less efficient relaxation channels that compete with the laser process. The threshold pump power predicted by the analytical model is validated by the comparison to the numerical calculation for the chosen set of laser parameters. Note that the steady state condition from the analytical approach can be applied to pulsed excitation when the duration of the exciting pulse is longer than the effective vibrational relaxation

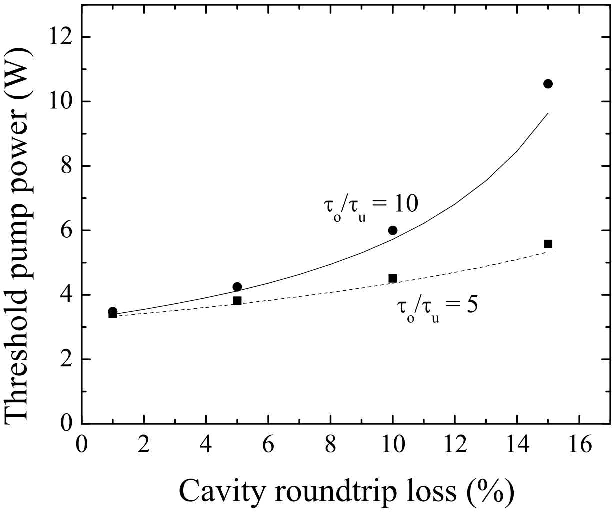

Figure 7.2: Pump power necessary to reach the laser threshold as a function of the cavity round trip loss for two different ratios τ_o/τ_u obtained from the analytical model (lines) and the numerical calculation (data points). Pump and laser beams having uniform beam profiles with diameters of 10 μm and a 1.5 m long WG filled with 10 torr of HCN were assumed.

times (τ_u and τ_o). Therefore the predicted threshold of CW excitation can be scaled to the expected peak threshold pump power of such a long pulse excitation.

Figure 7.3 compares the laser output obtained from the analytical and numerical simulation as a function of the ratio τ_o/τ_u. The horizontal bar indicates the probable range of τ_o/τ_u values for HCN that can be estimated from published kinetic molecular rates discussed in Appendix A.

As already suggested by Fig. 7.2, small ratios of τ_o/τ_e are favorable. It turns out that only one transition is lasing (from $|u,9\rangle$ to $|o,10\rangle$), channeling energy away from other possible laser lines. The insertion of a filter to obtain single line output is thus not necessary. The actual rotational relaxation rate of HCN for T = 300 K and p = 10 torr corresponding to a rotational thermalization of approximately 2 ns was used in Fig 7.3. The good agreement between the analytical and numerical results show that the assumption of an infinitely fast rotational thermalization is justified

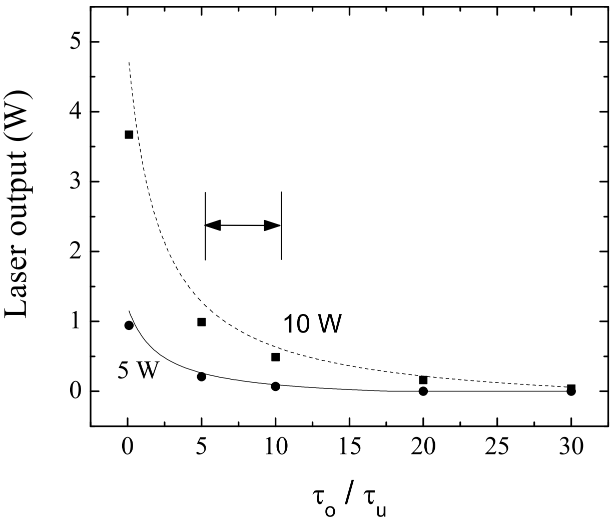

Figure 7.3: Laser output as a function of $\tau_\mathrm{o}/\tau_\mathrm{u}$ for two different pump powers obtained from the analytical model (lines) and the numerical calculation (data points). Pump and laser beams having uniform beam profiles with diameters of 10 μm and a 1.5 m long WG filled with 10 torr of HCN were assumed. Total linear losses of 5% are used for the calculations.

for these conditions.

Lower pressures and / or temperatures would decrease the rotational relaxation rates and the analytical model will no longer be able to describe the system adequately. To evaluate the range of thermalization rates for which the analytical model can be applied we compared the laser output power obtained from the analytical and numerical approach. Fig. 7.4 shows the ratio of the two output powers as a function of the rotational thermalization rate used in the numerical model. It is evident that as k'_R becomes large, which means fast rotational relaxation times, the results of the analytical and numerical models are approximately the same. In practice, such a situation can be approached by adding a buffer gas. A comparison of Figs. 7.2 and 7.3 shows that the behavior of the laser above threshold is more sensitive to a finite thermalization time than it is at threshold. The overall laser efficiencies cannot be predicted adequately by the analytical model as it is based on the assumption of

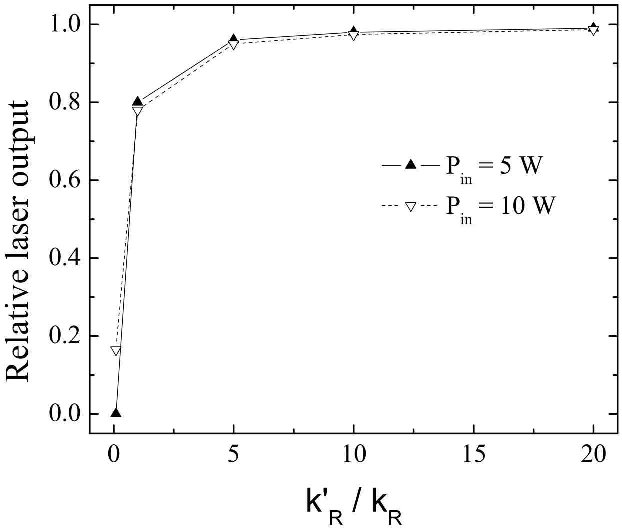

Figure 7.4: Relative laser output power obtained from the numerical and analytical model as a function of the rotational thermalization rate k'_R normalized to the actual rate k_R at 10 torr and 300 K. Pump and laser beams having uniform beam profiles with diameters of 10 μm and a 1.5 m long WG filled with 10 torr of HCN were assumed. Linear losses of 5% and $\tau_o/\tau_u = 5$ are used in the calculations.

axially homogenous gain and absorption. Since this type of laser requires relatively high pump saturation the laser efficiencies would be rather low. In practice, one would use conditions in which the pump saturation varies in order to increase the overall pump absorption and conversion to laser output. To analyze this situation numerically we divide our gain medium axially into slices of length Δz. We use the model described in Eqs. (7.3) to (7.7) for the population numbers and the laser gain in each slice, and assume $\tau_o/\tau_u = 0$, ($\tau_o = 0$) (no intermediate state) for simplicity. We consider two passes of the pump through the active medium. Lasing starts from spontaneous emission and we follow the temporal evolution of the laser output until steady state is reached. In each slice, the laser and the pump photon flux is the sum of the forward and backward propagating field. Interference effects (standing wave effects) are neglected. Figure 7.5 shows results of such a calculation for various HCN pressures. An increase in HCN pressure decreases τ_u. When the pump absorption

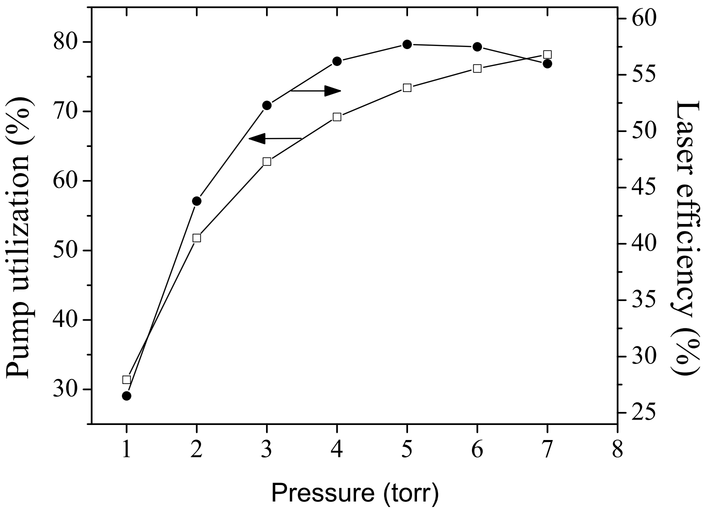

Figure 7.5: Pump utilization (fraction of absorbed pump) and laser efficiency as a function of HCN pressure. Pump power = 5 W, 20 μm WG diameter, 1.5 m long WG and WG loss = 0.02 dB/m), outcoupling loss =25%.

approaches 75% the laser efficiency is approximately 55%. No attempt was made to determine optimized operating conditions. However this example illustrates the fact that the pump field can couple efficiently to the laser field. The pump power that is not converted will contribute to heating. This represents the energy loss due to radiationless relaxation channels.

It should be noted that the condition $S_o = S_u$ assumed in section 7.2 is equivalent to the assumption that the rotational constants for the ground and excited vibrational state are identical. In general, the rotational constant decreases with increasing vibrational quantum number (cf. section 3.3) resulting in $S_o < S_u$. For HCN, the discrepancy between the rotational constants for (000) and (002) is about 1%. Thus for HCN the assumption that $S_o = S_u$ is well justified. In systems where S_u is considerably larger than S_o one can expect a smaller gain from the terminal pump state because more population is transferred to other rotational levels. At the same time the gain for transitions starting at other rotational levels and ending at

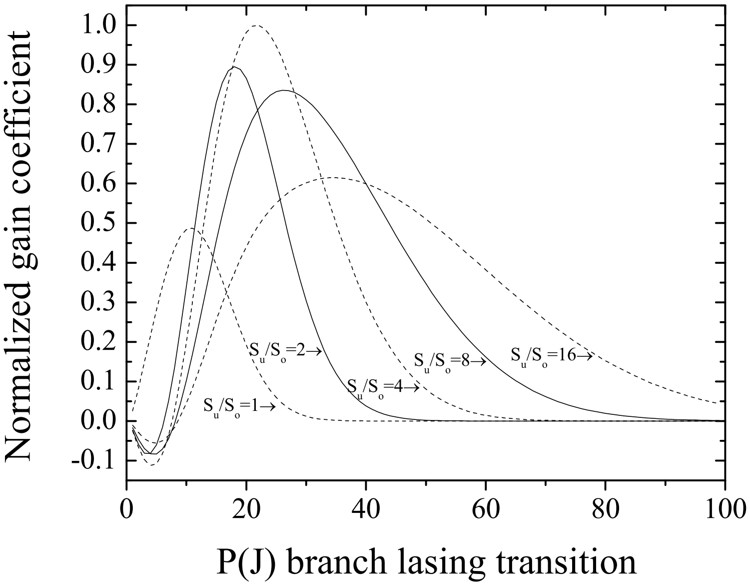

Figure 7.6: Normalized gain coefficient as a function of rotational state (J) of P branch lasing transition, i.e., P(J) for differen ratios S_u/S_o. The pump transition is from HCN(000), J = 8 to HCN(002), J = 9.

rotational levels of the vibrational ground state that have little thermal population may increase as shown in Fig. 7.6. An assessment whether the laser output from the strongest line increases or decreases if $S_o < S_u$ would require the evaluation of a real system and the outcome will depend on the system parameters.

7.5 Summary

The small quantum defect laser based on rotation-vibration transitions was analyzed using an analytical approach in which the instantaneous rotational relaxation (thermalization) condition is assumed. HCN is used as an example gas for the small defect laser. The lasing of HCN is possible resulting quantum efficiencies of ≈ 99 %. The conditions necessary for critical molecular relaxation parameters were derived under which lasing is possible. These conditions can be applied to similar other potential gases for the small defect laser systems such as C_2H_2 and HI which are attractive particularly for the C-band excitation. Numerical simulations suggest that the analytical predictions are approximately valid for a broad range of rotational thermalization rates and also applicable to pulse pumping if the pulse durations are sufficiently long. Long interaction lengths between the (focused) pump laser beam and the active gas can be realized using hollow fiber waveguide structures. Although for this small defect laser concept to work strong pump absorption saturation is required, the long interaction lengths can result in strong overall pump absorption. Numerical simulations predict overall laser efficiencies exceeding 55 %.

Chapter 8

Preliminary results on a gas filled hollow core fiber laser

The experiments and estimations were carried out in parallel to writing the thesis. We report here only on the proof of principle demonstration. The positive outcome of these first experiments opens up exciting new directions for future work.

Photonic bandgap fibers that have a hollow core are wave guides whose dispersion and loss characteristics can be controlled by the core size and the distribution and shape of additional voids in the material surrounding the core [10]. The name photonic bandgap stems from the similarity of solid state bands that disallow certain electronic energy states to exist within the photonic bandgap. Similarly certain photon modes are not allowed outside the core confining guiding modes to the hollow region [10]. Photonic bandgap hollow fibers are commercially available and core diameters are typically of the order of 20 μm or less. These fibers are often designed to guide in the visible and near infrared spectral region.

These fibers can be filled with a gas. It is tempting to explore the application of those fibers for nonlinear optics. The overlap of the radially confined excitation laser and the nonlinear medium can be made large reducing the power necessary for generating nonlinear optical signals. In the past groups have successfully for example stimulated Raman scattering in H_2 [79].

Our plan was to use a gas filled hollow fiber and demonstrate the first laser based on population inversion. A successful demonstration of this concept would open up many new and exciting avenues for optically pumped gas lasers.

From the previous chapters we know that for example acetylene can lase at about 3 μm when excited by a pulsed laser emitting at about 1.5 μm. While guiding at 1.5 μm is not problematic, in fact many commercial hollow-core fiber lasers will permit this, guiding at 3 microns is a problem. Presently commercially available hollow core fibers do not guide in this wavelength region.

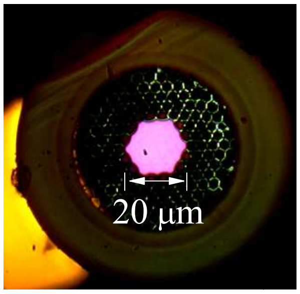

Figure 8.1: Cross section of kagome lattice structure. Supplied by K. Corwin (KSU) and F. Benabid (University of Bath).

In 2006, a group from Bath University (UK) succeeded in demonstrating hollow core fibers that are not based on photonic bandgaps [80]. Rather these hollow fiber designs allow fiber guided modes to cohabit with cladding modes without notably interacting. This is possible by a high degree of transverse field mismatch between the core and fiber modes [80]. There are circumstances where cladding and fiber modes of the same frequency can coexist. Figure 8.1 shows the cross-section of such a fiber with a Kagome lattice structure.

Core diameters exceeding 70 μm are possible. Although the guiding properties at 3 μm were unknown the relatively large optical gain prompted us to evaluate those fibers for OPMLs.

The experiments were carried out at UNM in collaboration with Dr. Nampoothiri and with Kansas State University (A. Jones and K. Corwin) and University of Bath (F. Benabid). As a first step the losses were measured in transmission experiments where the fiber was successively cut shorter. A ns OPO served as light source. Loss coefficients of about 20 dB/m were obtained, which hinted that 3 μm radiation can propagate as a weakly guided mode.

Encouraged by these results we used a simple model to predict the likelihood of lasing of such a fiber filled with acetylene and pumped by a 5-ns OPO pulse. We first propagated a pump pulse through the fiber assuming that created a population inversion. We then send a weak probe pulse and calculated the output energy. Both pump pulse and probe pulse are Gaussian pulse. The output was independent of the incident probe pulse energy if the latter was small enough as it should be. To take into account propagation effects the fiber was divided into slices for which the pump attenuation and probe amplification were calculated using the equation [81]

$$I_2(t) = I_1(t)\frac{G_0\ e^{u_1(t)}}{1 + G_0\left(e^{u_1(t)} - 1\right)}\ , \tag{8.1}$$

where $I_1(t)$ is the input(pump or probe) pulse intensity, $I_2(t)$ is the output (pump or probe) pulse intensity, G_0 is the small signal gain (absorption) $\left(e^{(-)g\ l_g}\right)$ and $u_1(t)$ is the energy normalized to the saturation energy [81],

$$u_1(t) = \frac{\omega_1(t)}{\omega_s}\ . \tag{8.2}$$

Here $\omega_1(t) = \int_{-\infty}^{t} I_1(t)dt$ and the saturation energy per unit area,

$$\omega_s = \frac{h\nu}{2\sigma} \tag{8.3}$$

where σ is the gain (absorption) cross section.

After each amplification step (slice) the pump and laser intensities were subject to linear fiber loss. The line width of OPO is wider than the line width of C_2H_2. To simulate pulse propagation and saturating conditions would require solving a set of Maxwell-Bloch equation and to take into account homogeneous and inhomogeneous contributions to the line broadening. For order-of-magnitude estimations we used some crude approximations. We determined an effective absorption cross section that takes into account the practical overlap of pump pulse spectrum and absorption profile. This cross section σ_{eff} was obtain from experiment where the small signal transmission of the pump through a 0.8 m long cell (2 torr of C_2H_2) was determined. From this σ_{eff}= 3.4×10^{-19}cm^2.

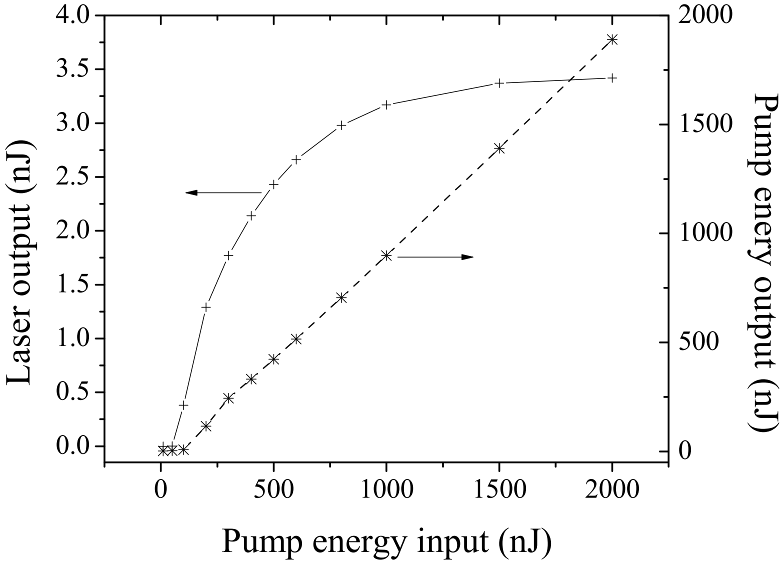

Figure 8.2: Calculated laser energy and the pump energy as at the output of the fiber as a function of the pump input energy. The fiber length = 1.65 m, and pressure of 2 torr. Fiber diameter is 20 μm

Figure 8.2 shows the expected laser energy as a function of the pump energy coupled into the fiber for a fiber core diameter of 20 μm and a gas pressure of 2 torr.

It also depicts the pump energy at the output of the fiber as a function of the pump input energy.

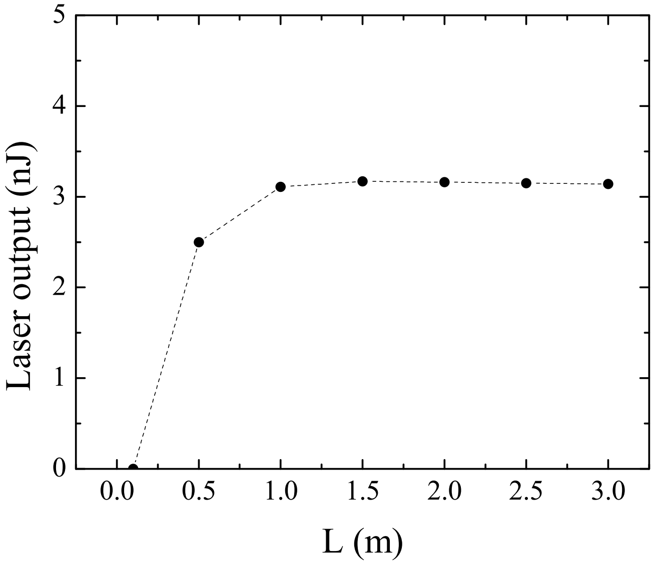

Figure 8.3: The laser energy as a function of the fiber length.

Figure 8.3 displays the calculated laser energy as a function of the fiber length with the energy input of 1 μJ for the gas pressure of 2 torr. From the simulations it seemed possible to reach the laser threshold. Note, many fiber laser do not need external mirrors for feedback provided the net gain is large enough for the output to saturate the gain medium.

The experimental setup is sketched in Figure 8.4 together with a photo of the laser. The two ends of a 1.65-m long fiber (Kagome structure, University of Bath) were inserted into small vacuum chambers (KSU), which were then filled with acetylene. Using an acetylene reference cell the OPO was tuned to the R(7) absorption line. The pulses were focused through the window of the vacuum chamber and coupled into the hollow fiber. In these first experiments no attempts were made to optimize coupling efficiencies. Figure 8.5 shows the fiber laser output as a function

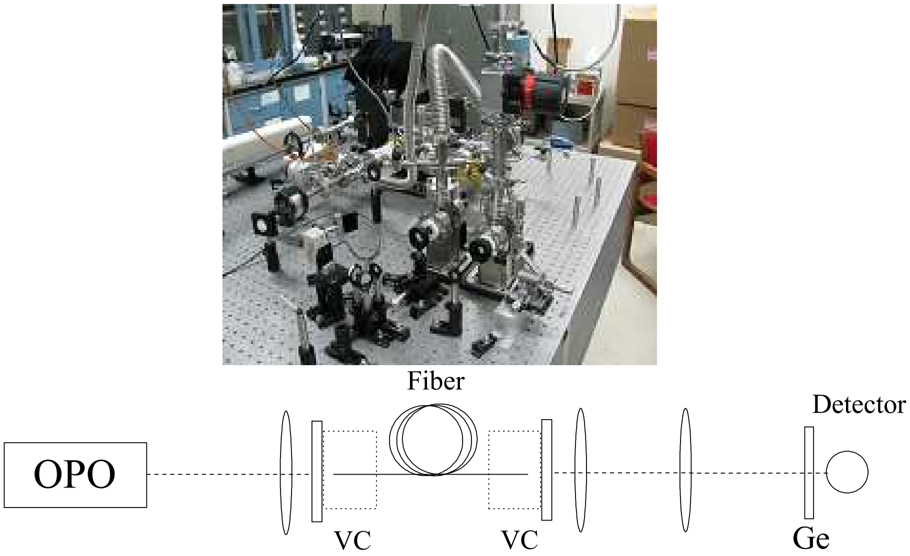

Figure 8.4: The experiment setup of the fiber laser. VC denotes to the vacuum chamber.

of pump pulse energy for 2 torr of gas pressure. The laser output shows the onset of saturation as the pump pulse starts to saturate the absorption transition.

Figure 8.6 depicts the spectrum of the laser output. The laser transitions are assigned to P(9) and R(7), and are the same as what we have observed in the conventional laser cavity (see Fig. 5.4).

This was the first demonstration of a gas-filled hollow fiber laser based on population inversion. The output energy is low because of gain media saturation (saturation fluence 200 $\mathrm{mJ/cm^2}$ at 2 torr). Some improvements here are possible using a fiber with a larger core diameter. The real advantage of this system is the low threshold pump energy owing to the long interaction length of a confined pump and “laser mode”. Future work should involve the demonstration of a CW acetylene or HCN laser along the schema discussed in Chapter 7. We estimated that a pump power in the range of 5 to 10 W is necessary to reach the laser threshold for a 1.5 m long

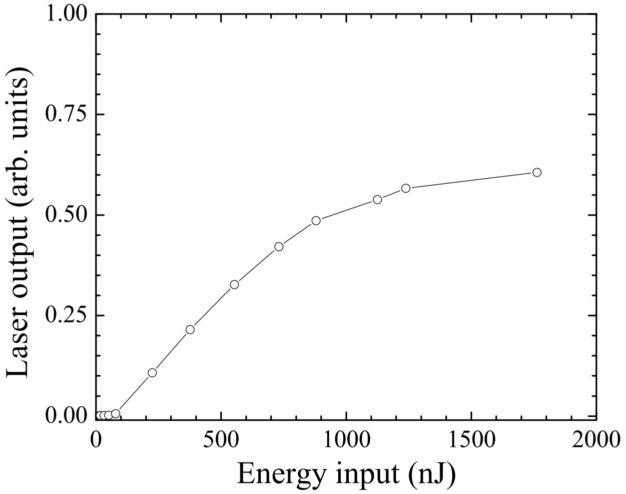

Figure 8.5: Measured fiber laser output as the function of pump pulse energy at gas pressure of 2 torr.

waveguide. While these pump lasers are commercially available, the existing 5-W pump in our laboratory may be not sufficient.

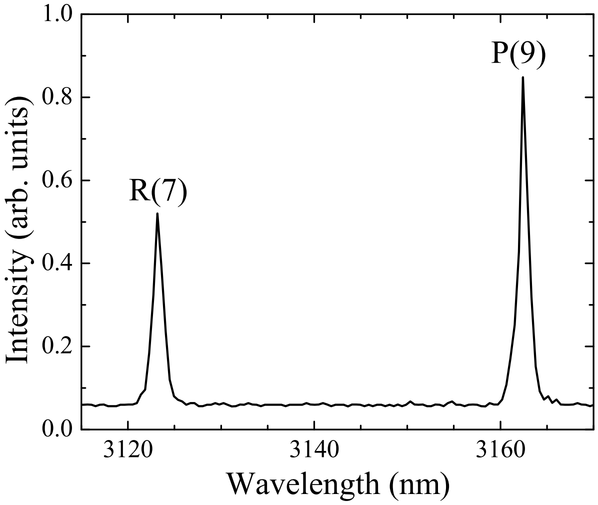

Figure 8.6: The spectrum of the fiber laser output.

8.1 Summary

We demonstrate the first hollow fiber gas laser based on population inversion. Pumping the gas filled fiber (1.65 m) with μJ pulses from a 5-ns OPO resulted in the emission of two laser lines at $3.12\,\mu$m and $3.16\,\mu$m. These lines correspond to the R(7) and P(9) transitions originating from the initially populated rotational state of the (10100) vibrational level and terminating at the (10000) vibrational state of acetylene. In this configuration both the pump and laser pulses saturate the respective transitions. A preliminary model has been developed to predict the laser output as a function of the pump input. The laser combines the advantages of fiber lasers, such as the confinement of pump and laser light over long interaction lengths in a compact configuration, with those of gas lasers: high damage thresholds, a wide variety of possible (eye-safe) emission wavelengths in the atmospheric transmission window, and the potential for coherent emission from mutually incoherent pump sources.

Chapter 9

Summary and outlook

The thesis comprises experimental and theoretical research on optically pumped molecular gas lasers. A theoretical model was developed to predict the performance of such lasers and make predictions concerning their spectral tunability and power and energy scaling [82]. The model takes into account the population of 30 rotational states for each vibrational state considered. It follows the population evolution due to the interaction with the pump and laser field, and due to collisions of the molecule with other active or buffer gas molecules. Heat dissipation and temperature changes in the active volume are taken into account in an approximate manner. As an example the model was applied to a second-overtone, optically pumped HBr laser. The main conclusions from this simulation are:

- Simulations show that both pulsed and CW HBr lasers can operate on the full lasing cascade, realizing efficiencies approaching to 80% and 93% respectively.
- Spectral tuning to a desired output is possible by an intracavity filter without sacrificing much of the laser efficiency for pulse and CW pumping.

The stability and performance of an existing, second-overtone pumped HBr laser was enhanced by improving the temperature tuning of the Nd:YAG pump laser operating at 1.34 μm. Improved stability resulted from the stabilization of the pump laser cavity to the seed laser frequency. Five lasing transitions have been observed with a low energy pumped HBr laser [64].

These experimental and theoretical results indicate that the HBr laser is a viable energy scalable system that can be operated pulsed and CW with the output tuned to regions of high atmospheric transmission around 4 μm. Further improvements are possible by using isotopically pure HBr, which was prohibitively expensive for our small-scale laboratory system. Waveguide structures (for example capillaries) are attractive cavity configurations.

Our search for attractive matches of gases and pump sources resulted in the selection of HCN and C_2H_2. Both gases can be pumped with diode and fiber lasers emitting in the telecommunication C band at about 1.5 μm. Rate constants were obtained from the literature and estimated when not available to assess the potential of using the molecules as active laser media. Two potential operating scenarios emerged. Pulsed excitation and pulsed output at about 3 μm and CW excitation and CW output at in the 1.5 μm region with a small Stokes shift relative to the pump. Operational parameters were estimated using computer simulations and an analytical approach. Lasing of both gases in a gas cell was demonstrated with a ns pump pulse obtained from an OPO [68]. The two spectral components of the laser output correspond to the 10100 → 10000 transition of C_2H_2 and to the 002 → 001 transition of HCN, respectively. Due to the large gain directed output (ASE) was also observed without external cavity mirrors.

An analytical approach was chosen to analyze the potential of a CW laser with small Stokes shift relative to the pump based on either C_2H_2 or HCN. It was estimated that a pump power in the range of 5 W to 10 W is sufficient to reach the laser threshold. Theoretical laser efficiencies of 55% are possible [83].

The experimental results and data from simulations for C_2H_2 and HCN indicated the possibility to achieve lasing in a gas filled hollow core fiber laser. We used a Kagome structure [80] because of the existence of weakly guided modes in the 3 μm region in contrast to commercially available photonic bandgap fibers. Lasing was demonstrated for a ns pump and C_2H_2 gas, which represents the first gas filled hollow fiber laser based on population inversion [84].

We have accomplished many aspects of theoretical and experimental studies of optically pumped molecular lasers. Our publications from this thesis are listed below

1. A. Ratanavis, N. Campbell, A. V. V. Nampoothiri, and W. Rudolph. Optically pumped HBr gas laser operating in regions of high atmospheric transmission. Proc. SPIE. 7005:70051P, 2008.

2. A. Ratanavis, N. Campbell, A. V. V. Nampoothiri, and W. Rudolph. Performance and spectral tuning of optically overtone pumped molecular lasers. IEEE J. Quant. Electron. 45:488, 2009.

3. A. Ratanavis, N. Campbell, and W. Rudolph. Feasibility study of optically pumped molecular lasers with small quantum defect. J. Opt. Commun. In press, 2009.

4. A. V. V. Nampoothiri, A. Ratanavis, N. Campbell, and W. Rudolph. Molecular C_2H_2 and HCN lasers pumped by an optical parametric oscillator in the 1.5-μm band. Optics Express. Submitted, 2009.

5. V. Nampoothiri, A. M. Jones, A. Ratanavis, R. Kadel, N. Wheeler, F. Couny, F. Benabid, B. R. Washburn, K. L. Corwin, and W. Rudolph. Mid-IR laser emission from a C2H2 gas filled Hollow Core Photonic Crystal Fiber. Photonics West. Submitted, 2010.

From this thesis two major avenues for future work emerge - the exploration of new concepts and further development of designs researched in this thesis.

- As new efficient narrow-band fiber and diode pump sources are developed other matches of gaseous active media and pump sources should be explored and more efficient cavity geometries investigated. HI molecules, for example seem already be attractive candidates because available waveguide structures based on coated capillaries should be explored to increase the mode overlap of pump and laser.

- Research based on the two gases HCN and C_2H_2 should continue to explore their full capability as laser media. This must involve the measurement of fundamental rate constants and their behavior if buffer gas is added. Another open question (because of the lack of sufficient spectroscopic data) is the possibility of a second lasing cascade back to the ground state. This would improve the efficiency dramatically.

- Finally, the demonstration of the gas filled hollow fiber lasers will likely spur the development of compact gas lasers with low pump thresholds. Improvements in the Kagome design can lead to considerably lower losses in the mid infrared spectral region. This in turn would lower the threshold even more. The hollow fibers can be connected to traditional fiber systems to deliver the pump at 1.5 μm. There is also the option of pumping through the fiber cladding. The combination of CW pumping at 1.5 μm and the use of larger core diameters could lead to narrowband output powers. This would be an attractive step toward using these systems to coherently combine the output of several independent laser sources.

Appendix A

HCN relaxation and estimation of τ_o and τ_u

Figure A.1 illustrates the most probable relaxation pathway of molecules from the (002) state to the ground state. The total removal relaxation time of the upper laser level (τ_u) discussed in section 7.2 can be calculated by the rate k_{002} given in Table 3.9 where $\tau_u \simeq k_B T / (133 \, p k_{002})$. However the relaxation pathway of molecules from the (001) state to the ground state have involved the collision processes described in Eqs. 3.3, 3.3 and 3.3.

The rate equations for the population numbers N_{001}, N_{100} and N_{010} are,

$$\begin{aligned}
\frac{dN_{001}}{dt} &= -\frac{N_{001}}{\tau_{001}} \\
\frac{dN_{010}}{dt} &= \frac{N_{001}}{\tau_a} - \frac{N_{010}}{\tau_{010}} \\
\frac{dN_{100}}{dt} &= \frac{N_{001}}{\tau_b} - \frac{N_{100}}{\tau_{100}} \\
N &= N_{000} + N_{001} + N_{010} + N_{100} \ , \qquad \text{(A.1)}
\end{aligned}$$

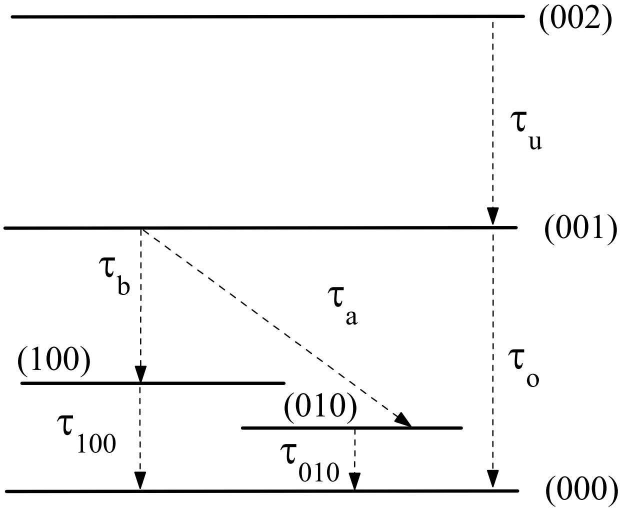

Figure A.1: Simplified relaxation pathway from the (002) state to the ground state.

where

$$\frac{1}{\tau_{001}} = \frac{1}{\tau_a} + \frac{1}{\tau_b} \;, \tag{A.2}$$

with $\tau_{001} \simeq k_B T/\left(133\ p k_{001}\right)$, $\tau_{010} \simeq k_B T/\left(133\ p k_{010}\right)$ and $\tau_{100} \simeq k_B T/\left(133\ p k_{100}\right)$.

Assuming the initial condition $N_{100}(0) = N_{010}(0) = 0$ and $N_{001}(0) = N^0_{001}$, the general solution for $N_{000}(t)$ is

$$\begin{aligned} N_{000}(t) \;=\; & N - N^0_{001}\left[\frac{\tau_{010}\tau_{001}}{\tau_a(\tau_{010}-\tau_{001})}\left(e^{-t/\tau_{010}} - e^{-t/\tau_{001}}\right)\right. \\ & + e^{-t/\tau_{001}} \\ & \left. + \frac{\tau_{100}\tau_{001}}{\tau_b(\tau_{100}-\tau_{001})}\left(e^{-t/\tau_{100}} - e^{-t/\tau_{001}}\right)\right] \;. \end{aligned} \tag{A.3}$$

Because of the similar nature of the (001) and (100) vibrational (stretch) modes we assume that $k_{001} \simeq k_{100}$. Derived from experiments a lower limit of the relaxation rate out of the (010) state has been reported. The corresponding rate k_{010} is of about the same order of magnitude as k_{001}. From Table 3.9 we may assume $k_{001} \approx k_{100} \approx k_{010}$, thus $\tau_{001} \approx \tau_{100} \approx \tau_{010}$ and the solution of $N_{000}(t)$ simplifies to,

$$N_{000}(t) = N - N_{001}^{0} e^{-t/\tau_{001}} \left(1 + \frac{t}{\tau_{001}}\right) . \tag{A.4}$$

The time after which the ground state is 63% repopulated is used for an estimate of τ_o. From the k_{001} listed in the Table 3.9 we obtain τ_o, which is about 5 to 10 times longer than τ_u.

Strictly speaking the above discussion applies only to a weakly excited gas where collisions essentially occur only with ground state molecules. The situation is more complicated under strong pumping conditions. As a result vibrational ladder climbing is possible, which adds additional relaxation pathways. For most of these channels relaxation rates are not known. This may increase τ_o and τ_u compared to the case discussed above.

References

[1] T. H. Maiman. Stimulated optical radiation in ruby. *Nature*, 187:493, 1960.

[2] J. Hecht and D. Teresi. *Laser: Light of a Million Uses.* Dover Publications, 1998.

[3] A. Javan, W. R. Bennett, and D. R. Herriott. Population inversion and continuous optical maser oscillation in a gas discharge containing a He-Ne mixture. *Phys. Rev. Lett.*, 6:106, 1961.

[4] C.R. Jones. Review of laser-pumped molecular lasers. *Tenth international sysposium on gas flow and chemical lasers*, 121:460, 1995.

[5] Jeff Hecht. Photonic Frontiers: beam combining - combining beams can boost total power. www.laserfocusworld.com.

[6] W.F. Krupke, R.J. Beach, V.K. Kanz, and S. A. Payne. Resonance transition 795-nm rubidium laser. *Opt. Lett.*, 28:2336, 2003.

[7] B.V. Zhdanov, T. Ehrenreich, and R.J. Knize. Highly efficient optically pumped cesium vapor laser. *Opt. Commun.*, 260:696, 2006.

[8] B. V. Zhdanov, A. Stooke, G. Boyadjian, A. Voci, and R. J. Knize. Rubidium vapor laser pumped by two laser diode arrays. *Opt. Lett.*, 33:208, 2008.

[9] C. S. Kletecka, N. Campbell, C. R. Jones, J. W. Nicholson, and W. Rudolph. Cascade lasing of molecular HBr in the four micron region pump by a Nd:YAG laser. *IEEE J. Quant. Electron.*, 40:1471, 2004.

[10] F. Benabid, F. Couny, J. C. Knight, T. A. Birks, and P. St J. Russell. Compact, stable and efficient all-fibre gas cells using hollow-core photonic crystal fibres. *Nature*, 434:488, 2005.

[11] G.M. Barrow. *The structure of molecules: an introduction to molecular spectroscopy.* W.A. Benjamin, 1964.

[12] D. C. Harris and M. D. Bertoluci. *Symmetry and spectroscopy.* Dover publication, 1989.

[13] H. Kuhn and H. D. Forsterling. *Principles of physical chemistry.* John Wiley & Sons, Ltd, 2000.

[14] D. A. McQuarrie and J. D. Simon. *Physical chemistry: A molecular approach.* University science book, 1997.

[15] J. M. Hollas. *Modern spectroscopy.* John Wiley & Sons, Ltd, 2005.

[16] P. F. Bernath. *Spectra of atom amd molecules.* Oxford university press, 1995.

[17] N. Davidson. *Statistical mechanics.* McGraw-Hill book company. Inc., 1962.

[18] G. Herzberg. *Molecular spectra and molecular structure: Infrared and Raman spectra of polyatomic molecules.* Van Nostrand Reinhold company, 1945.

[19] S. L. Gilbert and W. C. Swann. Pressure-induced shift and broadening of 15101540-nm acetylene wavelength calibration lines. *J. Opt. Soc. Am. B.*, 17:1263, 2000.

[20] P. W. Milonni and J. H. Eberly. *Lasers.* John Wiley & Sons, Inc, 1988.

[21] J.J. Olivero. and R.L. Longbothum. Empirical fits to the Voigt line width: A brief review. *J. Quan. Spec. Rad*, 17:233–236, 1977.

[22] A. Tramer, C. Jungen, and F. Lahmani. *Energy dissipation in Molecuar systems.* Springer, 2005.

[23] J. T. Yardley. *Introduction to molecular energy transfer.* Academic press, 1980.

[24] P. Pernage and P. Niay. Absorption intensities for vibration-rotation bands and the dipole-moment expansion of HBr. *J. Quant. Spectrosc. Radiat. Transfer.*, 18:315, 1977.

[25] H. C. Miller, D. T. Radzykewycz Jr., and G. Hager. Optically pumped mid-infrared HBr laser. *IEEE J. Quant. Electron.*, 30:2395, 1994.

[26] P. Pernage and P. Niay. Erratum. *J. Quant. Spectrosc. Radiat. Transfer.*, 25:95, 1981.

[27] S. Chou, D. S. Baer, and R. K. Hansan. High-resolution measurements of HBr transitions in the first overtone band using tunable diode lasers. *J. Mol. Spectrosc*, 200:138, 2000.

[28] V. Braun and P. F. Bernath. Infrared emission spectroscopy of HBr. *J. Mol. Spectrosc.*, 167:282, 1994.

[29] N. Nishimiya, T. Yukiya, T. Ohtsuka, and M. Suzuki. Laser spectroscopy of vibrationrotation lines in the 3←0, 5←0, and 6←0 overtones of HBr. *J. Mol. Spectrosc.*, 182:309, 1997.

[30] M. Heaven. Tech. rep. *unpublished*, 2007.

[31] S. P. Phipps, T. C. Smith, G. D. Hager, M. C. Heaven, J. K. McIver, and W. G. Rudolph. Investigation of the state-to-state rotational relaxation rate constants for carbon monoxide (CO) using infrared double resonance. *J. Chem. Phys.*, 116:9281, 2002.

[32] D. Chen and L. Chen. Vibration-to-rotation energy transfer in HBr and DBr mixtures. *J. Chem. Phys.*, 56:3315, 1972.

[33] J. Dasch and B. Moore. Single quantum vibrational energy transfer from HCl (v=2) and HBr(v=2). *J. Chem. Phys.*, 72:4117, 1980.

[34] M. Hopkins and L. Chen. Vibrational relaxation of HBr ($v = 1$) state in methane, water, helium, and hydrogen gaseous mixtures. *J. Chem. Phys.*, 59:1495, 1973.

[35] A. Horwitz and S. Leone. Laser-excited resonant isotopic V→V energy transfer: $H^{35}ClH^{37}Cl$, $H^{79}BrH^{81}Br$, $D^{35}ClD^{37}Cl$, and $D^{79}BrD^{81}Br$. *J. Chem. Phys.*, 69:5319, 1978.

[36] P. F. Zittel and C. B. Moore. Vibrational relaxation in HBr and HCl from 144 K to 584 K. *J. Chem. Phys.*, 59:6636, 1973.

[37] Y. Noter, I. Burak, and A. Szoke. Temperature dependence of vibration-to-vibration energy transfer in HCl and HBr. *J. Chem. Phys.*, 59:970, 1973.

[38] A. M. Smith, S. L. Coy, and W. Klemperer. Fourier transform spectra of overtone bands of HCN from 5400 to 15100 cm^{-1}. *J. Mol. Spectrosc.*, 134:134, 1989.

[39] A. G. Maki, G. Mellau, S. Klee, M. Winnewisser, and W. Quapp. High-temperature infrared measurements in the region of the bending fundamental of $H^{12}C^{14}N$, $H^{12}C^{15}N$, and $H^{13}C^{14}N$. *J. Mol. Spectrosc.*, 202:67, 2000.

[40] HITRAN. Hitran database. cfa-www.harvard.edu/hitran/.

[41] J. Wu, R. Huang, M. Gong, A. Saury, and E. Carrasquillo M. Rotational energy transfer in highly vibrationally excited HCN. *J. Chem. Phys.*, 99:6474, 1993.

[42] P. W. Hasting, M. K. Osborn, C. M. Sadowski, and I. W. M. Smith. Vibrational relaxation of HCN(002). *J. Chem. Phys.*, 78:3893, 1983.

[43] A. Hariri, A. B. Peterson, and C. Wittig. Electronicvibrational energy transfer from Br($4^2P_{1/2}$) to HCN, and deactivation of HCN (001). *J. Chem. Phys.*, 65:1872, 1976.

[44] A. B. Peterson and I. W. M. Smith. Relaxation of HCN (001) using stimulated electronic raman scattering in Cs vapor as a tunable infrared source. *J. Chem. Phys.*, 71:3346, 1979.

[45] J. A. McGarvey, N. E. Friedman Jr., and T. A. Cool. Vibrational energy transfer in HFHCN, DFHCN, and H_2HCN mixtures. *J. Chem. Phys.*, 66:3189, 1977.

[46] B. D. Cannon, J. S. Francisco, and I. W. M. Smith. The relaxation of HCN(101) by V-T,R and V-V energy transfer. *Chem. Phys.*, 89:141, 1984.

[47] B. D. Cannon and I. W. M. Smith. The relaxation of HCN(011) by V-T,R and V-V energy transfer. *Chem. Phys.*, 83:429, 1984.

[48] G. S. Arnold and I. W. M. Smith. Vibrational relaxation of HCN(001) by the noble gases, O_2, N_2 and CO. *J. Chem. Soc., Faraday Trans, 2*, 77:861, 1981.

[49] M. Herman, A. Campargue, M. I. El Idrissi, and J. Vander Auwera. Vibrational spectroscopic database on acetylene, $\mathrm{X^1\Sigma_g^+(12C_2H_2, 12C_2D_2, and 13C_2H_2)}$. *J. Phys. Chem. Ref. Data*, 32:921, 2003.

[50] W. C. Swann and S. L. Gilbert. Line centers, pressure shift, and pressure broadening of 1530-1560 nm hydrogen cyanide wavelength calibration lines. *J. Opt. Soc. Am. B.*, 22:1749, 2005.

[51] J. D. Tobiason, M. D. Fritz, and F. F. Crim. State-to-state relaxation energy transfer in highly vibratinally excited acetylene. *J. Chem. Phys.*, 97:7437, 1992.

[52] J. D. Tobiason, M. D. Fritz, and F. F. Crim. State-to-state relaxation of highly vibrationally excited acetylene by argon. *J. Chem. Phys.*, 101:9642, 1994.

[53] M. J. Frost and I. W. M. Smith. Energy transfer in the 3_1,2_1,4_1,5_1 fermi resonant states of acetylene. 2. vibrational energy transfer. *J. Phys. Chem.*, 99:1094, 1995.

[54] A. Miklavc and I. W. M. Smith. Vibrational relaxation of C_2H_2 and C_2D_2 by vibrationrotation, translation (VR, T) energy transfer. *Chem. Soc, Faraday Trans.2*, 84:227, 1988.

[55] I. W. M. Smith and J. F. Warr. Vibrational relaxation of $C_2H_2(v_3, v_2+v_4+v_5)$ in self-collisions and in collisions with the noble gases. *Chem. Phys. Lett.*, 173:70, 1990.

[56] M. O. Bulanin, A. V. Domanskaya, K. Kerl, and C. Maul. Spectral line parameters in the (3←0) overtone band of the HI molecule and line-mixing in the band head. *J. Mol. Spectrosc.*, 230:87, 2005.

[57] G. Guelachvili, P. Niay, and P. Bernage. Fourier transform high-resolution measurements on the 2←0, 3←0, 4← 0, 5←0 infrared absorption bands of HI and DI. *J. Mol. Spectrosc.*, 253:85, 1981.

[58] J. L. Ahl and T. A. Cool. Vibrational relaxation in the HF-HCl,HF-HBr,HF-HI, and HF-DF systems. *J. Chem. Phys.*, 58:5540, 1973.

[59] H. L. Chen, J. C. Stephenson, and C. B. Moore. Laser-excited vibrational fluorescence of HCI and the HCI—CO_2 laser. *Chem. Phys. Lett.*, 2:593, 1968.

[60] airliquide.com. Gas encyclopedia. http://encyclopedia.airliquide.com.

[61] C. L. Yaws. *Matheson gas data book*. McGraw-Hill Professional, 2001.

[62] W. W. McCormick. *Fundamentals of University Physics*. Macmillan.

[63] S. J. Davis, W. J. Kessler, K. W. Hotzclaw, and C.R. Jones. Laser-pumped Mid-ir gas-phase lasers. *Tenth international sysposium on gas flow and chemical lasers*, 121:469, 1995.

[64] A. Ratanavis, N. Campbell, A. V. V. Nampoothiri, and W. Rudolph. Optically pumped hbr gas laser operating in regions of high atmospheric transmission. *Proc. SPIE*, 7005:70051P, 2008.

[65] H.Kildal and T.F.Deutsch. Optically pumped infrared V-V transfer lasers. *Appl. Phys. Lett.*, 27:500, 1975.

[66] H. C. Tapalian, C. A. Michales, and G. W. Flynn. Midinfrared molecular gas lasers optically pumped by a continuously tunable infrared optical parametric oscillator. *Appl. Phys. Lett.*, 70:2215, 1997.

[67] J. H. S. Wang, J. Finzi, P. K. Baily, K. K. Hui, and G.W. Holleman. CW optical resonance transfer lasers (ORTL). *Journal De Physique*, 41:463, 1980.

[68] A. V. V. Nampoothiri, A. Ratanavis, N. Campbell, and W. Rudolph. Molecular C_2H_2 and HCN lasers pumped by an optical parametric oscillator in the 1.5-μm band. *Optics Express*, Submitted, 2009.

[69] H.Kogelnik and T. Li. Laser beams and resonators. *Appl. Opt.*, 5:1550, 1966.

[70] A. L. Golger and V. S. Letokhov. Population inversion due to saturation of absorption in molecular rotation-vibrational transition. *Sov. J. Quant. Electron*, 3:15, 1973.

[71] H. D. Morrision, B. K. Garside, and J. Reid. Dynamics of the optically pumped midinfrared NH_3 laser at high pump power. *IEEE J. Quant. Electron.*, 9:1051, 1984.

[72] H. C. Miller, G. Hager, P. G. Crowell, and A. I. Lampson. Overview of gas phase optically pumped infred laser: A comparison between theory and experiment. *Proceedings of the international conference on laser'93*, page 576, 1994.

[73] R. A. Serway and R. J. Beichner. *Physics for scientists and engineers.* Sauders cillege publishing, 2000.

[74] UKIRT. Irtrans4. http://www.jach.hawaii.edu/UKIRT/.

[75] S. G. Johnson, M. Ibanescu, M. Skorobogatiy, O. Weisberg, T. D. Engeness, M. Soljacic, S. A. Jacobs, J.D. Joannopoulos, and Y. Fink. Low loss asymptotically single mode propagation in large core OmniGuide fibers. *Optics Express*, 9:748, 2001.

[76] N. Skribanowitz, I. P. Herman, and M. S. Field. Laser oscillation and anisotropic gain in the 1 → 0 vibrational band of optically pumped HF gas. *Appl. Phys. Lett.*, 21:466, 1972.

[77] J. D. White, A. Chakrabarti, and J. Reid. Optically pumped atmospheric-pressure CO_2 laser. *Appl. Phys.*, B51:371, 1990.

[78] R. Thapa, K. Knabe, M. Faheem, A. Naweed, O. L. Weaver, and K. L. Corwin. Saturated absorption spectroscopy of acetylene gas inside large-core photonic bandgap fiber. *Opt. Lett.*, 31:2489, 2006.

[79] F. Benabid, J. C. Knight, G. Antonopoulos, and P. St. J. Russell. Stimulated Raman scattering in hydrogen-filled hollow-core photonic crystal fiber. *Science.*, 298:399, 2002.

[80] F. Couny, F. Benabid, and P. S. Light. Large-pitch kagome-structured hollow-core photonic crystal fiber. *Opt. lett.*, 31:3574, 2006.

[81] J. T. Verdeyen. *Laser electronics.* Prentice Hall, Inc., 1995.

[82] A. Ratanavis, N. Campbell, A. V. V. Nampoothiri, and W. Rudolph. Performance and spectral tuning of optically overtone pumped molecular lasers. *IEEE J. Quant. Electron.*, 45:488, 2009.

[83] A. Ratanavis, N. Campbell, and W. Rudolph. Feasibility study of optically pumped molecular lasers with small quantum defect. *J. Opt. Commun*, In press, 2009.

[84] V. Nampoothiri, A. M. Jones, A. Ratanavis, R. Kadel, N. Wheeler, F. Couny, F. Benabid, B. R. Washburn, K. L. Corwin, and W. Rudolph. Mid-ir laser emission from a C_2H_2 gas filled hollow core photonic crystal fiber. *Photonics West*, Submitted, 2010.